Probing the Crystallization Process and Morphology of Thin Films of Yttrium Iron Garnet on Non-Garnet Substrates with *in situ* TEM Methods

A Dissertation
SUBMITTED TO THE FACULTY OF
UNIVERSITY OF MINNESOTA
BY

Thomas E. Gage

IN PARTIAL FULFILLMENT OF THE REQUIREMENTS
FOR THE DEGREE OF
DOCTOR OF PHILOSOPHY

Prof. David J. Flannigan, Advisor
Prof. Bethanie J.H. Stadler, Advisor

October 2018

Acknowledgments

I would like to first thank my advisors, Professor David Flannigan and Professor Bethanie Stadler, for guiding me in my research and teaching me how to be a scientist. I was able to learn about a number of interesting topics arising out of the co-advised assignment. I would also like to thank all of my group members in both the Stadler and Flannigan group. Karthik and Prabesh especially helped with growth of the garnet films and care of our sputtering system. This work would not have been possible without the extra ordinary efforts of Dan, Dayne, Boo and Alyssa turning an empty room into a fully operational UEM lab. Finally, I would like to thank my family and friends who helped get me through the PhD process. Without their support all of this would have been impossible.

Abstract

Thin films of yttrium iron garnet (YIG) are of high interest for promising photonics and spintronics applications. Integration challenges with current silicon processing technology have limited device geometries and caused reduced performance largely arising from crystallization issues of as-deposited films. In order to gain understanding of the amorphous to crystalline phase transformation of YIG thin films on non-garnet substrates, plan-view TEM and *in situ* laser annealing TEM methods were utilized. Thin YIG films were sputtered onto SiO_2 TEM window membranes. These films were initially annealed *ex situ* using standard RTA annealing methods. A nanocrystalline matrix phase between YIG crystallites was discovered where previous studies had reported uncrystallized material. Preliminary *in situ* laser annealing led to the serendipitous discovery of a 2-step rapid thermal anneal which improved garnet phase formation in the films. To investigate YIG crystallization kinetics on SiO_2, temperature dependent *in situ* laser annealing TEM diffraction experiments were conducted. Avrami constants and apparent activation energy for the nanocrystalline phase formation is reported. *In situ* bright-field TEM was also used to investigate the growth of the YIG crystallites and indicated they enter a stress limited growth phase after reaching a critical dimension. Additionally, considerable effort was put into instrument development for *in situ* TEM methods, including optimization of single-shot pump probe capability. A range for optimized cathode to Wehnelt aperture distance

and photoelectron inducing laser fluence are reported. Demonstrations of single-shot capabilities in both diffraction and imaging modes with current equipment are shown.

Table of Contents

List of Tables

List of Figures

1. Chapter 1 – Introduction

"There's plenty of room at the bottom." This phrase coined by Richard Feynman has been used in the context of progressing all of nanotechnology since he first used it in 1959.[1] At its conception, Feynman was considering the idea of being able to directly manipulate individual atoms in order to create nanostructures of his choosing. While we do not yet have control over atoms in the ways Feynman was fantasizing about, nanotechnology has progressed an astonishing degree since this time.

This idea of smaller devices and nanotechnology in general has largely sparked the field of material science into a new direction in the 21st century away from classic bulk measurements and towards the nanoscale. At shorter length scales, the properties of materials begin to change in some unexpected ways. Device sizes in many different fields are moving to nanometers and beginning to approach single unit-cell dimensions.[2-4] Being able to create and tailor material properties on the nanoscale is crucial for any emerging nanotechnology. In order to have this level of control at short length scales, however, understanding how materials form and change when constructing devices with nanometer length scales is paramount. Control over these processes is getting towards Feynman's dream.

In this thesis, the theme of increased understanding of nanoscale processes provides the motivation for experimental and instrumentation studies. The following work will focus on a specific example of nanoscale control and understanding of the crystallization

process in thin films of yttrium iron garnet as well as the advancement of using *in situ* TEM studies to better understand non-reversible nanoscale processes. After relevant theory, backgrounds, and methods are discussed, the following chapters include three of the studies I completed during my PhD work which helped to give valuable insight into the overarching thesis theme.

1.1 Yttrium Iron Garnet

Yttrium iron garnet (YIG), $Y_3Fe_5O_{12}$, is a synthetic oxide that is a promising material for a host of technologies. YIG was first developed by Bertaut and Forrat[5] in 1956, and it has received constant research attention since then because it possesses a number of interesting properties, such as negligible optical absorption at infrared wavelengths[6], low spin-wave dampening[7], microwave filtering capability [8] and promising magneto-optical properties[9]. Each of these properties are critical for emerging technologies in both integrated photonics and spintronics. In the following sections, I will outline the above mentioned material properties of YIG and discuss why high quality crystalline thin films are important to potential devices.

1.1.1 Physical Properties

Yttrium iron garnet has a large unit cell with 160 total ions and a lattice parameter of 12.376 Å.[10] It is of the I_{a3d} space group and has a basis of five iron ions, three yttrium ions, and 12 oxygen ions. As can be seen in Figure 1.1, all yttrium ions are coordinated by eight oxygen ions, while the iron ions sit in two different coordination sites. Two Fe^{3+} ions

are octahedrally coordinated while three Fe^{3+} ions are tetragonally coordinated.[10] The two different iron ions are coupled antiferromagnetically, but due to unequal magnetic spin, YIG is ferrimagnetic. The unpaired spins in YIG results in Zeeman splitting of optical absorption peaks with applied magnetic fields, and this in turn leads to unequal velocities for right- and left-circular polarized light. When linearly polarized light propagates through magnetized YIG, it is therefore rotated nonreciprocally, an effect known as Faraday rotation. YIG is an insulating oxide with a band gap near 2.85 eV[11] and is highly transparent at optical communication wavelengths.[12] In amorphous YIG, the lack of ordering causes the iron ions to be both in the 2^+ and 3^+ state with a distribution of oxygen coordination and no magnetic structure, eliminating most of the interesting material properties.

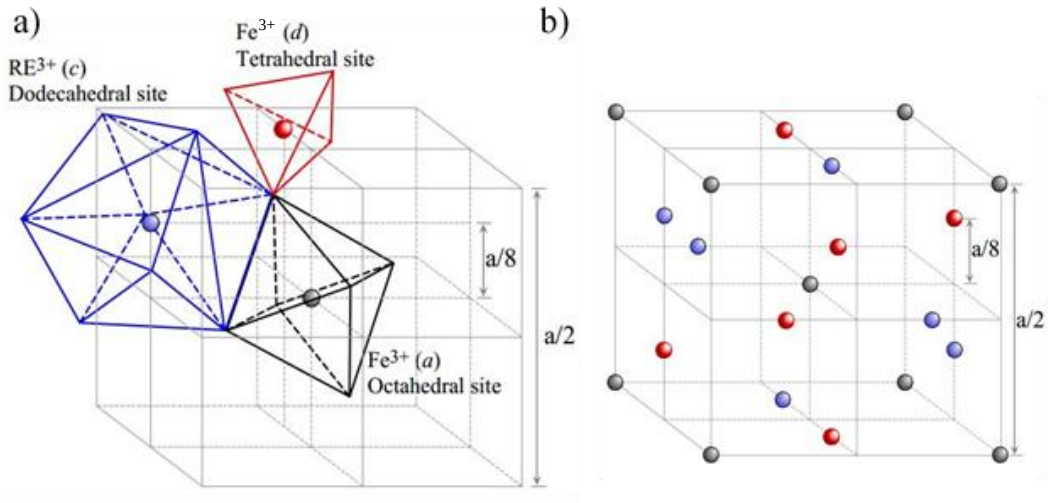

Figure 1.1. Partial unit cell for the YIG crystal structure. (a) Shows the oxygen coordination for the different ions. (b) Ion positions in the lattice. Adapted from Ozgur et al.[13]

It is the low absorption and the magneto-optical properties that make it a leading candidate for integrated photonic circuitry devices. Yttrium iron garnet displays a strong Faraday Effect in the visible and infrared spectrum.[6] The Faraday Effect combined with YIG's low absorption at these wavelengths means that it is possible to construct photonics devices which can be both highly efficient and have short length scales, characteristics necessary for integrated photonic circuits (PIC). By substituting yttrium ions with larger rare earth ions, typically Bi or Ce, it is possible to change the compensation temperature and increase the Faraday rotation for the material at room temperature.[14-15] Typical photonic device structures contain light propagation to a silicon, silicon nitride, or silicon oxide waveguide, where the functional material is a cladding on part of the waveguide, interacting with the evanescent tail of the light in the guide.[16-19] This structure, shown in Figure 1.2, allows for fewer material interfaces as the light propagations through the circuit. However, it is difficult to grow substituted YIG directly on non-garnet materials, so a thin film of undoped YIG can be used as a seed-layer. The seed-layer is typically between the waveguide and the garnet cladding, so it must be thin to maximizethe evanescent tail inside the substituted garnet.[17] This is one motivation for understanding and improving the crystallization behavior of thin films of YIG on non-garnet materials.

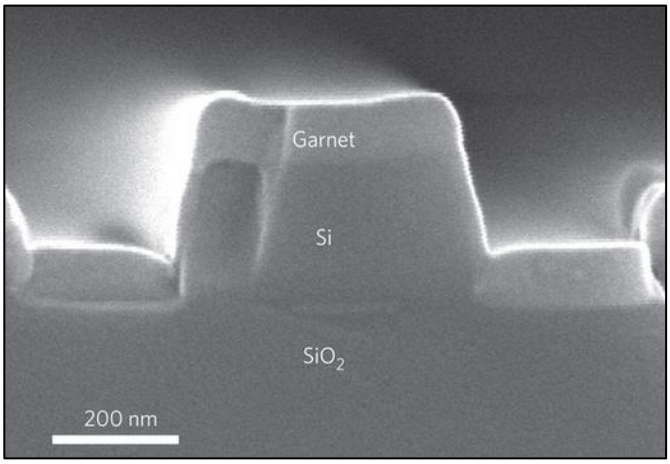

Figure 1.2. Cross-section of a silicon waveguide on SiO_2 with a garnet cladding. Adapted from Bi et al.[20]

More recently, YIG has been one of the most important materials for emerging spintronics research, due largely to its low Gilbert damping which enables efficient excitement of magnetization dynamics.[21-23] YIG can be pumped with high frequency microwaves at frequencies that match the material's intrinsic magnetic moment precession. This causes all of the moments to precess in unison creating a coherent spin wave in the material. The coherent spin moment oscillation is the basis for important physical phenomena such as the Spin Hall and Inverse Spin Hall Effects where the coherent spin wave can interact with electrical currents at the interface of adjacent metallic films.[24] For thinner films of YIG in contact with a metallic material, the damping coefficient increases, meaning there is increased interaction and improvement of the Spin Hall and Inverse Spin Hall Effects, improving potential device performance shown in Figure 1.3.[25]

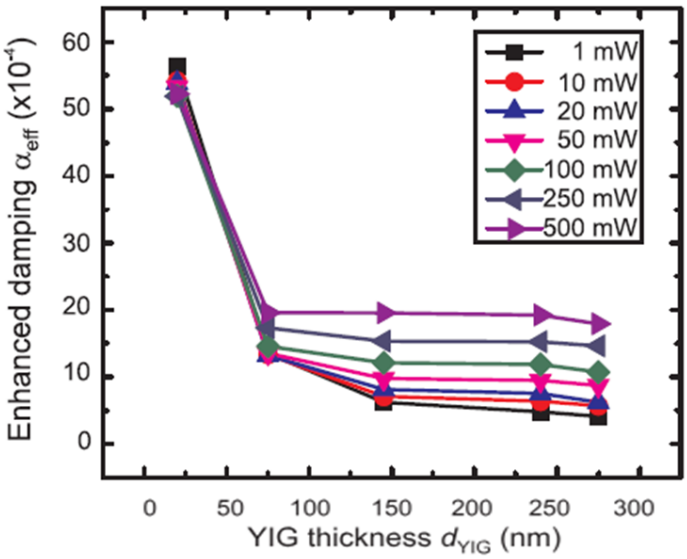

Figure 1.3. A plot showing the trend between YIG film thickness and enhancement of the damping coefficient for spin pumping a Pt film. Adapted from Jungfleisch et al.[25]

The Spin Seebeck Effect refers to the generation of a spin voltage caused by a temperature gradient in a ferromagnetic material. This spin voltage can cause thermal injection of spin currents into attached nonmagnetic metals. By the Inverse Spin Hall Effect, this spin current can be converted to a useful charge voltage.[26] YIG has been demonstrated to be one of the most promising materials for using the Spin Seebeck Effect to harvest waste heat and convert it to usable energy.[27] Again, thin films of high quality YIG are needed to most effectively harvest heat while limiting the insulating effect of added material to a system. Here, polycrystalline films have been demonstrated to perform comparably to single-crystal systems.[28]

This is not a comprehensive list of the possible applications of thin films of YIG, however, it does give a flavor of the importance that they can play in emerging technologies. So long as photonics and spintronics show promise as revolutionary technologies in communication and computing, YIG will continue to play a critical role and receive high interest as a material.

1.1.2 Crystallization Challenges

In all of the above cases, thin films of YIG are needed in materials systems where they cannot be grown epitaxially for wide spread device adoption. In most studies concerning the performance of YIG and the underlying physical properties associated with thin films of the material, YIG is grown on gadolinium gallium garnet (GGG). This allows for epitaxial growth of the YIG crystal structure ensuring a high quality single-crystal film. By definition epitaxy requires a garnet substrate, limiting potential device geometries. GGG, however, is expensive, non-abundant, and incompatible with silicon wafer processing. Some researchers have attempted wafer bonding as a means to get around this problem, building a device and fusing the YIG film to the top.[29-30] Again, geometry issues arise because of the thick GGG substrate atop the device structure in this case.

Efforts by the optics community to develop high quality YIG films grown directly on silicon based devices have had mixed results. It has been demonstrated that phase pure YIG thin films can be attained by pulsed laser deposition (PLD) or sputter deposition with subsequent annealing to crystallize.[31-33] Thicker films of YIG (>45nm) have been shown

to crystallize with high phase purity given the right annealing conditions on non-garnet substrates. Below 45nm, thin films of YIG do not fully crystallize into garnet.[34] This effect is shown in Figure 1.4(a). A number of publications have investigated the optimization of the YIG crystallinity in thin YIG films, though no previous publications had investigated the fundamental crystallization kinetics of the amorphous to crystalline phase transformation in thin YIG films on non-garnet substrates.

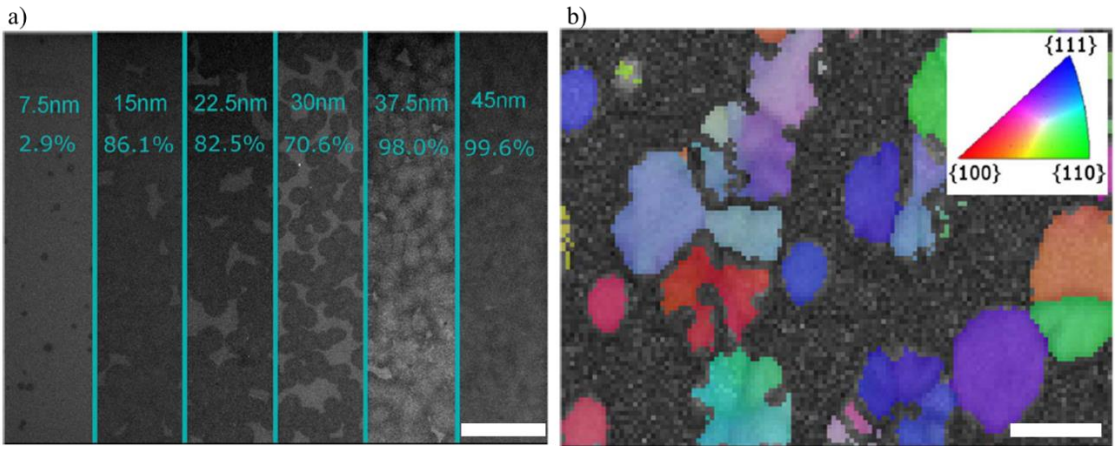

Figure 1.4. (a) SEM micrographs showing increased YIG phase formation with increasing thickness. Darker film regions are garnet. Scale bar 10 µm (b) EBSD image where YIG crystallites' crystallographic orientation have been mapped. The gray region is reported to be amorphous. Scale bar 2 µm. Adapted from Block et al.[34]

1.2 Solid State Crystallization Kinetics

An amorphous material is defined as having no long range atomic order. There can still exist short range order in glasses corresponding to the atomic arrangement and spacing of nearest neighbor ions. Where short range order can become long enough to be considered a crystal is a question which has vexed materials scientists and will not be answered in this thesis.

Glasses are traditionally formed by rapidly cooling a material from a liquid state with no change in specific volume. In this way, glasses can be thought of as super-cooled liquids with atoms not having enough energy to move around with respect to each other, creating a solid material. Most materials, with the exception of pure metals, can be prepared by rapid quenching in order to form the amorphous state. Creating a glass without a network former elementis possible but requires more specialized preparation, such as sputtering, as described here, to create a glassy film from a gas.[35]

Controlling the crystallization process of the glass can allow for the tailoring of its properties. The investigation of crystallization in terms of kinetics is important for scientists and engineers to properly understand this phenomenon. The role of temperature and temperature change rates can have a profound impact on the nucleation, growth, and phase behavior of a glass.

Crystallization of an amorphous solid is a two part process involving nucleation and growth of crystallites. Nucleation can be either homogeneous or heterogeneous. Homogeneous nucleation refers to the case where nucleation occurs in the volume of the amorphous material with no influence of additives. Heterogeneous nucleation refers to the

case where nucleation occurs at sites where the amorphous material is in contact with a foreign particle or surface. After nucleation, growth occurs by mechanisms that also have different types of observable behavior.

Nucleation is driven by the difference in free energy between the amorphous state and the crystalline state. Due to a competition between surface energy ($\alpha\ r^2$) tending to minimize the surface area of a crystallite and volumetric Gibb's free energy ($\alpha\ r^3$) tending to maximize the volume, there is a critical nuclei size which must be overcome to form a stable nuclei. This is depicted in Figure 1.5. The radius corresponding to r_c is the point at which nuclei smaller than it will be driven to shrink while those larger will enter into the growth phase.

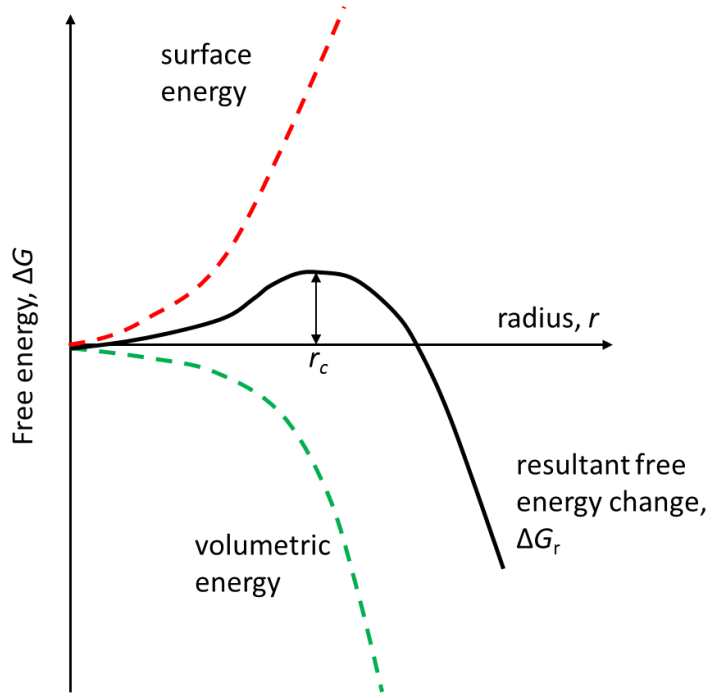

Figure 1.5. Plot of Gibb's free energy versus the radius of a nucleation site. The critical radius for stable nucleation is noted as r_c.

Crystal growth is the increase in size of the crystallite as the surrounding amorphous material is converted to the crystalline phase. The growth rate is controlled by thermodynamic forces and the rate at which atoms successfully join the crystalline phase from the amorphous phase. At higher temperatures, ions in the amorphous phase will have more energy to move into an energetically favorable position in the crystal, however, the thermodynamic driving force decreases linearly with temperature above the crystallization temperature. This results in a maximum crystal growth rate a specific temperature for a given system.

By studying the fraction crystallized in a system as a function of time and temperature, a number of assumptions about the crystallization kinetics can be inferred using the Johnson–Mehl–Avrami–Kolmogorov (JMAK) model.[36-37] These include the dimensionality and controlling mechanism of crystal growth, the geometry and kinetics of nucleation sites, and the activation energies for transformation. Common techniques for determining the fraction of a material crystallized include differential scanning calorimetry, X-ray diffraction, magnetometry, resistivity measurements, and optical measurements. Any signal which can linearly relate the fraction crystallized to the measurement signal can be conveniently used with the JMAK formalism.

The JMAK model of crystallization requires an isothermal state. For any system in which one phase, α, is transforming into another phase, β, such as shown in Figure 1.6 and meets the constant temperature criterion, the following analysis can be applied.

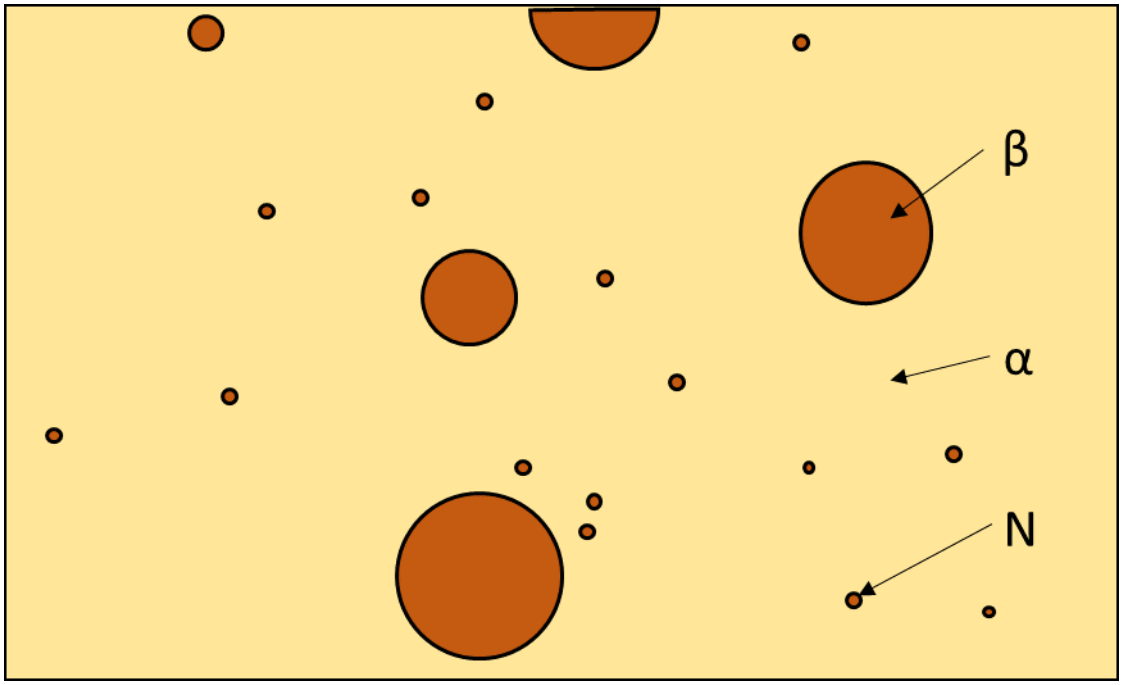

Figure 1.6. A representation of the nuclei and beta phase forming in an alpha phase. The beta phase shows radial growth behavior here.

The total volume of the system is taken to be the sum of the volumes of α and β.

$$V = V_\alpha + V_\beta$$

The fraction of the volume transformed is represented as X. $\dot{N}$ is taken as the nucleation rate per unit volume and G represents the linear growth rate. The number of nuclei formed in a timeline τ is proportional to the volume.

$$N = V\dot{N}d\tau$$

On a different timeline, t, starting when the isothermal temperature is achieved, the radius to which the nuclei has grown can be considered

$$r = G(t - \tau)$$

Now the volume of the particles nucleated during dτ at time *t* is

$$dV_\beta = \frac{4\pi}{3}\dot{G}^3(t-\tau)^3 V\dot{N}d\tau$$

assuming spherical growth of the crystallites. If we assume to have limited effect on the volume change from the nuclei, this equation can be integrated over dτ yielding

$$V_{ex} = \frac{\pi}{3}\dot{G}^3 t^4 V\dot{N}$$

So far, this analysis has not taken into account that portions of the volume have already been transformed and some of the transformed volume may be outside of the original volume. Now the idea of extended volume will be applied to account for this. Here the argument is made that amount of phase dV_β formed is proportional to the amount of phase formed in the extended volume $dV_{\beta e}$ with a factor of the amount of the α phase formed.

$$dV_\beta = dV_{e\beta}(1 - \frac{V_\beta}{V})$$

Integrating both sides of this expression yields

$$ln(1 - X) = -V_{e\beta}/V$$

Now we can substitute in the equation we previously found representing the extended volume of the β phase and solve for *X* resulting in the JMAK equation.

$$X = 1 - exp(-Kt^4) \qquad K = \frac{\pi}{3}\dot{G}^3\dot{N}$$

The JMAK equation can be linearized in the following way to find values for *ln(K)* and the Avrami coefficient, *n*, which are important in determining crystallization behavior.

$$ln\big(-ln\big(1-X(t)\big)\big) = ln(K) + n\,ln(t)$$

In this study, time-resolved transmission electron microscopy is used to study crystallization kinetics in thin films. While other techniques have been applied to the time-resolved crystallization study of thin films, there is inherently a difficulty in time-resolved studies in thin films due to the small volume of the film and resulting limited signal.[38] Transmission electron microscopy is unique in its ability to use both real space imaging as well as diffraction for correlated studies in a system. Also, the high brightness and strong interaction of the electron beam with the specimen are able to produce a high signal, ideal of time-resolved crystallization studies of thin films.

When lower signal techniques are used to determine fraction crystallized, signal acquisition times must be made longer, thus limiting the temporal resolution of any such study. Because TEM has such strong signal as described above, in most cases, the temporal resolution of TEM *in situ* experimental are limited to the resolution of the camera used. Pump-probe techniques combined with TEM described in the following section can be used to overcome this temporal limitation.

1.3 Ultrafast Electron Microscopy

Traditional time-resolved electron microscopy experiments are limited in temporal resolution by the camera read out times. While TEM camera technology has seen vast

improvements over the decades, now pushing into the sub millisecond temporal resolution regime,[38-40] it still is not able to be used for the study of dynamic processes for many natural processes of interest. There is a method for improving the temporal resolution beyond that of the camera known as a pump-probe technique. Using pump-probe techniques in conjunction with TEM is known as ultrafast electron microscopy.

There are two types of ultrafast electron microscopy, stroboscopic and single-shot, depicted in Figure 1.7.[41] The stroboscopic technique builds up a signal by repeatedly striking the specimen with a pump laser pulse and a subsequent probe electron packet with a defined delay time, allowing time for the system to relax before the next pump pulse. Once enough signal has been acquired, the delay time is changed, thus creating a dataset able to demonstrate dynamics. The temporal resolution is only limited by the duration of the electron packet which can be sub-picosecond.[42] The downside of this technique is the necessity for reversible processes. The system must be able to reproduce the same dynamics with every pump pulse and relax to the same state each time. While there are many natural phenomenon which do meet this condition, there are a number which do not, leading to the second type of UEM technique, single-shot.

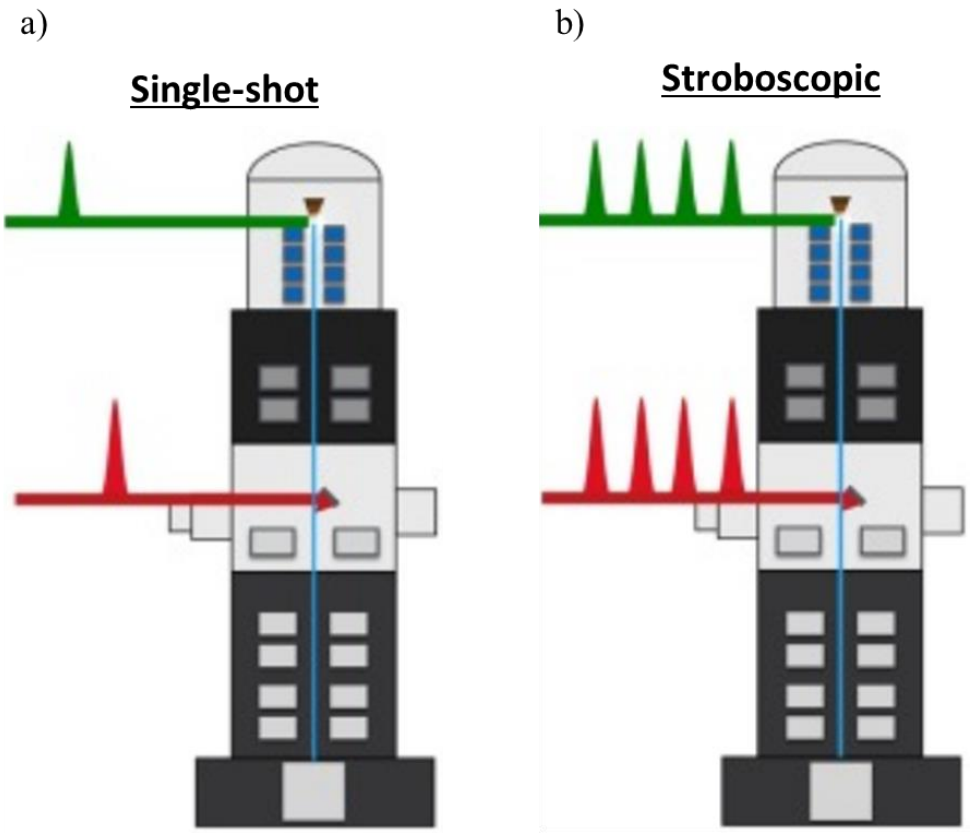

Figure 1.7. A representation of a pump-probe setup in a TEM. Here laser pulses enter the gun region and specimen region of the TEM. (a) Only one pump and probe pulse are used in single-shot mode. (b) A pulse train is used in stroboscopic mode to build up a signal from a highly reversible process. Adapted from Arbouet et al.[43]

In the single-shot setup, the entire signal must be formed from a single electron probe packet. While it is still possible to use the pump-probe technique to achieve high temporal resolution, the columbic repulsion of the electrons within a probe electron packet causes the packet to spread out, limiting the temporal resolution of this technique. This leads to an inherent tradeoff between signal and temporal resolution in single-shot UEM.[44] The advantage here, however, is being able to probe a process which is irreversible.

At the University of Minnesota, we have constructed a lab designed to perform both stroboscopic and single-shot UEM experiments. The equipment and operation of this lab are described in Chapter 2. This thesis includes instrumentation experiments on the single-shot UEM setup. While the original intent was to be able to probe crystallization dynamics with this technique, current hardware limitations made this task unachievable. Instead, Chapter 6 describes the optimization of our single-shot setup and suggestions for future improvements.

2. Chapter 2 – Equipment and Methods

In this chapter, I detail the experimental techniques used in the following chapters. I will briefly describe the theory of the technique and the practical setup I used in this thesis.

2.1 Sputtering

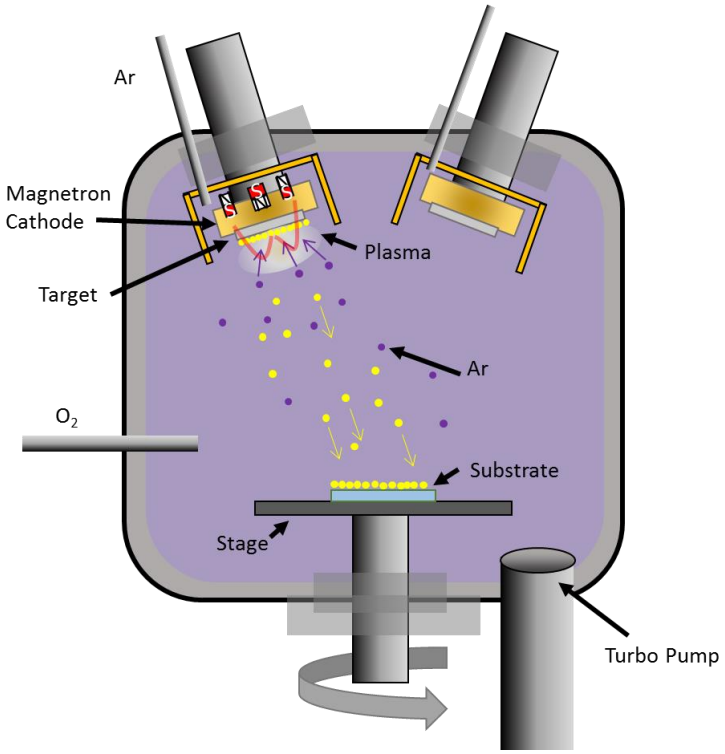

Figure 2.1. A typical top down sputtering chamber representation. The magnetic field from the magnetron holds electrons near the target. Target atoms are ejected by a high energy Ar plasma and deposit on the substrate.

Sputtering is a physical vapor deposition method commonly used for thin film growth. It has ranges in application from semiconductor device fabrication to hard-disc drive media film deposition. Sputtering is a highly repeatable deposition method that can also provide high quality films growth from a range of materials.[45] Figure 2.1 shows the working principle of the sputtering chamber used for the film growth used in this work. This setup is similar in all sputtering systems, though variations in geometry are common. The system used here is known as a sputter-down configuration. A sputtering target is held

at a negative bias and attracts positively charged Ar gas that is introduced to the chamber near the gun region. Upon collision of the Ar with the target, the kinetic energy of the Ar is transferred to the atoms in the target. This causes an ejection of the atoms in the target, some of which end up on the substrate as a thin film. This is a complicated process due nature of the plasma interacting with itself and the potential charging of the target. The complications of this process and some solutions are addressed in the following sections.

2.1.1 Magnetron Sputtering

Magnetron sputtering aids in dealing with a fundamental problem of the sputtering setup, secondary charge. It is possible to build up a positive charge on the surface of the sputtering target which can shield the negative bias created to attract the Ar ions. In order to counteract this phenomenon, a magnetron is placed behind the target, creating a ring of high magnetic flux on the surface of the target. This magnetic field traps secondary electrons created during the sputtering process, greatly increasing the ionization efficiency.[46] This helps with increased deposition rate when compared to non-magnetron sputtering.

2.1.2 RF Sputtering

Direct current (DC) source power for sputter guns is common and useful for metallic targets. Metallic targets are able to conduct charge which can build up on the surface during sputtering. For non-conducting targets, the surface charge will continue to build up and eventually terminate the plasma. A solution to this problem is to use a radio

frequency (RF) power source. The alternating current (AC) of this power source attracts the positively charged Ar ions during the negative half of the cycle and attracts negatively charged electrons during the positive half of the cycle. The electron mobility is much higher than the positive charge, resulting in a time averaged negative charge for the target.[47]

2.1.3 Reactive Sputtering

Oxide films can be deposited in one of two ways. The first method is to sputter an oxide target directly. This process has the benefit of being able to assume that the sputtered target will result in a film with a nearly identical stoichiometry to the target. The drawback of this method is a large reduction in deposition rate due to the strong covalent bonding in an oxide compared with the following method, reactive sputtering.[47] In a reactive sputtering setup, a metallic target is sputtered while a reactive gas is flowed into the chamber. To achieve an oxide film, oxygen is flowed in. Oxygen is then able to react with the particles being sputtered at the substrate to form an oxide thin film.[48]

While reactive sputtering can lead to much higher deposition rates than oxide sputtering, there are a number of challenges that present as well, namely target poisoning. This term refers to oxidizing the surface of the target such that it now behaves as if it were an oxide target. In order to get back to a metallic target, the oxide surface must first be sputtered away. Often it is optimal to operate at an oxygen pressure which is just below the range in which poisoning will start to occur as seen in Figure 2.2. This leads to a high oxygen content in the film as well as high deposition rates.[48]

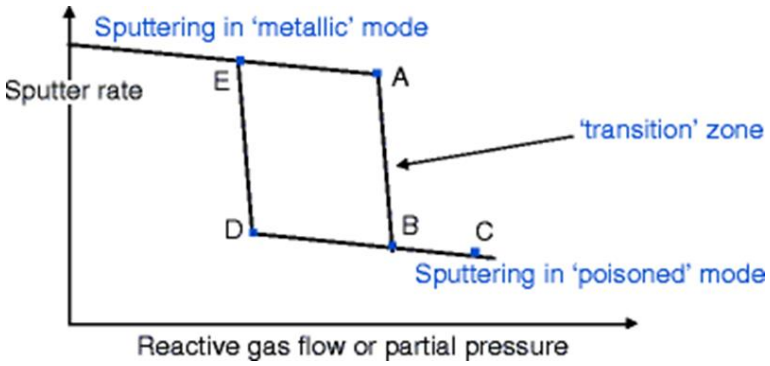

Figure 2.2. Sputtering target poisoning occurs as the reactive gas flow increases and the sputtering rate decreases. Point A is the optimal operating position. Once the target is poisoned (point B) it must be brought back to point E through point D to recover a metallic deposition behavior. Adapted from Lippens et al.[49]

2.1.4 Sputtering Parameters

Alluded to above is the impact that oxygen pressure can have on the sputtering process. It is the interaction of the base vacuum, argon partial pressure and oxygen partial pressure, which can dictate the quality and properties of the resultant film. The purity of the film largely depends on the base vacuum pressure. Typically, turbo pumps are used to bring reduce the pressure in the sputtering the range of 10^{-6} Torr.[47] This provides films of reasonable purity, though some films requiring higher purity use base vacuum pressures closer to 10^{-8} Torr. During deposition, the partial pressure of Ar has an optimal point at which there are enough ions to sputter quickly but a low enough pressure such that collisions and scattering or sputtered atoms in the plasma are low. The nominal partial pressure optimization is highly chamber dependent.[47]

Target thickness is also important for magnetic targets like those used in this work. For thick magnetic targets, the magnetic field from the magnetron is shunted by the magnetic material. This eliminates the effect of the magnetron and can lead to low sputtering rates. For this reason, all magnetic targets used here are less than 1/8th" thick.[47]

2.1.5 Working Setup

The sputtering setup in this work was done in a home-built system. It has 3 AJA magnetron guns, one of which is designed for magnetic materials. All guns are compatible with 2.0" diameter targets. Argon gas lines feed directly into the gun region of the chamber maximizing sputtering rate while minimizing sputtering operating pressure. The stage can be rotated so that films are uniform in thickness and composition. Oxygen is flowed into a ring near the substrate stage. This setup does not have stage heating, though that is a common feature in other sputtering chambers. A high vacuum gauge is used to monitor the working pressure of the chamber.

2.2 Rapid Thermal Annealing

Rapid thermal annealing (RTA) is a common thin film processing route. Typically it is used to induce a phase change, oxidation, dopant activation, or grain growth in thin films.[50-53] The working principal of the rapid thermal anneal is to use high intensity tungsten filament bulbs to quickly heat a substrate wafer while monitoring the temperature of the wafer with a closed feedback loop controlling the bulb intensity. This setup is shown

in Figure 2.3. By adjusting feedback parameters, temperature gradients on the order of 100 °C/sec are achievable with high precision at the holding temperature. This is useful for reporting temperature dependence of isothermal processes.

There are two common ways the temperature of the substrate is monitored during RTA. The first is by using a thermocouple. The thermocouple is comprised of a conductive loop made of two different materials. Due to the thermoelectric effect, a voltage is produced by the thermocouple which is temperature dependent to a high degree of repeatability. There is a ceiling of operation for common thermocouples near 1000 °C and oxidation can lower this threshold further. The thermocouple used in this work is a type K thermocouple which consists of nickel-chromium and nickel-alumel. It is rated for continuous use up to 800 °C.

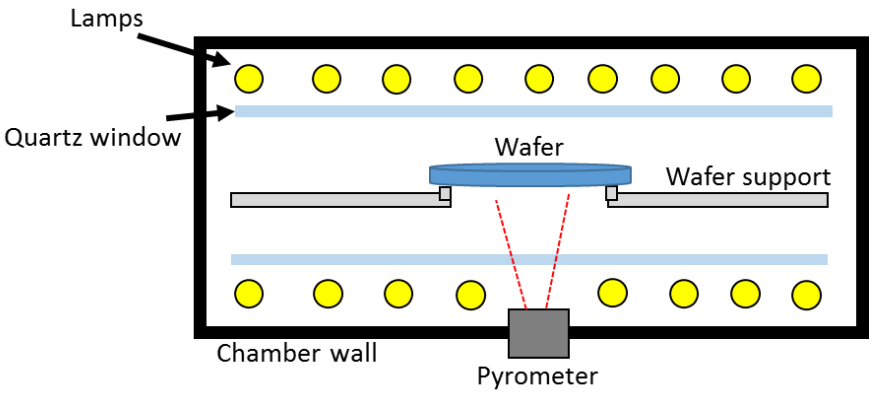

Figure 2.3. A RTA furnace diagram. The tungsten lamps are in rows on the top and bottom of the chamber. The wafer sits on quartz support. The pyrometer views the bottom of the wafer for black body radiation.

The second means by which to monitor temperature during a rapid thermal anneal is by using a pyrometer. A pyrometer works by measuring the black-body radiation from a silicon wafer and comparing the wavelength dependent intensities against calibrated values. This method of measurement achieves greater accuracy at higher temperatures because of the increase in black-body radiation. There is a small camera inside the RTA which can measure the spectrum and instantly report a temperature. There are significant drawbacks to this measurement method such as significant effects of contamination in the RTA and low signal compared to the thermocouple especially at low temperatures.

In this work, all *ex situ* anneals are performed using an MTS Rapid Thermal Processor 600-S which can operate in either temperature measurement mode. The chamber of the RTA consists of a small quartz line chamber and tungsten-halogen lamps. Samples were heated to between 400 and 900 °C and held for 2-3 minutes. Anneals were performed while flowing either 10 SLPM of O_2 or N_2 at 1 atm.

2.3 X-ray Diffraction

X-ray diffraction (XRD) is a powerful materials science tool for probing a material's crystallographic structure. High energy X-rays are coherently scattered from atomic planes in a sample of interest. These X-rays are commonly generated from a Cu or Co source when impacted with high energy electrons. The source atoms are electronically excited and when they relax, they emit characteristic X-rays. The wavelengths of these X-

rays are elementally specific as well as energy specific and can be filtered to allow for a highly coherent beam.[54]

X-rays are wavelike in nature and can constructively interfere. Because crystals are made of repeating unit cells, there will be certain angles at which incident X-rays will constructively interfere after reflection while all other angles will cause destructive interference. This is known as Braggs' Law. It mathematically described as follows,

$$d = \frac{n\lambda}{2\sin\theta}$$

where d is the interplanar spacing in the crystal, n is the order of the reflection, λ is the wavelength of the incident X-ray, and θ is the incident angle relative to the surface. A typical XRD spectrum consists of an incident angle plotted against the intensity of X-rays at the detector. When the Bragg condition is satisfied in the equation above at a given angle there will be a peak in the intensity.[54] This idea will be discussed in the diffraction section of TEM background in further detail.

XRD can be powerful for identifying crystallographic phases in a material system as well as determining the exact lattice constants and an approximation of grain size. XRD needs to be approached slightly differently for single-crystal versus polycrystalline cases. These cases are highly analogous to diffraction in TEM and will be discussed in further detail in that section.

All XRD analysis used in this work was performed at the University of Minnesota Characterization Facility using the Bruker D8 Discover 2D Diffractometer. This equipment uses a Co K_α source which generates electrons that are collimated to a 0.8 mm

beam. The sample is mounted onto a 3-D translation stage which can position the sample in the beam path. Figure 2.4 shows the geometry of the measurement setup. The D8 Discover uses a two dimensional area detector which takes a slice of the Ewald sphere resulting from the diffraction.

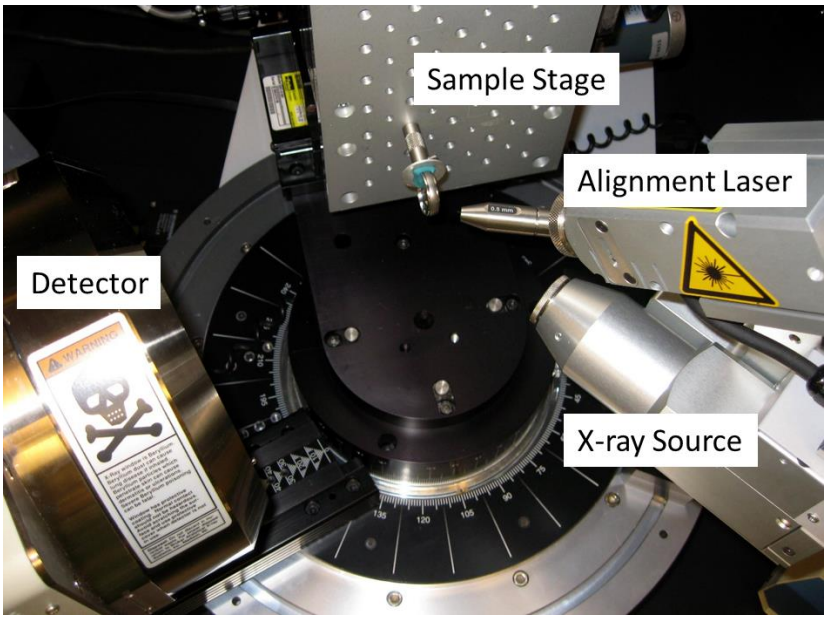

Figure 2.4. The D8 Discover XRD setup used for this thesis. The X-ray source is aligned using a laser spot on the sample stage.

Traditional XRD systems use one dimensional detectors, limiting the amount of signal they gather and the reciprocal space information that can be captured in a single scan. With the two dimensional detector, shorter scan times are possible which can be important for ultra-thin, polycrystalline films such as those in this study. The two dimensional nature of the detector also makes texturing information more readily available.

2.4 Energy Dispersive X-ray Spectroscopy

Energy dispersive x-ray spectroscopy (EDS) uses characteristic x-ray emission to provide information about the elemental composition of a material. By exciting a material with incident electrons, the material will enter into an excited state when core electrons are ejected. When the material relaxes and the core electron vacancies are filled, an X-ray will be emitted. This X-ray will have a specific energy which depends on the element it was emitted from as well as the electronic transition which caused it. With a high enough electron flux, an energy spectrum can be obtained from the characteristic X-ray spectrum which can be related to the elemental composition of the material.[55] In this work, an Oxford Inca X-Act EDS detector at the University of Minnesota Nano Center JSM-6610LC SEM was used to confirm the composition of the films being deposited.

2.5 Atomic Force Microscopy

Atomic force microscopy (AFM) is a technique used to probe small topographical changes on surfaces. This is a surface technique which can have sub nanometer resolution in the vertical direction. AFM operates by moving a sharp tip over a surface and using the back surface of the tip cantilever as a mirror. A laser is incident on this mirror and small deviations in the mirrors angle are magnified. There are numerous modalities and specialization for AFM setups. The two most common operating modes and static force and tapping mode. Tapping mode uses the resonant frequency of the tip to "tap" the surface. This mode is non-destructive but can be less sensitive to fine features and relies

on high tip quality. In this work static force mode is used. In this mode, the tip is dragged along a surface. Because this thesis is concerned with an oxide material, many common issues associated with this mode are not impactful.

In this work a Nanosurf Mobile S AFM was used. The primary function of the AFM was to measure film thickness after deposition. To do this, a line was drawn with a marker on the film before deposition. After deposition, the film was cleaned with acetone and IPA. This resulted in a sharp step-edge where the film deposited on the marker was lifted off. The AFM was able to achieve nanometer resolution which was enough to report the thickness of the films. Surface roughness measurements were also performed using this AFM where grain boundaries and cracks were observed in the films.

2.6 Alternating Gradient Magnetometer

The most common measurement tool for magnetic material is the vibrating sample magnetometer (VSM). A VSM operates on the principle that a magnetic sample vibrating in a magnetic field will produce an electric current which will be a function of the applied magnetic field.[56] This current can be calibrated to a known magnetic moment and the magnetic moment of a sample can be reported. The alternating gradient magnetometer (AGM) works on a similar principle. In this setup, a sample is placed between two alternating magnetic field coils and is attached to a sensitive piezo-electric. As the magnetic field is altered, the force on the magnetic sample also changes, creating a change in voltage in the piezo electric. AGM instruments are more sensitive than typical VSMs but often are more limited in sample size and geometry.[57] In this thesis, AGM

measurements were performed on a MicroMag 2900 AGM from Princeton Measurements at the Institute for Rock Magnetism.

2.7 Transmission Electron Microscopy

In this section, I will give a brief overview of the operational theory of the TEM and describe in more detail some of its operating modes. Time-resolved microscopy and the different instrumentation options will be discussed to help motivate the following chapters where it is used for the majority of the work. The time-resolved TEM laboratory at the University of Minnesota will be described as it relates to this work.

2.7.1 Working Principle

The TEM's core function is to probe the structure of material. To accomplish this function, it uses electrons which have been accelerated to relativistic velocities to interact with a specimen. The electrons are transmitted through a specimen to a camera. These high energy electrons have de Brogli wavelengths on the order of picometers, meaning that the diffraction limit for resolving features will not be the limiting factor for imaging nearly any feature of interest.[58] The high energy electrons can interact with the specimen either coherently or incoherently, or they can pass through the specimen with no interaction. Using all three of these types of electron interactions, many physical properties can be discerned using different TEM techniques.

2.7.2 Components

The basic TEM consists of three functional regions: the gun region where electrons are produced and accelerated, the column where the electrons are directed by magnetic fields and interact with the specimen, and the camera where the electrons are measured. These regions can be seen in Figure 2.5.

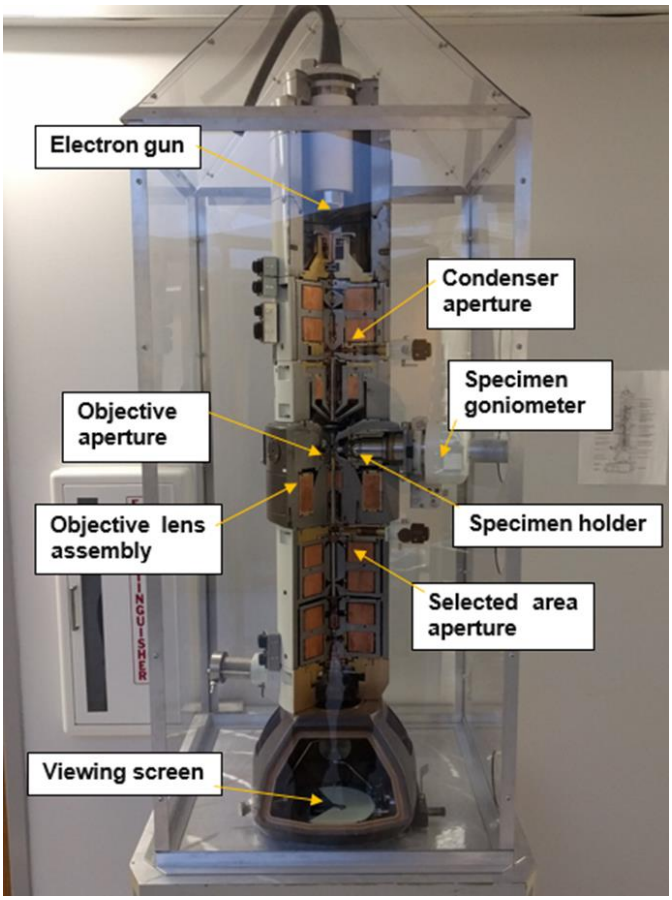

Figure 2.5. Cross-section of a thermionic TEM. Relevant components are labeled.

2.7.2.1 The Gun

There are two families of TEMs which are distinguished by the type of gun cathode they use to produce electrons. One type is field emission guns or FEG TEMs. In this setup,

the cathode is a fine tip of tungsten, and electrons are extracted at room temperature using quantum mechanical tunneling. An electric field is applied and enhanced by the needle like structure of the tip seen in Figure 2.6(b). This tip geometry yields a highly coherent and bright electron beam but is sensitive to any contamination of the tip necessitating ultra-high vacuum. Schottky guns are in the same vein as traditional FEG tips in the sense that they rely on quantum tunneling for electron production as well. Schottky guns use a combination of heating and material selection to lower the work function and make the tunneling process easier.[58]

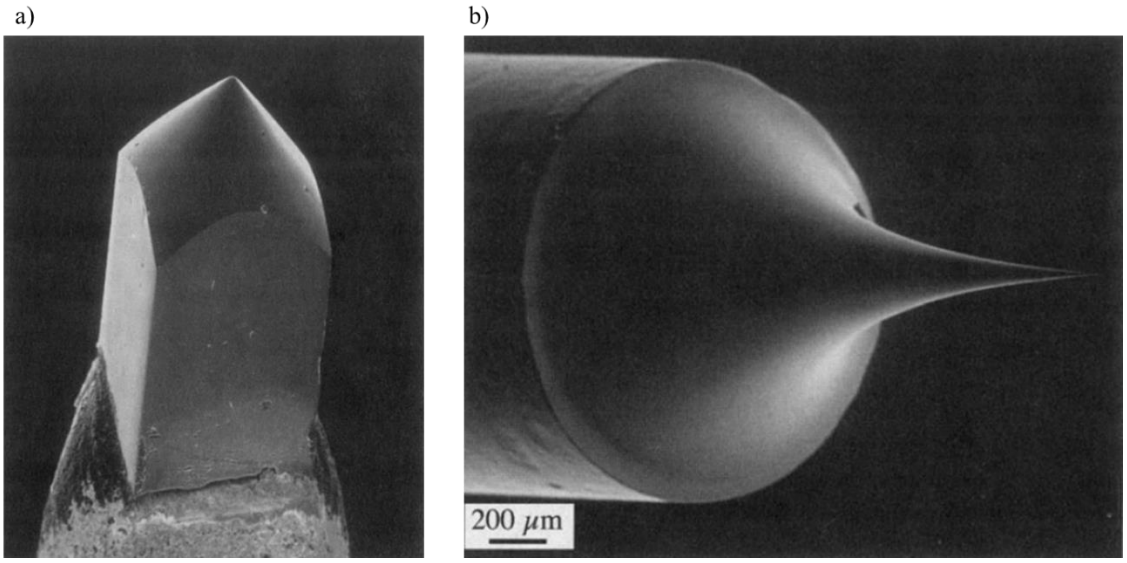

Figure 2.6. Electron cathode tip examples (a) thermionic LaB6 tip (b) needle-like tungsten field emission tip. Adapted from Williams et al.[58]

Thermionic emission guns are the second class of TEM cathodes and rely solely on heating the tip in order to "boil" off electrons. Typically made from either tungsten or

LaB_6, thermionic tips are not as finely tipped as the FEG guns due to their need for higher mechanical stability. This leads to a reduction in coherence. One reason these types of guns are commonly used is that they do not have the same ultrahigh vacuum requirements as FEG sources. An example of a thermionic gun tip can be seen in Figure 2.6(a).[58]

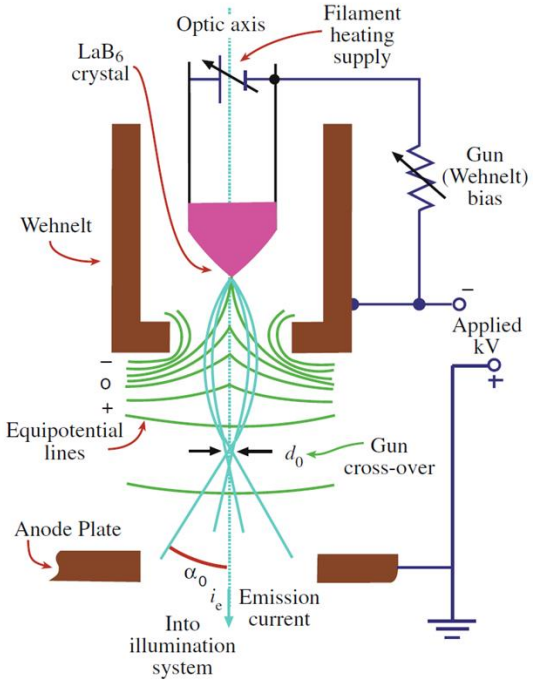

Figure 2.7. Diagram of a thermionic gun region. The heated tip is connected to a self-biasing Wehnelt cap creating a virtual source at cross-over. The anode plate accelerates electrons to relativistic velocities. Adapted from Williams et al.[58]

In thermionic guns microscopes, there is a Wehnelt housing as seen in Figure 2.7. The Wehnelt housing acts to focus the extracted electrons into a point creating a virtual cathode source. The size of the crossover created by the Wehnelt will dictate the brightness and coherency of the electron beam. Also, as shown in Figure 2.7, the Wehnelt is self-

biasing in some gun assemblies. This will prove to be important to note when operating in some experimental modes.[58]

The anode plate is also part of the gun assemble and is used in both FEG and TEG systems to accelerate the electrons to relativistic speeds. Typical voltages for TEM operation are between 60 kV and 300 kV, though some MeV systems exist.[59] The accelerated electrons then enter the column.

2.7.2.2 The Column

It is in the column where the electrons are manipulated and focused by magnetic lenses, allowing for access to different operating modes and changes to magnification. It is also the region of the instrument where the spatial resolution is limited by intrinsic geometry issues related to lensed systems. These spherical aberrations are corrected in some microscopes by using higher order lens systems. The corrections are needed to achieve the highest spatial resolution possible, however, angstrom resolution can readily be achieved without the corrective lenses.[58]

2.7.2.3 The Camera

The electrons need to be detected after interacting with the specimen. In order to form images from the beam, an electron camera is needed. The technology for detection has improved drastically since the beginning of TEM and is still changing today.[58] There are three currently commonly used camera types: CCD (charge coupled device), CMOS (complementary metal-oxide semiconductor), and direct electron. CCD cameras are still the most commonly used. They are relatively cheap and have good performance for

traditional TEM needs. CCD cameras operate by scintillating the incident electrons and capturing the resultant photons on a pixel. These pixel then generate a signal which is read out as part of large ensemble of pixels to form an image. CMOS cameras operate on a similar principle, differing only in how the photon excited charge is read from the chip. CMOS cameras directly convert each pixel's charge value to a digital signal while CCD cameras transport the charge across the chip. Direct electron cameras by contrast do not use any scintillation during the electron detection. These cameras are relatively new and more expensive than the other two types. They do, however, operate with better signal to noise at low electron counts, making them ideal for low dosage experiments.[60] Direct electron detectors also suffer from low dynamic range compared to the other types of cameras limiting their usefulness for diffraction work.

2.7.3 TEM Operating Modalities

The TEM has a number of modes in which it can be operated. I will cover a few here which are relevant to the following studies. First, basic optics need to be described to demonstrate the working principles. Figure 2.8 shows a simplified ray optics diagram. The incident electrons which are coherently scattered by the specimen can be modeled as such when passing through a lens. At the back focal plane, electrons which were parallel to each other when exiting the specimen converge to points. At the image plane, an image of the specimen is formed at a magnification which depends on the focal length of the lens. Though the TEM system is comprised of many lenses, the back focal plane and image plane still exist for the effective lens strength of the TEM lens ensemble.

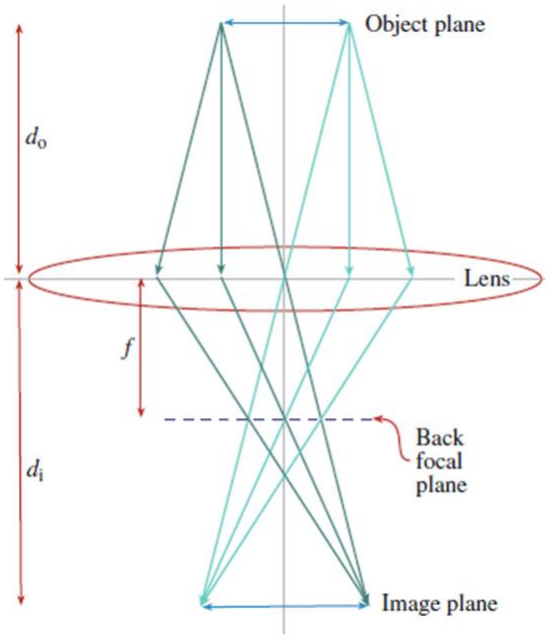

Figure 2.8. Electrons are scattered at the object plane by the specimen. After passing through the objective lens assembly parallel electrons converge at the back focal plane. Spatially coherent electrons at the object plane are used to reform an image of the object. Adapted from Williams et al.[58]

2.7.3.1 Diffraction

The TEM can be used to determine the crystalline structure of a specimen using diffraction techniques to form patterns from coherently scattered electrons. In crystalline structures, ordered crystalline planes scatter electrons at regular spatial intervals, similar to what was described in XRD. Due to Bragg's Law, we observe constructive and destructive interference depending on both the wavelength of the incident electrons and the interplanar spacing. Constructively interfering electrons are only allowed at specific angles for different crystalline structures. This leads to electrons exiting the specimen at different

locations but all having the same allowed angles of trajectory with respect to the crystal lattice they scattered from. As shown above, electrons with the same trajectory when exiting the specimen will converge at the back focal plane. We can view this plane by manipulating the lenses in the TEM resulting in a diffraction pattern.

If the electrons incident on the sample are all parallel to each other, that is known as a parallel beam condition. The resulting coherently diffracted beams will only have one allowed angle with respect to the incident beam from each crystalline domain. Diffraction patterns for a single-crystal will appear as spots with angles and spacing depending on the crystalline lattice. This is a result of the geometry of the Ewald sphere, a three dimensional structure in reciprocal space where the radius of the sphere is the inverse of the electron wavelength. The crystalline lattice is represented in reciprocal space by the reciprocal lattice, with only allowed reflections for the space group being represented. In TEM, the reciprocal lattice sites are relrods elongated normal to the plane of the specimen due to the thinness of the TEM specimen. This elongation allows for the Bragg condition to be met even with some deviation from the exact angular conditions. The Ewald sphere and reciprocal lattice geometry is shown in Figure 2.9.[58] This figure is not to scale for TEM and is more representative of an XRD geometry. An example of a single-crystal diffraction pattern is shown in Figure 2.10(a).

In the case of a polycrystalline specimen, instead of having discrete reciprocal lattice locations, reciprocal spherical shells are used because of the rotational symmetry of the allowed reflections. In this case, the diffraction pattern will appear as circles, with radii

still at only allowed spacing, but all allowed reflections will be seen without having to tilt the specimen to a specific zone axis. An example of a polycrystalline diffraction pattern is shown in Figure 2.10(b).

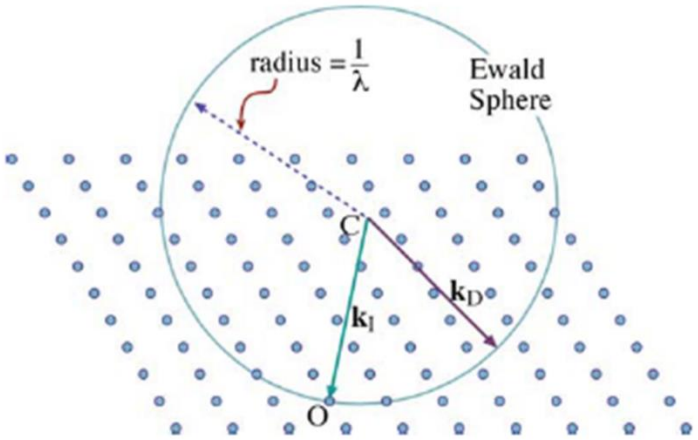

Figure 2.9. Ewald sphere interacting with the reciprocal lattice. The radius of the Ewald sphere in electron diffraction is much larger than represented here due to the short wavelength of the electrons. Adapted from Williams et al.[58]

For an amorphous specimen, no long range order is present. There can still be short range ordering due to average bond lengths of neighboring atoms. In an amorphous material the spacing between neighboring atoms can be defined by a probability function. This results in a radial distribution function (RDF) appearing in diffraction space where the different real-space interatomic spacings are represented in reciprocal space as diffuse rings with increased intensity at favorable atomic spacing radii. An example of an amorphous specimen parallel beam electron diffraction (PBED) pattern is shown in Figure 2.10(a).

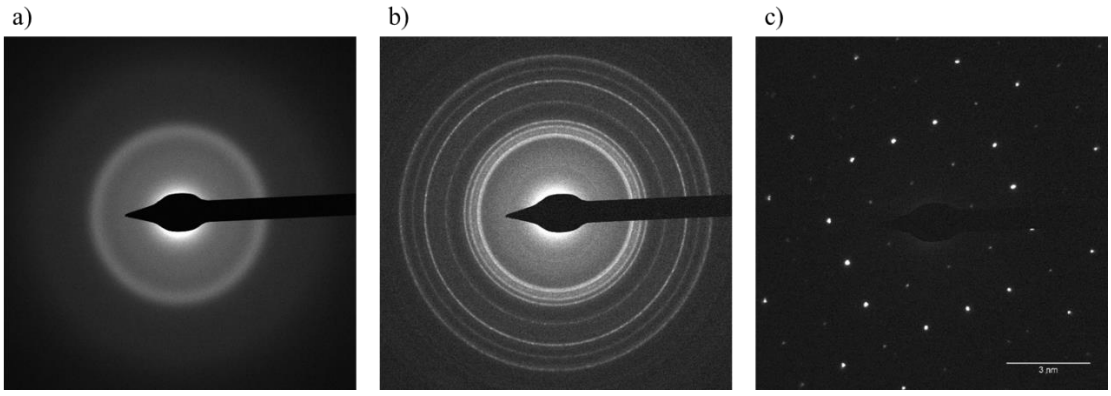

Figure 2.10. Examples of PBED patterns from thin YIG films on SiO2. (a) amorphous (b) polycrystalline (c) single-crystal

Using a parallel beam condition, the area probed for diffraction can be limited by using a selected-area aperture, known as selected-area diffraction patterns (SADP). These apertures are typically larger than 100 nm making probing isolated areas smaller than this impossible with this technique. By converging the beam down to only nanometers in size, it is still possible to obtain crystallographic information from the specimen with a technique known as convergent beam electron diffraction (CBED). Converging the beam means that the parallel beam condition is no longer satisfied. Now there are a number of incident beam angles which can coherently scatter causing discs to form on the back focal plane instead of points for a single-crystal. Though these discs can be more difficult to analyze for some information, they also can provide greater detail about the specimen in regards to strain and thickness with proper analysis. The symmetry and spacing of the reciprocal discs in CBED are the same as the Bragg spots would have in a PBED pattern.[58]

2.7.3.2 Real Space imaging

Images of the specimen can be formed by forcing the image plane to be located at the camera. In doing so, electrons which were incident on the specimen at a particular location will all reconverge to a point regardless of scattering angle unless they were lost in the column. In bright-field imaging, an objective aperture is used to block scattered electrons, only allowing unscattered electrons to contribute to the image. Another mode of imaging is dark-field imaging, where only diffracted electrons are used to create the image. Most of the imaging done in this work makes use of bright-field imaging.

There are a number of ways in which contrast can arise in bright-field imaging. One common type of contrast mechanisms is mass-thickness contrast. This contrast mechanism is most intuitive to understand. If a specimen is denser, it will have higher electron cross section, increasing the probability of scattering an incident electron. Similarly, if a specimen is thicker, it will have more chances to scatter an electron, increasing the specimen electron cross-section. Most of the work here is performed on thin films which have uniform thickness and atomic composition, meaning little mass-thickness contrast is observed.

The main mechanism of contrast in the following research is diffraction contrast. In a crystalline specimen, if the crystallographic planes parallel to the optic axis are strongly scattering, it will be more likely to coherently scatter incident electrons. In bright-field, this manifests as a darker area of the image because more of the electrons will be blocked by the objective aperture. For a nanocrystalline film, diffraction contrast will give a speckled like image with varying amounts of contrast for each grain, depending on how

close to a strongly scattering zone-axis that grain is aligned. For large, single-crystal grains, diffraction contrast can cause bend contours to appear in the bright-field image.

Bend contours are a type of diffraction contrast resulting from bending of the crystalline lattice in a single-crystal. If the crystal is bent enough such that it no longer meets a Bragg condition, electrons will no longer be coherently scattered and blocked by the objective aperture. Figure 2.11(b) demonstrates the cause of bend contours and Figure 2.11(a) shows an example of a typical bend contour in a thin film specimen.

Bend contours can provide insight into the crystal structure of a specimen even at low magnifications in bright-field imaging. By tilting the specimen, the bend contours can be seen to move as a function of the radius of the bending revealing structural information that would otherwise be impossible to gather in TEM.

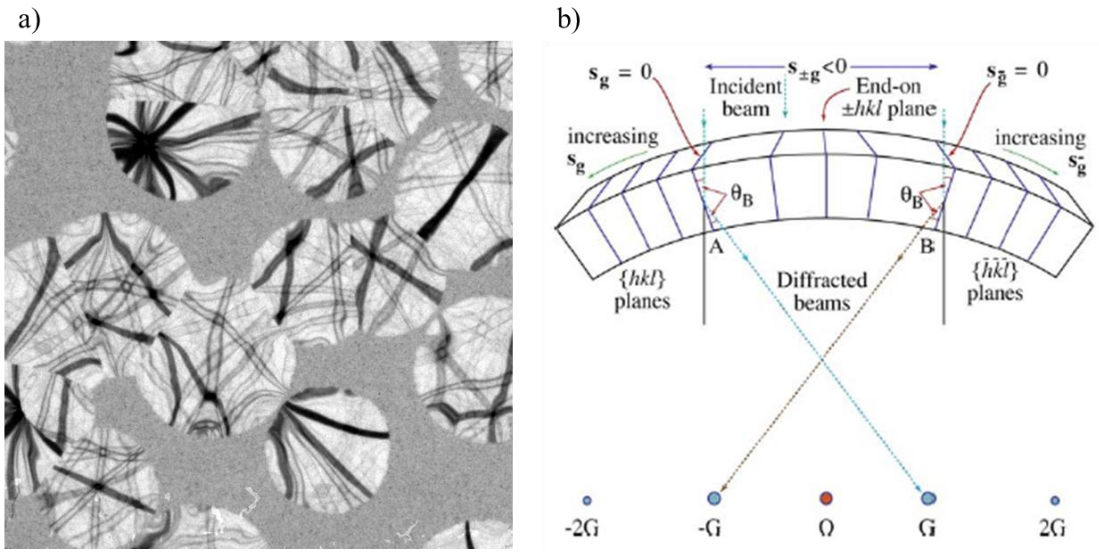

Figure 2.11. (a) YIG crystallites demonstrating bend-contours in bright field imaging. (b) Depiction of the bending of the lattice causing the Bragg condition to only be satisfied at certain locations. Adapted from Williams et al.[58]

2.8 Ultrafast Electron Microscopy Instrumentation

In this section I will describe the UEM setup at the University of Minnesota. Both the customization of our TEM and our custom laser system are explained. It should be noted that this same laser system and TEM were used when performing the preliminary *in situ* crystallization in Chapter 4, the video-rate YIG crystallization experiments in Chapter 5, and the single-shot experiments in Chapter 6.

2.8.1 TEM Column

All of the descriptions in this section relate to the time-resolved microscopy lab at the University of Minnesota which is conducted on an FEI Tecnai Femto UEM (Thermo Fisher). The microscope is similar in design to that of a FEI T20 microscope. It can operate up to 200 keV and can obtain 1.4 Å of resolution in conventional TEM mode.

The main modifications to the TEM are the addition of two optical periscopes. There is one periscope for access to the gun region and one for the specimen region. Both of these periscopes are composed of UV transparent quartz windows as well as a series of mirrors which allow for directing an incident laser beam onto either the cathode or the specimen, respectively. The first such mirror is controlled using external micrometers in both ports. The second mirrors are piezo-controlled for fine adjustments. For optical access into the gun region, a fixed mirror is used in the laser line which directs the laser beam at a 4 degree angle on to the cathode. The last mirror in the specimen laser line is a

2.5mm disc of polished aluminum. In Figure 2.12 these ports can be seen as additions to the standard TEM column. Also attached to the column is an optical board where power meters and focusing lenses can be mounted.

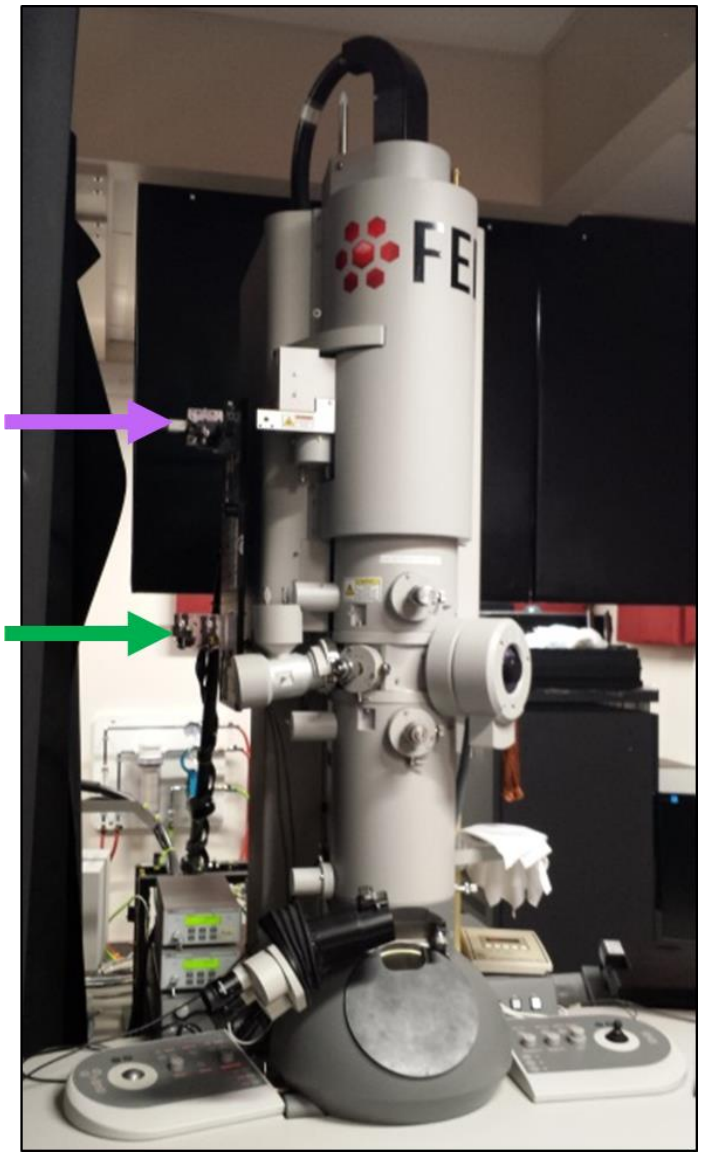

Figure 2.12. Picture of our custom TEM column. The top arrow points to the gun periscope and the bottom arrow points to the gun periscope.

We also have a specially installed condenser aperture which is much larger than what is standard. Our aperture is 1.25 mm in diameter, and we observed a factor of eight increase in electron counts when compared to the 200 μm aperture, the next largest aperture. This does lead to a loss in coherency, though the increase in electron counts allows for higher spatial resolution in most UEM experiments.

2.8.2 Gun Region

The gun region of our TEM is standard except for two significant changes that we have made in order to operate with a higher electron count. The first such modification is the use of a larger diameter Wehnelt aperture. The standard Wehnelt aperture is between 1 and 0.3 mm in diameter. Our custom Wehnelt is 2 mm in diameter and was shown to increase the photoelectron count at the detector by an order of magnitude. This is thought to allow for a higher collection efficiency based on work by Kieft et al.[61] There is an expected loss of temporal coherency due to a larger energy spread in the electrons. The second modification is the use of larger cathodes for electron generation. In this work, we use a 150 um diameter flat (100) LaB_6 tip while the norm is close to an order of magnitude smaller and can have varying geometries. The larger tip size allows for a higher number of electrons to be generated during a single laser pulse at the sacrifice of spatial coherence of the electron beam. Not used in this work but commonly used by our group are carbon coated tips which help to eliminate sidewall emission from the tip and assist with increased stability and coherency of longer stroboscopic UEM experiments.

2.8.3 Laser System

Typical TEM setups do not include any laser systems. Because we operate a time-resolved setup with a pump-probe condition, our system is reliant on these laser systems to both create photoelectrons for imaging as well as excite our specimen into a transient state. Our laser system consists of two separate lasers. I will discuss the lasers as they relate to single-shot experiments, but the same lasers and configuration are used for stroboscopic experiments as well.

2.8.3.1 Pump Laser

The laser used for specimen excitation is a diode-pumped, ytterbium-doped potassium gadolinium tungstate (Yb:KGW), solid state laser (PHAROS, Light Conversion). The maximum average power is 6 W and can operator from single-pulse mode to 1 MHz in frequency. The maximum pulse energy of the PHAROS laser is 200 µJ at a fundamental wavelength of 1,030 nm. The pulse duration at this wavelength has been measured to be 700 fs by autocorrelation. The pulse duration can be adjusted with a compressor setting allowing for longer pulses but not to the point where the pulse duration will be comparable to that of the probe pulse. In this regard, the instrument response will be solely dictated by the duration of the electron packet in single-shot mode. The Pharos laser pulses immediately enter into a multiharmonics module (HIRO, Light Conversion), which can output the fundamental, doubled (515 nm) or tripled (343 nm) wavelength in a variety of co-linear and wavelength separated beams. Any of these wavelengths can be selected for exciting the specimen. The selected wavelength laser line is directed through

a series of mirrors onto an elevated table which is used to guide the pulses into the specimen periscope. Before entering the periscope, the laser passes through a focusing lens attached to a micrometer which focuses the laser at the specimen. The laser spot size has been calculated to be 60 µm FWHM at the specimen and is Gaussian in profile.

2.8.3.2 Probe Laser

A second laser is operated for producing optical pulses which are used to excite photoelectrons at the cathode for imaging. Here, a Q-switched, neodymium-doped yttrium aluminum garnet (Nd:$Y_3Al_5O_{12}$; Nd:YAG) laser (Wedge HF, Light Solutions) is used. This laser has a pulse duration of 700 ps and a fundamental wavelength of 1,064 nm. It has a maximum output pulse energy of 180 µJ and can be operated between single-shot and 100 kHz in frequency. Immediately after output, the laser is sent through a frequency doubling crystal to convert from the fundamental frequency to 532 nm. This is done by passing the beam through a lithium triborate (LiB_3O_5; LBO) crystal (3 x 3 x 10 mm, Eksma Optics). The 532 nm light is then frequency doubled again to obtain 266 nm ultra-violet (UV) light. This is done by passing the beam through a beta barium borate (B-BaB_2O_4; BBO) crystal (5 x 5 x 0.4 mm). The UV wavelength is needed to efficiently excite photoelectrons above the bandgap for LaB_6. The probe-beam then gets raised to the top laser table and directed up and into the gun-region periscope. The beam passes through a focusing lens attached to a micrometer such that the laser fluence can be adjusted on the LaB_6 crystal.

2.8.3.3 Laser Timing

To perform pump-probe experiments, the timing between a pump laser pulse being incident on the specimen and a probe electron packet passing through the specimen needs to be well defined and controllable. While no time-resolved experiments were performed as part of this work, a system in which they could be has been established.

In order to precisely control the timing of the pulses, we use a digital delay generator (DG353, Standford Research Systems). The pump laser (PHAROS) is set to operate at a frequency of 200 kHz, but is pulse picked down to 1 Hz. The PHAROS is able to provide a signal when it opens the pulse picker, effectively at the same time as the pulse leaves the laser. This signal is then read into the delay generator which provides a certain delay to the signal it sends to the probe laser (HF Wedge) to trigger in single-shot mode. By using two optical diodes attached to an oscilloscope, the timing of these pulses can be visualized. Because of electronic delay, we need to use a delay as follows:

$$t_{input} = 1 \pm t_{path} \pm t_{exp}$$

The variable, $t_{\text{input,}}$ is the delay entered into the delay generator, t_{path} is the intrinsic delay generated by differences in laser path length and electronic lag, and t_{exo} is the desired experimental offset from a projected time zero. By correctly setting $t_{\text{input,}}$ it is possible to overlap the pump and probe pulses with the desired delay in a steady state 1 Hz pulse train. By opening mechanical shutters of both the probe and pulse line simultaneously for one second, we are able to capture a single pump and a single probe pulse, thus satisfying the single shot experimental condition.

There is timing jitter in the signaling electronics resulting in the pulses being separated by values on the order of 10 ns from what had been previously calibrated. This timing jitter can be captured and reported by picking off part of the pulses and seeing the precise delay on the oscilloscope limited only by the temporal resolution of the oscilloscope.

To further improve the accuracy of the reported experimental delay, a method for measuring the delay of the electrons from photoemission to interacting with the specimen needs to be established. This would require visualizing material dynamics. Also, by using experimental dynamics, the instrument response could be calculated.

2.8.3.4 Pump Alignment

The alignment of the pump laser is important for both pump-probe experiments as well as *in situ* laser heating experiments. It is a fairly trivial process of aligning mirrors to have the pump laser enter the specimen periscope. From here, the alignment and characterization of that alignment becomes more difficult. There is no way to visualize the pump on any of the internal periscope mirrors or on the specimen except using the electron beam. We have developed a means by which to align the pump laser without venting the chamber.

A first rough alignment needs to be done with the specimen region vented and a 3 mm piece of paper inserted into the specimen holder. From here the laser can be aligned through the periscope onto the paper through traditional alignment techniques. By maximizing the brightness of the laser on the paper, clipping on the internal mirrors is

minimized. Once the laser is successfully aligned to the 3mm specimen holder region, the column is pumped down. Using a 200-mesh TEM grid with a Quantifoil amorphous carbon film, the laser can be more precisely aligned. The specimen needs to be moved to eucentric height in real space imaging mode. This is critical due to the angle at which the pump laser is incident on the specimen. By using a pump laser fluence of 0.1 mJ/cm2, the Quantifoil can be burned which visualizes as a light spot on the TEM grid. Using the micrometers on the focusing lens, the burned area can be directed to the center of the viewing area. This provides a good alignment which has experimentally been shown to be within 10 μm. For some of the following experiments, finer adjustments were necessary. The burned area seemed to be sensitive to the conduction of the local copper grid bars and regularly disagreed with experiments on SiO_2 TEM windows. As such, a more refined method was developed.

An oriented gold film calibration specimen was used for the more precise alignment. Once the rough alignments have been made, the laser power was set to 200 kHz and an average power of 5 mW. Using the green (515 nm) wavelength, the gold film was heated and this heating was observed by the expansion of Bragg spots in diffraction mode. Using the smallest selected area aperture (200 nm) centered on a grid square, the role of thermal diffusion is minimized in terms of spatial error. Going to the longest possible camera length on a low order diffraction spot, we are most sensitive to thermal changes. When changing the specimen periscope micrometer X and Y positions by micrometers, obvious changes can be seen to the position and intensity of the diffraction

spot. Submicron positioning of the focusing lens is possible by maximizing the apparent Bragg spot changes. This method was the only means by which the pump could be placed reliably with micrometer accuracy on the specimen.

2.8.3.5 Probe Alignment

The alignment of the probe is critical to getting high photoelectron emission and should be performed without any specimen obstructing the electron beam path. The first step in aligning the probe laser is enacted when a new tip is inserted and the gun region is at atmosphere. A special alignment tool is placed into the column which has a cross hair where the Wehnelt aperture is located during operation. By aligning the laser using standard alignment techniques to the crosshair and maximizing for intensity, clipping on internal mirrors is minimized. After the gun region is pumped back down to vacuum, the thermionic electron beam is aligned and tightly focused. The thermionic heating value should then be lowered such that there is no more thermionic emission. Operating the probe laser at 10 kHz, we allow the laser to be incident into the gun region. By rastering the micrometers of the focusing lens, an electron beam of photo-emitted electrons can be found once the laser becomes incident on the tip. It is important to make sure that the emission is coming from the tip and not the Wehnelt aperture which can also emit electrons. This is easily confirmed by rastering the laser across the tip and seeing the circle like geometry of tip emission and not the ring character emission from the Wehnelt. Standard TEM alignment procedures should then be performed with the photoelectron beam.

2.9 Finite-Difference Heating Model

Fourier's law describes how heat is conducted in a material over time and is given below for the one dimensional case.

$$\frac{\partial T}{\partial t} = \alpha \frac{\partial^2 T}{\partial x^2}$$

Here, the time derivative of the temperature is a function of the second derivative of the spatial gradient. In more simple terms, the rate at which something cools or heats is proportional to how quickly the temperature is changing in space across it. There is a thermodynamic driving force to minimize temperature gradients.

Numerical models can be used to apply this equation to an experimental setup in the form of a finite-difference (FD) model. In an FD model, only certain times and spatial locations are solved in a grid which is representative of the behavior of the system. There are multiple ways in which to solve for the temperature at each grid location using an implicit or explicit solution. In this work an explicit forward stepping solution has been used to evolve the system in time according to Fourier's law. The time domain is not discretized, but the spatial domain is. A first order approximation of the second derivative of the temperature with respect to space is applied to Fourier's law. In this way, the discrete spatial elements can be used to solve for the time derivative as shown below with an Euler approximation of the second spatial derivative.

$$\frac{\partial T}{\partial t} = \alpha \frac{(T_{j-1} - 2T_j + T_{j+1})}{\Delta x^2}$$

The experimental system we wish to consider with this model has a radial symmetry. We can apply a one dimensional model to this system, but must account for the change in the area that each spatial grid point is representing, as shown in Figure 2.13. This is accounted for by introducing an extra term in the approximation shown here

$$\frac{\partial T_j}{\partial t} = \alpha \frac{\left(j + \frac{1}{2}\right)\left(T_{j+1} - T_j\right) - \left(j - \frac{1}{2}\right)\left(T_j - T_{j-1}\right)}{j * \Delta r^2}$$

In this way, the increase in thermal diffusivity is included as the radii increase with the index of the point being considered. The amount the currently considered spatial point is affected by radii farther or closer to the center is weighted. The implementation and experimental value of this model are discussed in Chapter 5.

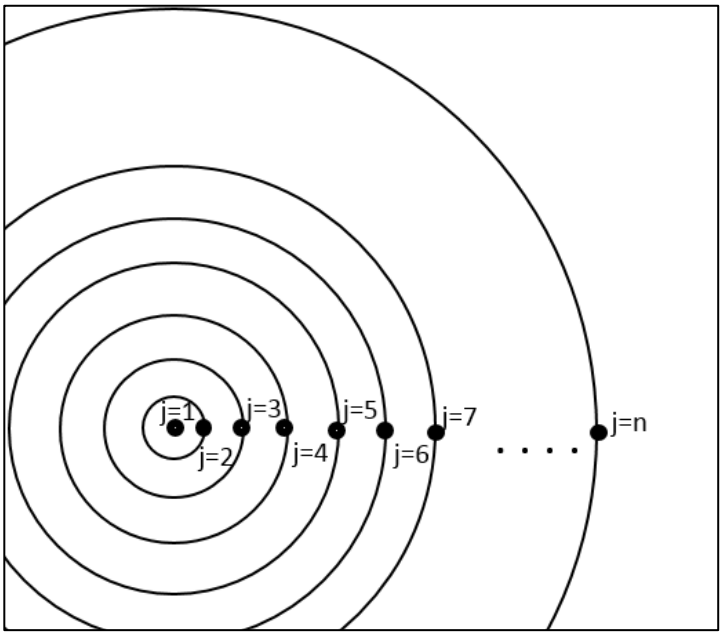

Figure 2.13. Depiction of the radial grid used in the finite- difference temperature model. The indices start at 1 in the center and increase as the radius of the model increases.

3. Chapter 3 – YIG: Thin Film Structural Observations

In this chapter a detailed description of the YIG film structure is provided. *Ex situ* RTA and *in situ* laser annealing methods were used to transform amorphous YIG films on both silicon wafers and SiO_2 TEM membranes into a crystalline state. The process of creating and characterizing the as-deposited films is detailed. After annealing, the microstructure and nanostructure of the resulting films are described. This work is the first plan view TEM study of YIG film structure. Here we investigate previously unreported phase and microstructure information about the YIG films. This chapter contains data and images from multiple specimen and observations which were made over the course of my PhD work. The descriptions below are applicable to all YIG films I have created unless noted.

3.1 YIG Film Growth

3.1.1 Deposition

Amorphous YIG films were deposited at room temperature in all studies using RF reactive sputter deposition. A Y:Fe (3:5) metallic composite target was sputtered controlling the forward power, set at 240 W. The chamber base pressure was recorded to be between $8x10^{-6}$ and $2x10^{-5}$ Torr. A mixture of Ar and O_2 was flowed into the deposition chamber. The exact flow rates of Ar and O_2 were changed over the course of this thesis in

order to optimize deposition rates, however, the ratio of $Ar:O_2$ was kept at 10. The sputtering stage was rotated at a rate of at least one rotation per three seconds. This yielded a deposition rate of between 0.5 and 4 nm/min depending on a number of factors including target thickness, vacuum pumping rate, and the condition of the target. The thickness of the YIG films used in each study is reported in that section.

Energy dispersive spectrometry was used to evaluate the ratio of Fe to Y in the deposited films to ensure the correct stoichiometry for YIG was achieved. Our EDS system was not able to resolve the Y and Si peaks without overlap which can affect the quantitative analysis of the composition when attempting to determine the composition when the film is on a Si based substrate. To avoid the issue with the Si signal, thick films (>100nm) were deposited on copper tape and the spectrum acquired from these films. A 3:5 Y:Fe ratio was confirmed within the expected error for all depositions.

3.1.3 Substrates

Two different substrates were used in this thesis for studying YIG films. For the TEM studies, a windowed TEM grid (TEMwindows.com) with a 40 nm amorphous SiO_2 membrane over the windows was used. These membranes were selected because they most closely match the chemical interface the YIG films would see on silicon device because of the native oxide layer. The SiO_2 membrane is also chemically inert to temperatures over 1000 °C according to the manufacturer. While there are 20 nm membranes available, the 40 nm membranes provided greater mechanical stability which was important during the deposition and subsequent annealing processes where stress can cause the membrane to

tear. The geometry of these windows is shown in Figure 3.1. The TEM grids were untreated prior to deposition.

For XRD measurements as well as thickness measurements, films were deposited on undoped (001) silicon wafer pieces. The silicon pieces were cleaned prior to being put into the deposition chamber with a standard cleaning process. They were sonicated for three minutes in acetone and subsequently sonicated for three minutes in IPA. The wafer pieces were then rinsed with distilled water and rapidly dried with an air gun. They were then placed into the sputtering chamber. This work was not performed in a cleanroom and some dust and contamination were seen on the films. Because most of the measurements concerning the silicon wafer pieces were large-area, a limited number of dust particles or other contaminates is not expected to affect the results.

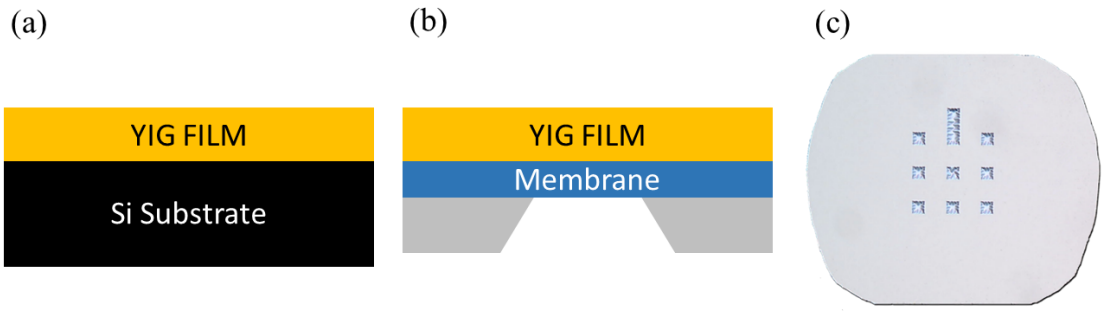

Figure 3.1. Representation of (a) YIG film on a silicon wafer (b) YIG film on TEM window grid membrane. (c) Plan view of a TEM window grid.

3.2 YIG Crystallites

3.2.1 Bright-Field Imaging

To benchmark typical microstructures and nanostructures, YIG films were deposited on TEM grids with SiO_2 windows and imaged before and after standard annealing (RTA at 800 °C for 3min in N_2), shown in Figure 1(a and b, respectively). Figure 1(a) verifies that films were amorphous as-deposited. There were no structural features in the bright-field images, and the diffraction pattern shows a single diffuse ring due to a regularity in interatomic spacing typical in glassy structures.[62] After annealing, Figure 1(b), the microstructure was similar to that typically seen in integrated YIG films by optical microscopy and SEM/EBSD in previous publications.[63] Micrometer-sized crystallites (1-2 μm) were observed in a seemingly amorphous matrix. These crystallites contained the desired garnet phase, but they only accounted for ~80% of the sample area. However, because the YIG regions were highly crystalline, they were strongly diffracting and accounted for almost all of the intensity in the diffraction pattern, Figure 1(c). The angular intensity of the diffraction pattern was uniform, suggesting that the crystallites had no preferred in-plane texturing. The characteristic dark streaks throughout the crystallites arise from bend contours, a common diffraction-contrast feature in single-crystal films.

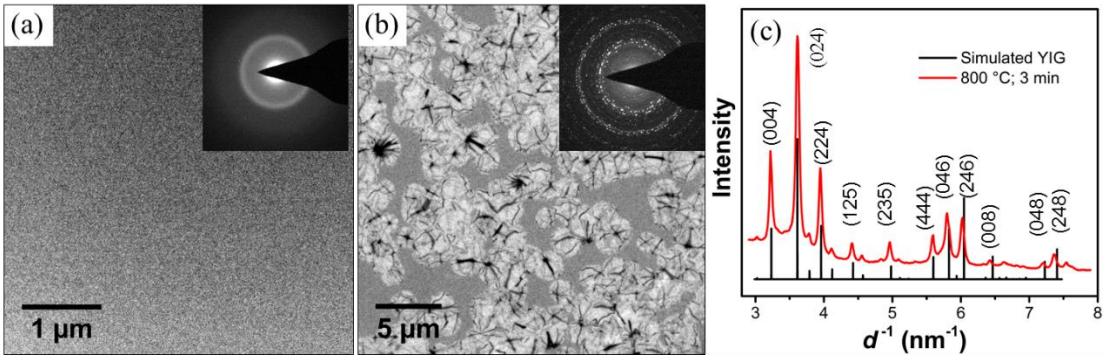

Figure 3.2. Bright-field TEM images and accompanying diffraction patterns of (a) as-deposited film and (b) RTA-annealed film (800 °C, 3min). Note: dark streaks in crystallites are a common diffraction-contrast feature in single-crystals. (c) Radial integration of diffraction intensity for annealed film compared to simulated YIG data. Adapted from Gage et al.[33]

The YIG crystallites are single-crystal in nature. This is an important discovery because many applications are negatively affected by grain boundaries. Other publications on YIG film crystallization have used the Scherer formula in XRD studies to report grain size.[64-66] This has resulted in grain sizes close to the thickness of the film being attributed to the full grain geometry when in reality the width and thickness of the grains are very different. Along with the bend contours being indicative of the single-crystal nature of the YIG crystallites, diffraction and HR-TEM methods were used to confirm this discovery.

3.2.2 Diffraction

Utilizing a selected-area aperture, a single-crystallite can be probed in diffraction mode in the TEM. Figure 3.3 shows the resulting diffraction pattern from a grain oriented along the (001) zone axis. This experimental pattern differs from the simulated pattern due

to the expected effects of a dynamic beam condition in the TEM for a specimen of this thickness. The relative positions and angles of all Bragg spots are as expected, however, disagreement in intensity and allowed reflections are a result of diffracted beams acting as the main beam. Because of the random orientation of the crystallites, the SADP from each crystallite will look different, however, they can all be tilted to achieve a low zone-axis and demonstrate the single-crystal nature. The bending of the grains can lead to multiple zone axes being present in a pattern, but this does not mean there are more than one grain in the selected area.

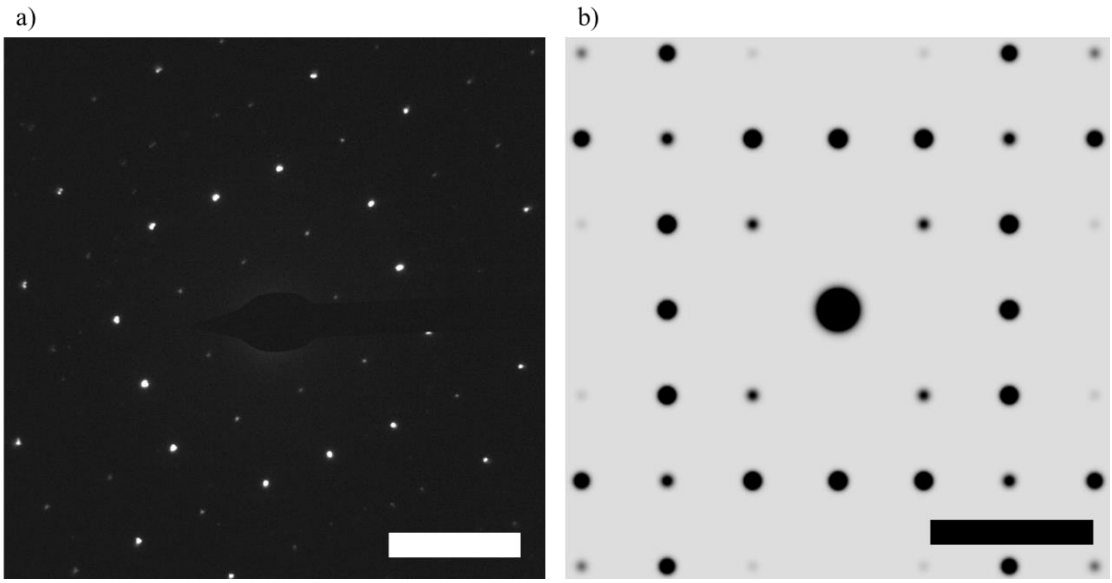

Figure 3.3. (a) Selected-area diffraction pattern of a YIG crystallite. Forbidden reflections are present due to a dynamic beam condition. (b) Simulated diffraction pattern of YIG down the (001) zone-axis. Scale bars are $3nm^{-1}$.

3.2.3 HR-TEM Imaging

High resolution TEM can also be used to show the crystalline ordering of the YIG crystallites. Figure 3.4(a) shows the lattice fringes of a YIG crystallite oriented along the (101) zone axis. This figure was obtained using a 45nm YIG film which was laser annealed. Figure 3.4(b) shows the Fourier transform of 3.4(a) image. We see high agreement between the lattice spacing and the orientation of the FFT lattice spots compared to simulation confirming the YIG single-crystal structure.

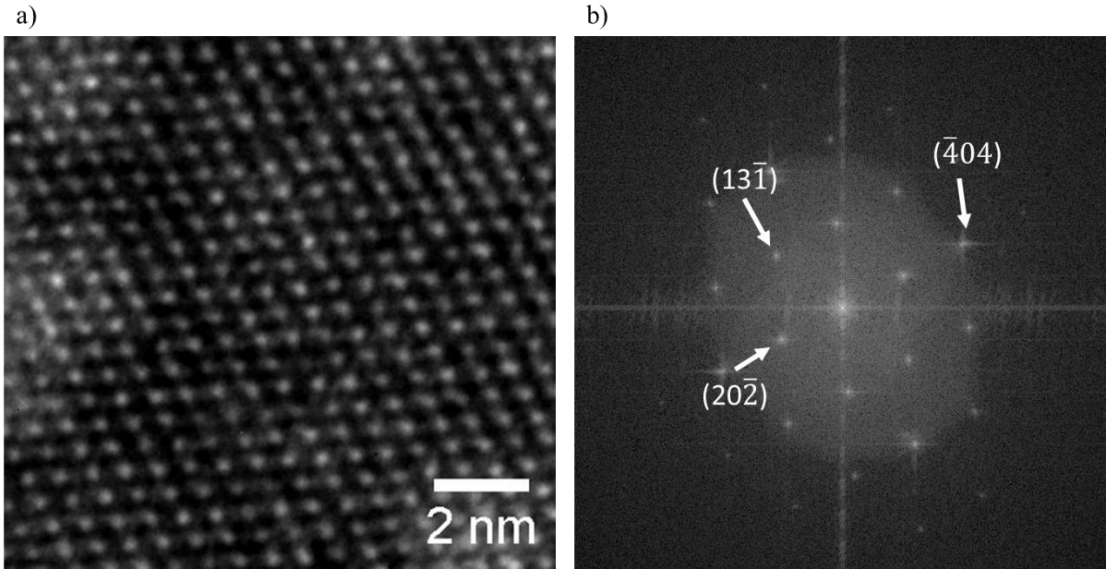

Figure 3.4. (a) HR-TEM image of a YIG crystallite. (b) Fast Fourier transform (FFT) of the HR-TEM image indicating regularly spaced lattice sites. FFT spots are labeled according to corresponding interplanar spacings in YIG.

3.2.4 Bend Contours

The characteristic dark streaks throughout the crystallites arise from bend contours, a common diffraction-contrast feature in single-crystal films. Figure 3.5(a) shows that as

the specimen is tilted, the dark bands move with relation to the crystallite. This motion is caused by a spatially-varying Bragg condition that occurs as the bent reciprocal lattice (stemming from a slight bending of the real-space lattice) is rotated with respect to a fixed Ewald sphere. The local curvature of individual crystallites may be due to ripples across the SiO_2 TEM grid membrane the film was grown upon. It may also be indicative of the true crystal structure in the films, a slight bend across its width in relation to the substrate. All grains observed are bent such that the center of the radius of curvature lies above the film.

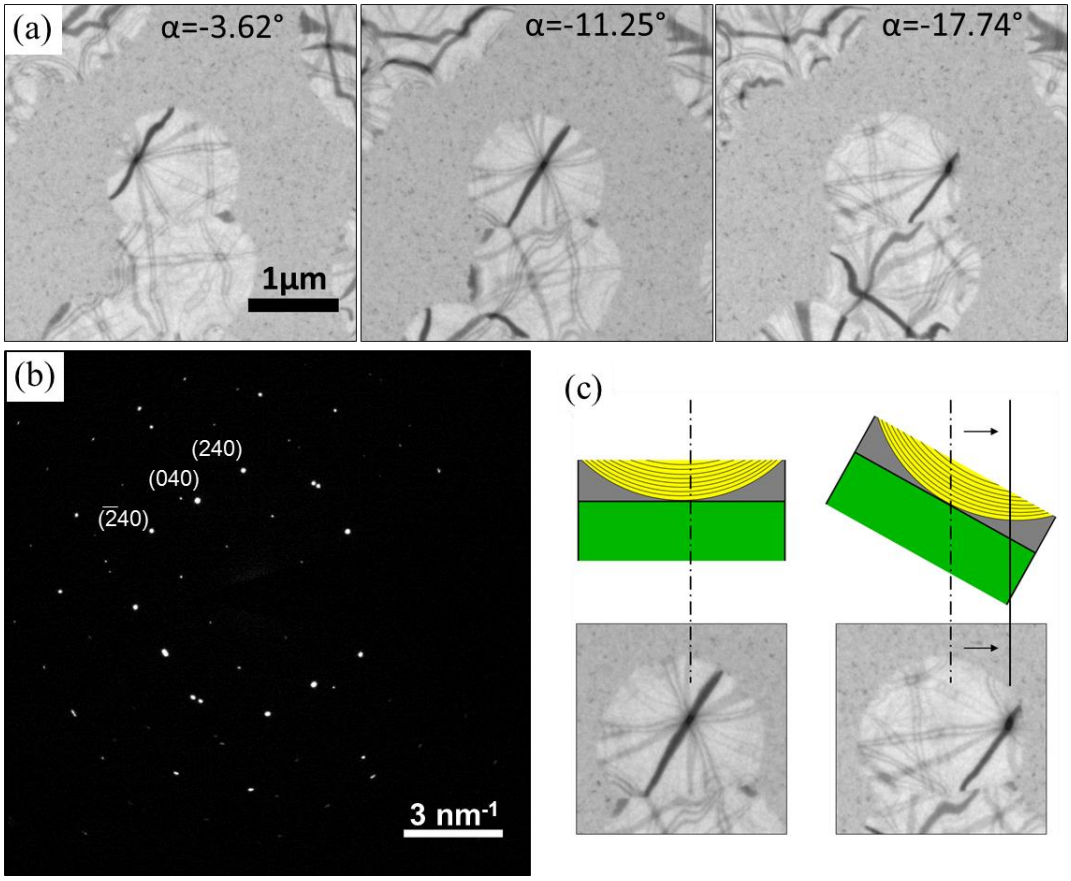

Figure 3.5. (a) YIG crystallite imaged at different tilt angles demonstrating the movement of the bend contours. (b) SADP from the imaged crystallite (c) Cartoon description of how tilting can align different areas of the YIG crystallite to the optic axis causing higher scattering and lower intensity in bright-field.

3.2.5 SEM and Optical Micrographs

The requirement for a TEM specimen to be less than 100 nm in thickness necessitates that we cannot examine the crystallization of a YIG film on a bulk substrate with TEM. It also means in order to use TEM we must make some modifications to the

system we wish to examine. Instead of a SiO_2 on Si system, we are only able to use a 40nm unsupported membrane of SiO_2. In order to compare our results on the TEM grid with those on the Si wafer, SEM and optical microscopy were used. In Figure 3.6, both the SEM micrograph and optical microscope images are similar to the geometries we observe in the TEM images. This leads us to believe we are sound in extrapolating the TEM findings to those of a YIG film on a Si wafer.

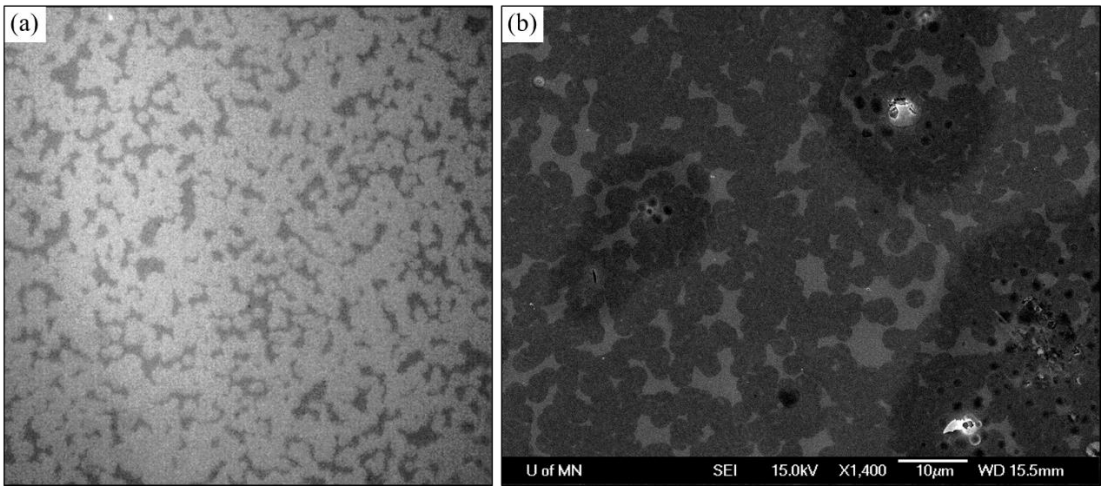

Figure 3.6. (a) Optical microscope image of a YIG film on a silicon wafer. Light regions are the YIG phase. (b) SEM micrograph of a YIG film on a silicon wafer. Dark regions are the YIG phase.

3.2.6 Summary

In this section, we have shown that the as deposited amorphous films have partially transformed into the YIG phase. The YIG crystallites are microns in diameter, are single-crystal in nature, and are randomly oriented. This is important because it implies that it is

possible to create single-crystal YIG domains in thin films (<40nm) which is approaching the spatial dimensions for potential devices. The dynamics of this phase transformation are addressed in later chapters.

3.3 Nanocrystalline Matrix

An important discovery made during the course of this thesis was the presences of a nanocrystalline matrix between the YIG crystallites. Previous work had not reported this structure and rather assumed un-crystallized material remaining in the film after YIG crystallization.[34, 67-68] This was the first plan-view TEM study of thin YIG films. Other studies have missed the nanocrystalline phase due to the characterization tools they used or by using other deposition techniques. Thicker films made by liquid phase epitaxy (LPE) often are porous and have a three dimensional structure instead of a two dimensional thin film structure.[23, 69] XRD can miss nanocrystallinity because the diffracted signal is low. The YIG phase will have a much higher signal, and if the XRD measurements are stopped when appropriate signal has been reached for the YIG phase, the nanocrystalline phase may not appear in any statistically significant way. SEM and optical microscopy imaging techniques do not have the same contrast mechanisms or spatial resolution which would make imaging the nanocrystalline phase plausible.

3.3.1 Bright-Field Imaging

The first observations of the nanocrystalline matrix were made in bright-field TEM imaging of the YIG films. If the material was amorphous between the YIG crystallites, no contrast would be observed in the region. Instead, a speckled variation in intensity was seen with spatial contrast variation seen on the order of nanometers. Here, a 40 nm YIG film is examined. Utilizing the high spatial resolution, we were able to more closely investigate this region. Figure 3.7(a) shows a bright-field micrograph of the interface between a YIG crystallite and the nanocrystalline phase. Tilting of the specimen causes shimmering of the intensity in this area confirming that the contrast is due to diffraction contrast from grains being oriented along different zone axis with different amounts of coherent scattering. Figure 3.7(b) shows a HR-TEM image of the interface. The nanocrystalline phase is on the left in this image with grain sizes on the order of 10 nm. This grain size was seen consistently in the films and did not seem to be affected by film thickness or annealing temperature. Moiré fringes can be seen, indicating the presence of stacked grains. On the right, the YIG phase is observed as in relatively uniform intensity because there is no diffraction contrast owing to the single-crystal nature and negligible bending over a region of this size.

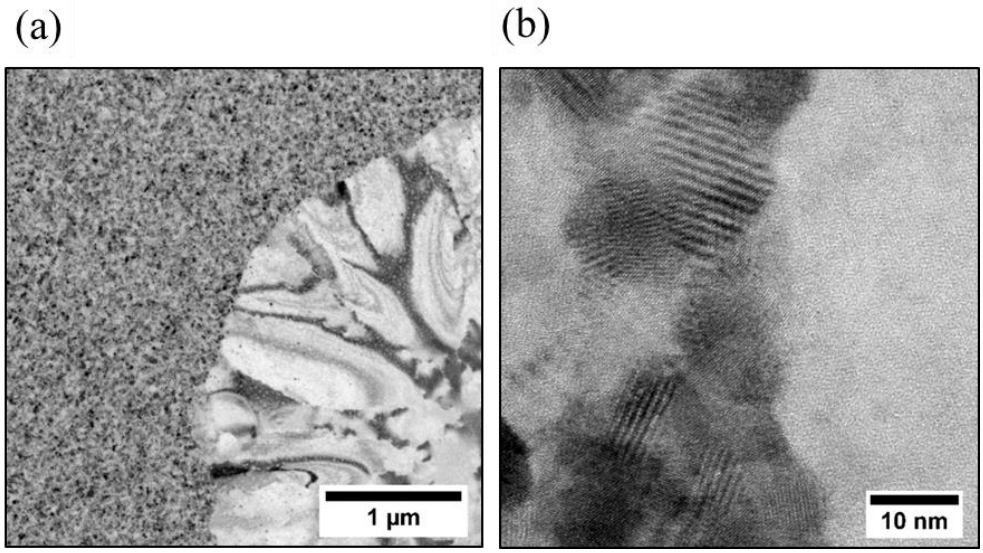

Figure 3.7. (a) Bright-field image of the border between a YIG crystallite and the nanocrystalline matrix phase. (b) HR-TEM image of the same interface showing the bumpy nature of the transition between the phases.

3.3.2 Diffraction

Diffraction patterns of the nanocrystalline phase were obtained using selected-area diffraction, isolating the signal from only the desired phase region. Even with the smallest selected-area aperture (200nm), signal from hundreds to thousands of grains is obtained leading to rings at the back focal plane. The radii of the rings is inversely correlated to the interplanar spacing as described in Section 2.7.3. This provides us with structural information about this nanocrystalline phase.

3.3.2.1 Texturing

Diffraction studies of the nanocrystalline phase provided information about the crystal structure and, specifically, crystallographic texturing of the nanocrystals. An early observation of the nanocrystalline phase in diffraction space was that tilting of the specimen about an in-plane axis led to bunching of the azimuthal intensity of the diffraction rings. Figure 3.8 shows the effect of tilting on a 25 nm specimen (RTA, 3 min, N_2). Because the intensity is uniform when the electron beam is perpendicular to the surface and changes only when the specimen is tilted, the specimen has a strong out of plane texturing. This means that the grains have a preference to align along a particular zone axis aligned perpendicular to the surface of the film. The continued presence of intensity around the entirety of the rings even when tilted means that the texturing is not absolute and some grains do not follow the texturing direction.

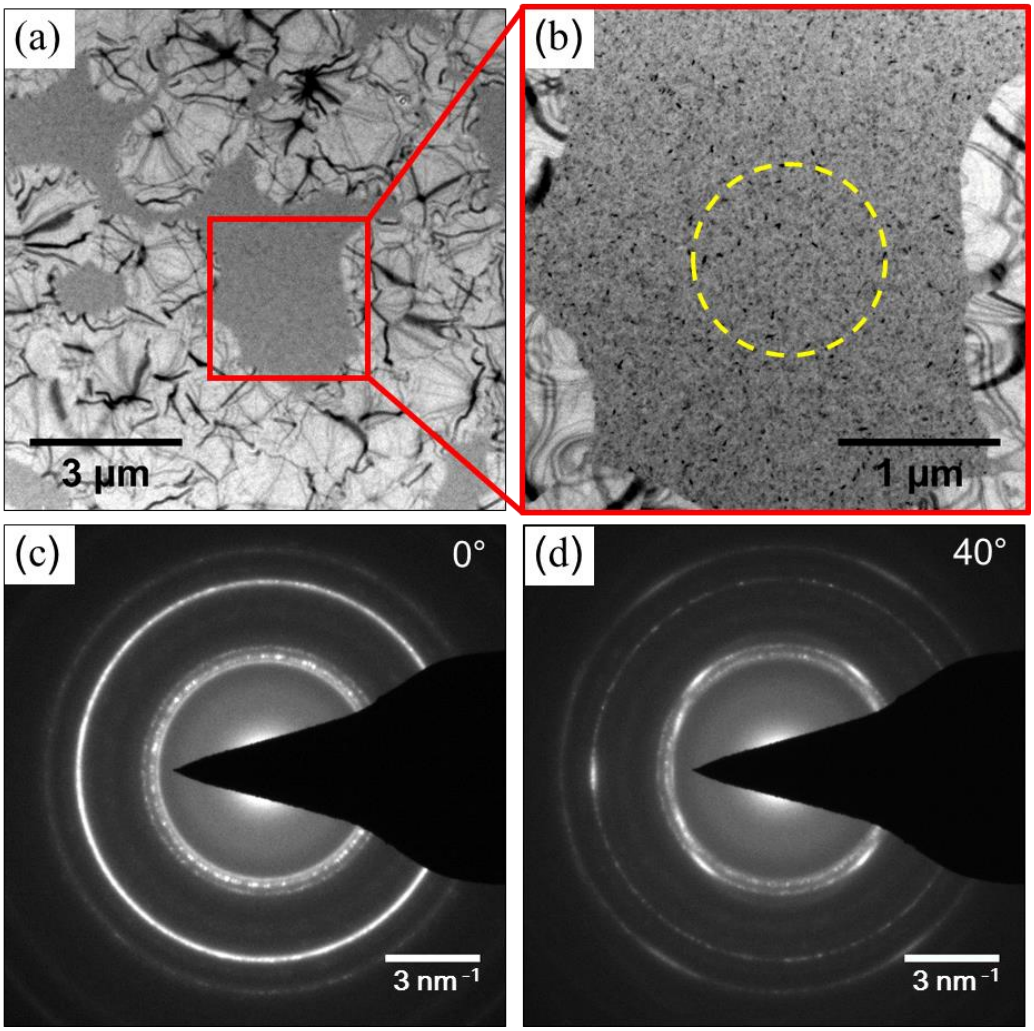

Figure 3.8. (a,b) Bright-field TEM images of the inter-YIG matrix phase present in films produced by standard anneals. The yellow circle in (b) shows the area from which SADPs were obtained. SADPs obtained at (c) 0°, showing no in-plane texturing and (d) 40°, suggesting out-of-plane texturing.

The texturing seen here was not seen in all films. Specifically, the films studied in Chapter 5 did not display any texturing of the nanocrystalline film. Other films which were laser annealed did display out of plane texturing but a rigorous study was not performed to

determine any possible differences which could explain when the nanophase is textured or not. Two possible factors which could account for the change in behavior are the thickness of the film and temperature gradient during annealing. Laser annealing heats the film largely by internal heat generation while the RTA heats the Si support wafer which then conducts the heat to the film on the free-standing membrane. It is also possible that the texturing is only evident when films are thick enough to have grains nucleate away from interfaces which may interfere with growth along certain crystallographic directions. This plan-view TEM study is not able to probe the morphology of the film in the out-of-plane direction. Further studies, possibly cross-sectional TEM, are needed to better understand the out-of-plane morphology of the nanocrystalline phase.

3.3.2.2 Phase analysis

The ternary system of Y-Fe-O has a number of possible phases which it can form as shown in Figure 3.9. YIG lies at one edge of the triangle, and, though it is thermodynamically stable, it must overcome a high energy barrier to form.[70] Work previous reported by Sung et al. reported that it is possible to achieve the garnet phase without being exact with the reactant stoichiometry, but like other studies, relied on XRD to perform phase analysis.[68] Here, we have quantified the ratio of Y:Fe as outlined in the sputtering section, but we are unable to report the percent oxygen in our films due to the high degree of error in oxygen measurements using EDS.

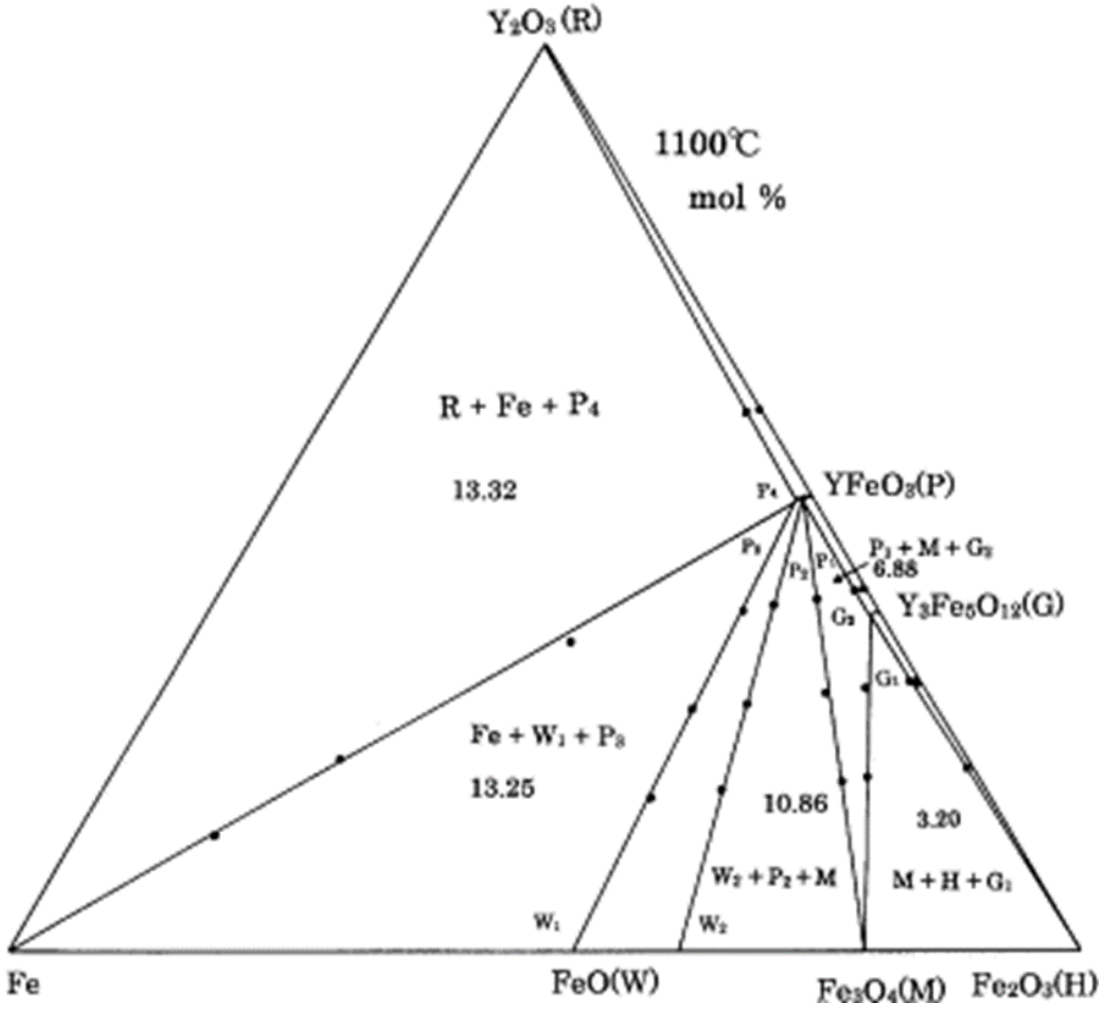

Figure 3.9. Ternary phase diagram for the Y-Fe-O system. The YIG phase is represented by (G) and lies on the far right (fully oxygenated) side of the triangle. Adapted from Kitayama et al.[71]

By comparing the azimuthally integrated intensity from the selected area diffraction pattern of the nanocrystalline phase, along with the texturing information, we can make informed theories of the crystallographic structure in this region. Phase determination for a complex, thermodynamically unstable system in this manner is challenging. Strain due

to the high temperature crystallization process can distort the lattice away from what is reported in literature and texturing can make intensity matching between experimental and known phases difficult. There are six reported ternary phases for the Y-Fe-O system and dozens of possible phases when considering there could also be iron and yttrium oxides. No known phase fits the observed diffraction information exactly, however, we can make an informed hypothesis about the composition of the nanocrystalline phase, assuming we have at most two known phases, as outlined below.

Here, it should be noted that other crystallization studies of sol-gel preparation of Y-Fe-O films and particles have observed intermediary phases before achieving the YIG phase during annealing.[72-75] These studies had YIG grain sizes on the same order as other phases because of the preparation techniques, unlike what has been observed from sputtering thin films. Four phases have been reported as intermediaries by other studies. A tetragonal $Y_3Fe_5O_{12}$ phase has been reported as a possible intermediate phase.[76] Though it is a fair fit to our diffraction pattern as seen in Figure 3.1(a) and has the correct stoichiometry, the directionality of the texturing would not be expected. The strong peak we see which has its intensity move commensurately with tilting would be the (326) zone axis. This is not a high symmetry zone axis and it would be unusual to see texturing in this direction. This phase is not well reported on and has only been mentioned in a couple of studies.[76-77]

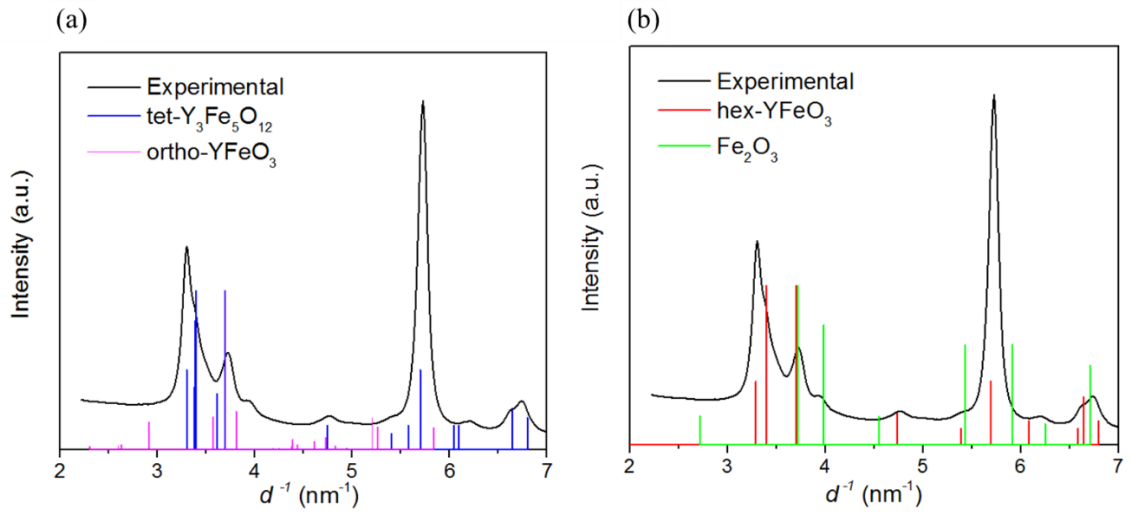

Figure 3.10. Azimuthally integrated intensity for the nanocrystalline phase SADP compared to known phases (a) tetragonal-$Y_3Y_5O_{12}$ and orthorhombic-$YFeO_3$ (b) hexagonal-$YFeO_3$ and Fe_2O_3. Simulated diffraction patterns of known phases taken from JCPSD [00-046-0891], [01-073-1345], [00-048-0529], [00-002-0915] respectively.

Most commonly, the transient phase is reported to be an orthorhombic $YFeO_3$ phase.[73-75] This structure is ruled out due to its poor fit to our measured diffraction patterns. There is little agreement between any of the peaks in the model and our experimental data in Figure 3.10(a). Another $YFeO_3$ phase which has been reported as forming in stoichiometric YIG precursors is the hexagonal phase. This phase is thermodynamically unstable but is favored for formation in the $YFeO_3$ system.[77-78] The hexagonal $YFeO_3$ has gained interest in its own right for properties including its magnetic structure[79-80] and its chemical properties, particularly when doped.[77] It fits well to our experimental diffraction

pattern seen in Figure 3.10(b) with intensity variations to be expected due to texturing and multiple beam effects in the TEM.

The hexagonal $YFeO_3$ phase is not stochiometrically the same as our measured film. If the hex-$YFeO_3$ phase were to form, we would be left with an iron rich film. This may be explained by the presence of a Fe_2O_3 phase which would also account for the only major peak which cannot be attributed to the hex-$YFeO_3$ phase. The Fe_2O_3 phase is also fit to the experimental data in Figure 3.10(b). The presence of an iron oxide phase could balance the stoichiometry to match that of the YIG phase. With a multi-phase system the relative intensities of the two phases would be determined by their relative abundance in the film, but because of texturing and possible strain, absolute quantitative analysis of the fraction of each phase present is arbitrary.

There has been computational work reported to explain the favorability of the hexagonal $YFeO_3$ phase to be energetically favorable.[81] If the ionic sizes of Y, Fe and O are considered, then this crystal phase provides the least frustration for perovskite like structures. It has been reported that even with yttrium deficiency, as is the case here, the hexagonal $YFeO_3$ phase can form.[75] Even if we are not forming the precisely defined $YFeO_3$ phase, there is reason to suspect we have a similar hexagonal phase. A $Y_2Fe_4O_9$ phase was previously reported to account for the nanocrystalline matrix.[33] While the fit was close for most peak locations, there was not an exact match. The commonality between the hexagonal phases is the location of the (110) peak which has high agreement with our results. This is also the direction of texturing based on the tilt study. The

placement and coordination of the iron ions determines the lattice constant in the c direction. This has had a range of values as reported.

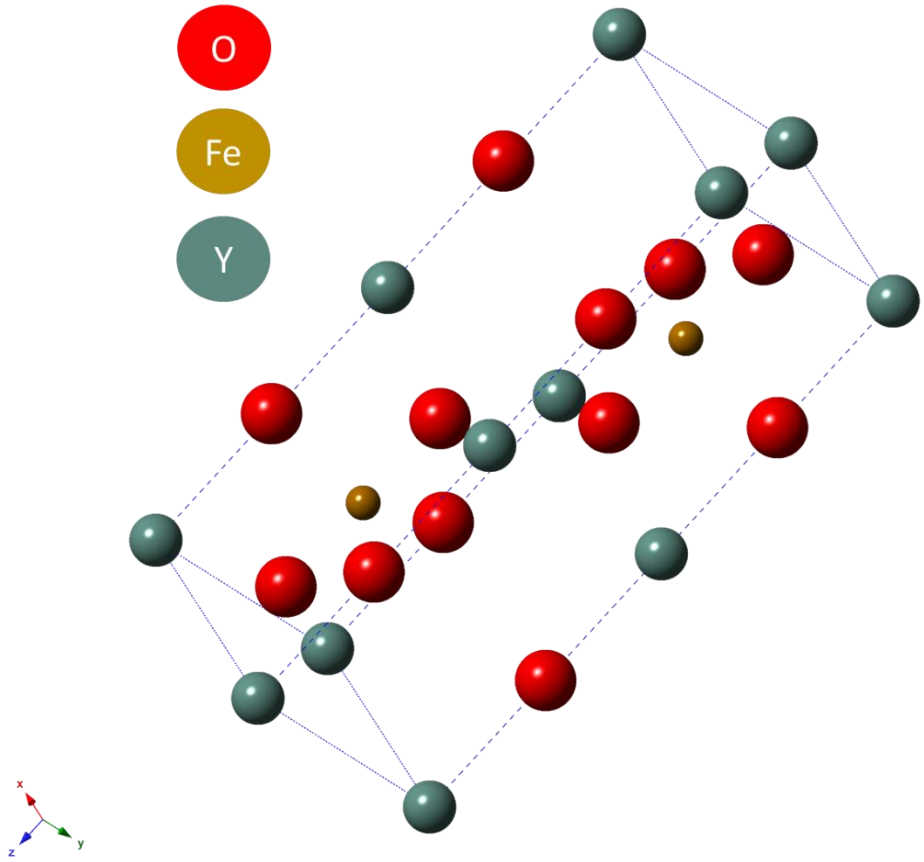

Figure 3.11. Simulated unit cell of the hexagonal-$YFeO_3$ phase. The Fe ions sit in a trigonal bipyramidal oxygen site. Created using CrystalMaker™.

3.3.2.3 CBED

Converged beam electron diffraction was used to obtain diffraction information about a single grain of the nanocrystalline phase. By using CBED, it is possible to ascertain symmetry information which is averaged out by having many grains in a PBED pattern.

Figure 3.12(a) shows a representative CBED pattern from a nanocrystal compared to a simulated pattern from a $YFeO_3$ hexagonal phase down the (001) zone axis. There is high agreement both in the symmetry and radii of the 2 prominent rings of CBED spots.

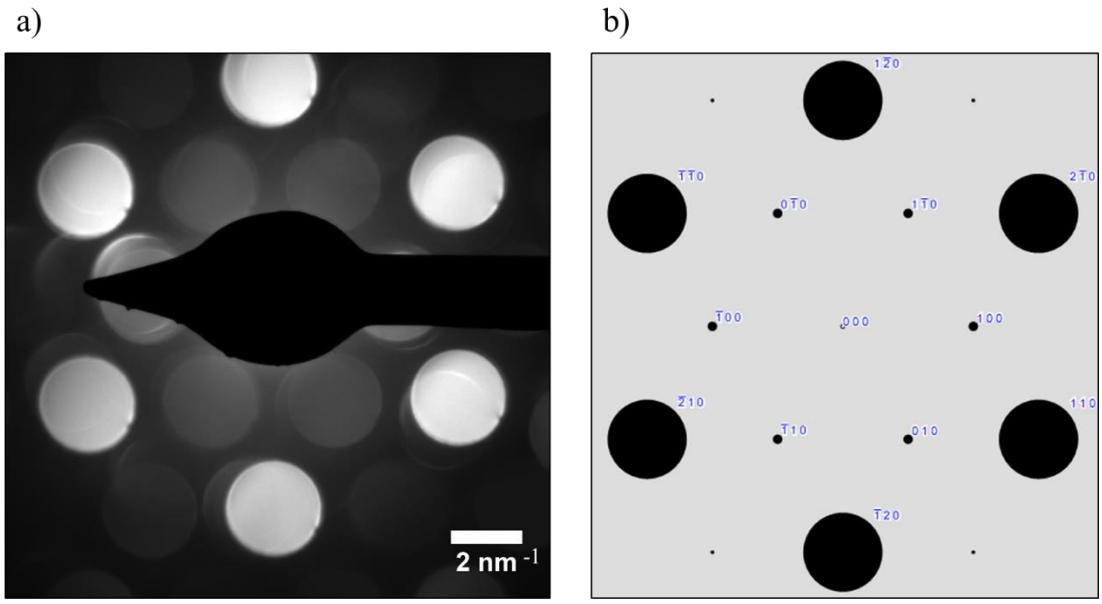

Figure 3.12 (a) CBED pattern obtained from imaging a highly textured nanocrystalline film with a 5 nm electron beam size at crossover. (b) Simulated diffraction pattern from the hex-$YFeO_3$ phase with weighted Bragg spots down the (001) zone axis.

3.3.3 Summary

Here we have been able to identify the presence of a nanocrystalline phase between large YIG crystallites in thin films of stoichiometric YIG after annealing. The presence of this phase is important because of its role during the crystallization process as well as possible properties that could impact average film behavior. While further studies are

needed to determine the structure of the nanocrystalline phase throughout the thickness of the film, the phase has shown to be strongly textured in some experiments and not textured in others. Further studies are also needed to confirm the exact crystalline phase present and if the hexagonal $YFeO_3$ phase forms in conjunction with a Fe_2O_3 phase. High resolution EDS imaging could provide insight as to whether phase or elemental segregation is occurring.

4. Chapter 4 – Two-Step Anneal of YIG Films

Initial *in situ* laser annealing studies were used to examine the amorphous to crystalline phase transition for YIG. From these studies, qualitative findings were used to try a new method of annealing in which a low temperature anneal was followed by a high temperature anneal. This resulted in higher crystallization of the YIG phase compared to the traditional single step anneal.

4.1 Preliminary In situ Laser Annealing

In order to study the amorphous-to-crystalline phase transition for YIG, *in situ* TEM laser-annealing studies were conducted on films deposited onto SiO_2 on Si as used in the previous chapter. The film used in this laser annealing section was 25nm. A relatively high average laser power (82.6mW; 1 second; Gaussian shape; 343nm) was used for *in situ* crystallization of the amorphous film. All laser power measurements were acquired near the source and should be referred to as relative and not absolute powers at the specimen. Further irradiation with this power produced no additional changes in the structure. Three regions with different crystallization behavior were identified, the formation of which is attributed to differences in temperature caused by the Gaussian energy profile of the laser similar to other *in situ* laser annealing studies, Figure 4.1.[82] The central dark region (red) was a nanocrystalline phase and was highly textured in-plane radially from the center of

the spot due to the direction of thermal transport. The texturing of this phase in a radial direction from the center of the laser spot can be seen in Figure 4.2. The second region (yellow) is shown more closely in Figure 4.1(b,c). The large grains in this region show bend contours due to the highly ordered crystalline structure, similar to the YIG crystallites in the RTA-annealed sample above. This region was pure YIG, as verified with SADP (inset of Figure 4.1(c)). The third region (blue), along the outer regions of the laser spot, was comprised of YIG crystallites that appeared to have seeded the growth in the second region. Using the known full-width at half-maximum (FWHM) of the laser intensity, and assuming the second region reached the crystallization temperature of YIG (800 °C), the third region was estimated to have reached 400 °C as shown in Figure 4.3.

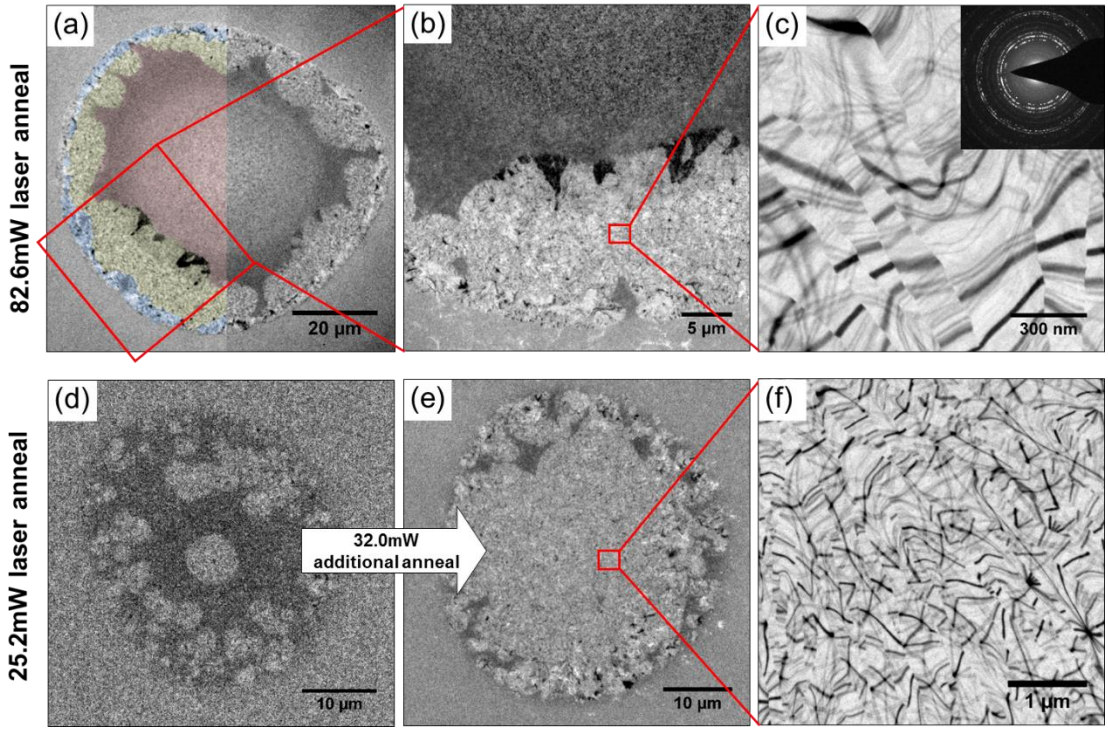

Figure 4.1. Bright-field images of YIG films crystallized with different laser powers. (a-c) Crystallization of YIG resulting from 82.6mW average power, shown with relatively (a) low (b) medium and (c) high magnification. YIG nanocrystals near the edge of the spot appeared to seed larger crystals inside a ring. The inset in (c) shows a SADP of the highly crystalline YIG area (d) Bright-field image of YIG film crystallized with 25.2mW average power followed by (e) an additional 32.0mW average power. The initial laser anneal at 25.2mW appeared to create crystallites that seeded subsequent growth. (f) Magnified image of the film following the second additional anneal at 32mW.

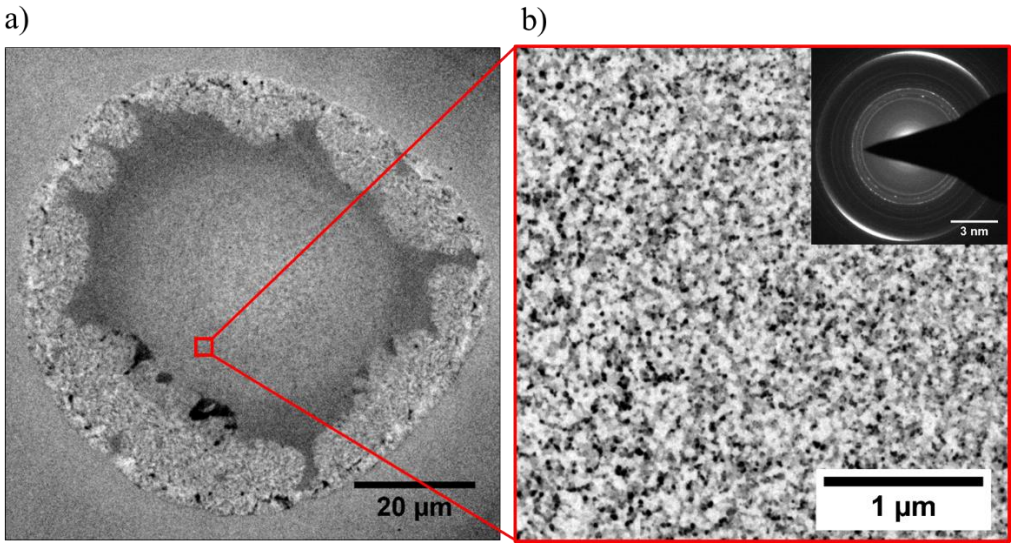

Figure 4.2. (a) Bright-field TEM image of the high power anneal laser spot (b) higher magnification showing the nanocrystalline nature of this region. The diffraction inset shows a strong texturing in-plane radially from the center of the laser spot.

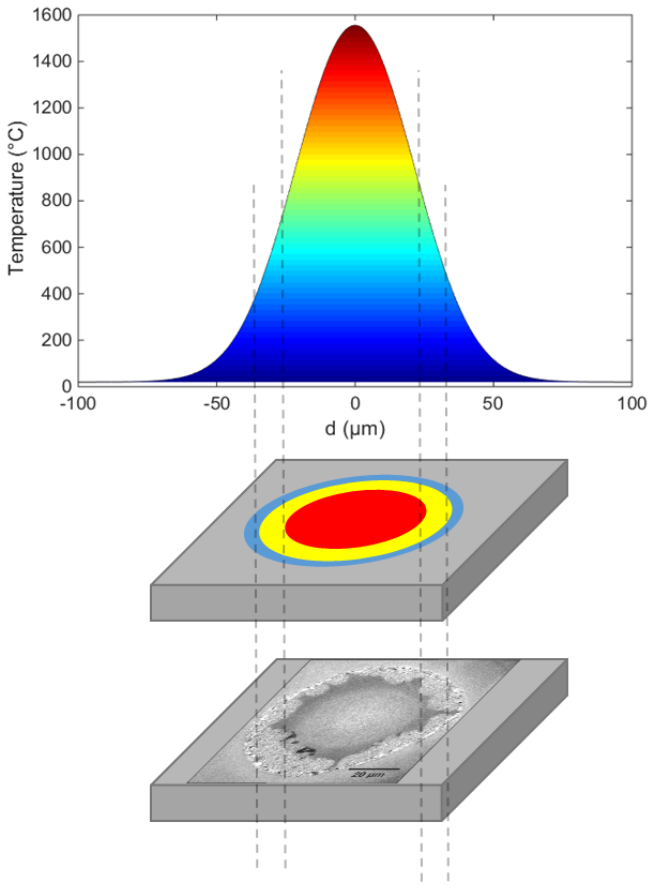

Figure 4.3. The temperature profile of the sample versus the distance from the center after laser irradiation. Three regions as defined in the sample are shown to correspond to the temperatures chosen for the two-step RTA experiment.

This growth behavior was unexpected, and it suggested that a low temperature anneal could produce nuclei and/or seed crystallites, thereby enabling the rapid formation of YIG during subsequent high temperature anneals. This low thermal budget concept for obtaining fully crystallized films is very appealing for eventual use in high quality spintronics and photonics devices.

To study this idea further, a lower average power of 25.2mW was used to form crystallites in as-deposited films, Figure 3(d). Further laser irradiation at this power did not produce any additional structural changes. However, increasing the average laser power to 32.0mW caused these crystallites to grow with a crystallization front velocity of 280 nm/sec, determined using time-resolved TEM. Figure 4.4 shows this growth. Although the laser profile again yielded different behavior for the outer region of the beam, the entire center of the laser-annealed area was phase-pure YIG after this two-step anneal, Figure 4.1(e,f).

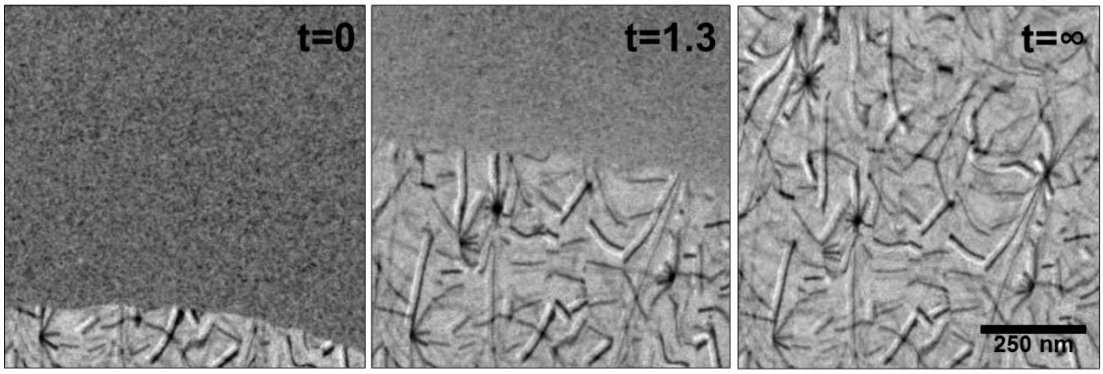

Figure 4.4. Still images taken from a video-rate movie of the YIG crystal front growing into the nanocrystalline phase. The front velocity was calculated to be 280 nm/sec.

4.2 Novel Two-step Rapid Thermal Annealing

This study was brought full circle by applying the newly discovered means of nucleation and growth to a two-step rapid thermal anneal, which can be up-scaled for use

with spintronics and photonics devices. YIG films (25nm and 130nm thick) were annealed by either standard RTA (800 °C, 3 min), low-temperature RTA (400 °C, 3 min), or two-step RTA (400 °C, 3 min; 800 °C, 3 min) all in a N_2 environment with a 10 sccm flow-rate during anneal. The first RTA process has been the most common anneal for YIG since its discovery.[83-90]

Magnetic hysteresis measurements (Figure 4.5) were used to determine the extent of crystallization for YIG films that were annealed using both the standard RTA and the two-step RTA. The films produced by standard RTA had saturation magnetizations of 99.6 emu/cc, which is 27% lower than expected for pure YIG. Significantly, the YIG films annealed by the new two-step RTA had saturation magnetizations of 130.6 emu/cc, which is within experimental error (eg: film volume measurements) of reported values for bulk YIG of 136.7 emu/cc.[24] These results are in fair agreement with the difference in the garnet area in a fully garnet film versus garnet areas found in the bright-field images shown in Figure 3.1.

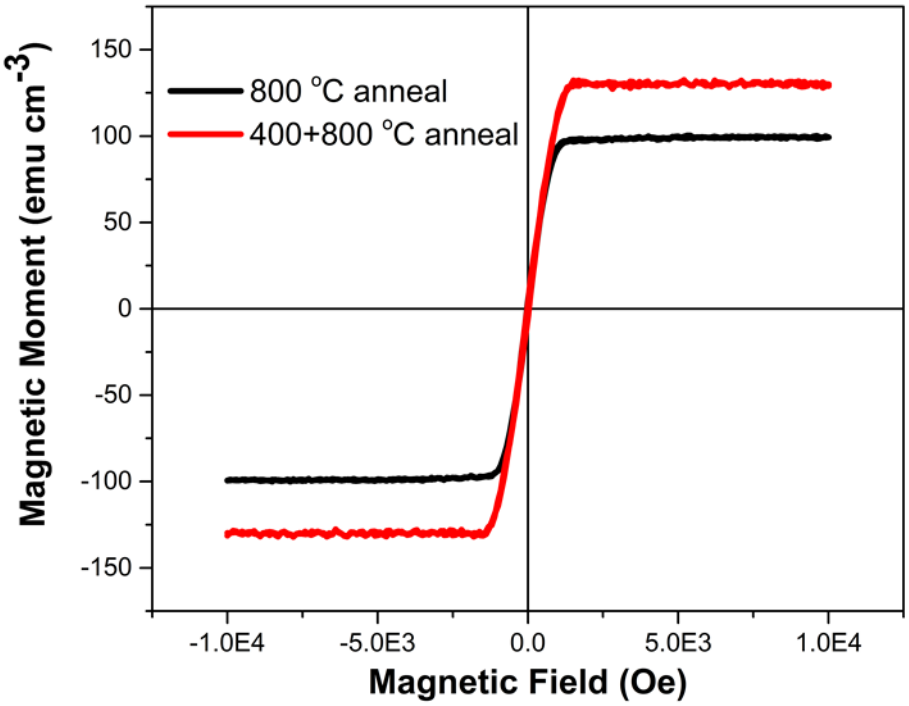

Figure 4.5. Out-of-plane hysteresis loops of 130nm thick YIG films annealed using standard RTA (800 °C, 3 min) and the new two-step RTA (400 °C, 3 min; 800 °C, 3 min).

Additional TEM characterization supported the VSM result that the novel two-step RTA produced completely crystallized (phase-pure) YIG films, Figure 4.6(a), rather than the typical crystallites in a nanocrystalline matrix, which are produced by standard RTA, Figure 4.6(b). The film annealed at only the pre-anneal temperature (400 °C) did not show any contrast in TEM imaging, appearing completely amorphous. The diffraction patterns in Figure 4.6(c) underscore the challenges associated with determining the phase purity of YIG films from diffraction alone. Both patterns, corresponding to images on the left, have similar peak intensities and highly consistent peak locations. These patterns strongly

suggest that standard, large-area Bragg diffraction patterns (X-ray diffraction) are not sufficient for reporting YIG crystallization of integrated devices because amorphous and "X-ray amorphous" (nanocrystalline) phases will not appear in these patterns.

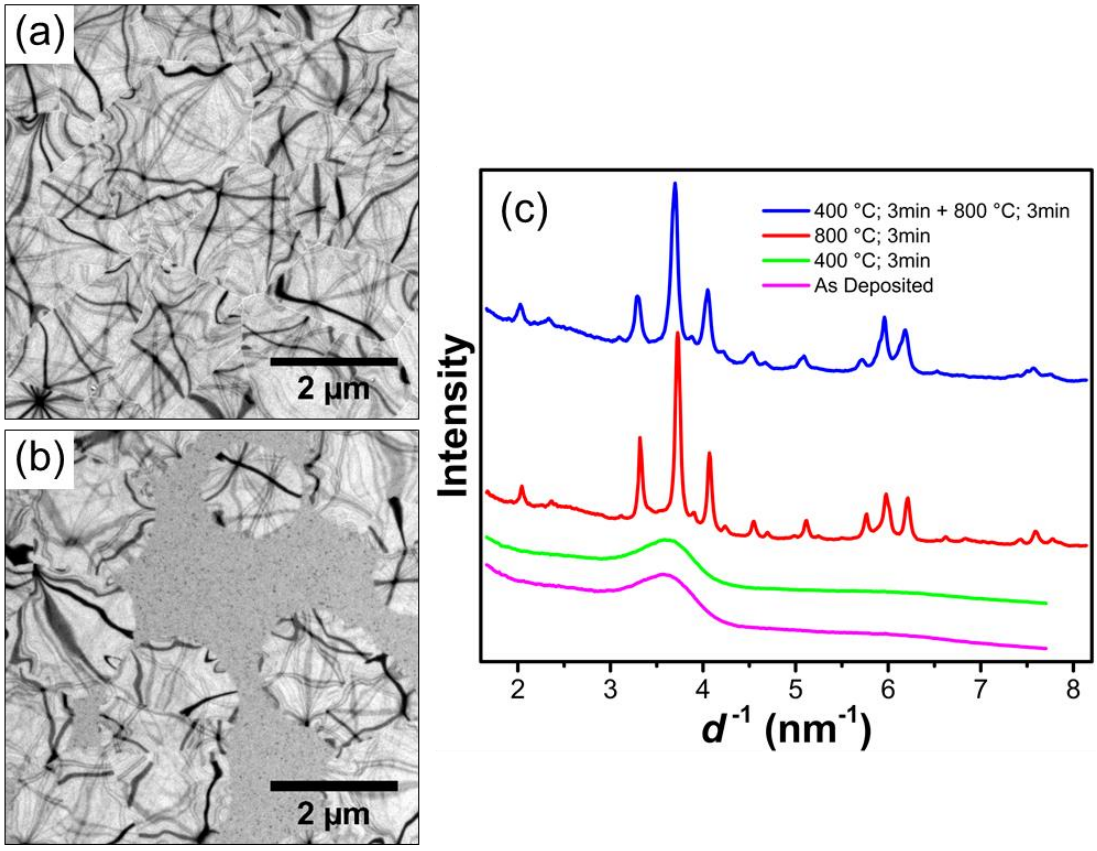

Figure 4.6. Bright-field TEM images of 25 nm YIG films (a) annealed at 400 °C for 3 min and subsequently annealed at 800 °C for 3 min and (b) annealed at only 800 °C 3 min. (c) Radial integration of diffraction patterns for films annealed at various conditions. The diffraction patterns appear similar, but unlike standard anneals, the two-step anneal successfully produced phase-pure YIG.

4.3 Conclusions and Outlook

The exact nature of the effect of a pre-anneal on the YIG film has not been determined by this study, though is of critical importance to better understand the crystallization process. Something changed in the YIG film when heated to 400 °C and cooled which allowed for complete formation of the YIG film compared to the film as deposited which is not detectable in diffraction or TEM imaging. One possibility is the relaxation of strain in the film. In chapter 5, the role of strain in YIG crystallite formation is discussed in further detail. If heating the amorphous film and cooling relaxes strain in the subsequent high temperature anneal, this could explain the complete crystallization observed. Another possibility is the ordering of the glass, specifically with regard to the iron ion coordination. Previous work in the field has indicated that films grown on a heated substrate have a higher number of iron ions in the 3^+ valence state which are able to crystallize into YIG films of higher quality.[91] It is possible that we are able to better chemically structure the YIG while it is still in its amorphous state. This theory of priming the glassy film for crystallization is supported by more general crystallization studies as well.[92] It could be that the growth is not promoted in the YIG film, but rather the number of nucleation sites. If the grains are growth limited to certain size, having more nucleation sites would allow for complete YIG transformation in the film. This transformation is studied more closely in Chapter 5, however the question of what caused the improved YIG formation remains unanswered.

5.Chapter 5 – *In situ* Laser Annealing of YIG Films

In this chapter, I will discuss the *in situ* laser annealing experiments I performed on thin films of amorphous YIG. These experiments have given us insight into the crystallization dynamics of these films that was not available through *ex situ* annealing studies. The *in situ* laser annealing experimental setup is not completely novel, though I have found no other publication reporting temperatures, activation energy or Avrami coefficients from such an experimental setup. These important crystallization parameters and how they were calculated using this experimental method are described here.

5.1 Laser heating advantages

Laser annealing is not the only method for *in situ* TEM annealing experiments. More popular is using an *in situ* heating holder which uses a resistive heating furnace to heat the entire specimen. The use of an *in situ* heating holder offers some advantages and disadvantages to *in situ* laser heating. Advantages include being able to directly measure the temperature of the specimen and select this temperature with an external controller. Also, the ability to uniformly heat a specimen can in some experiments be an important advantage as well.

In contrast, *in situ* laser annealing can heat only small portions of a specimen in an isolated fashion. In this way, experiments can be conducted at different temperatures on

the same specimen. This offers more certainty of specimen uniformity between temperature experiments as shown in this study.

Also important to *in situ* heating studies is the ability to reach temperatures of interest quickly for isothermal assumptions in analysis. Demonstrated here are temporal temperature gradients greater than 100 °C/ms. In other *in situ* crystallization studies, *in situ* heating holders are limited to increases of 10 °C/min.[93-95] This is more than 7 orders of magnitude difference between temperature rise rates for laser annealing versus a typical heating holder. Even new holders from Protochip, which have electronics built into the TEM grid for heating, only allow for heating at rates of 1000 °C/s, orders of magnitude slower than the laser heating method.[96]

The maximum temperature for modern TEM heating holders is between 800-1400 °C. While these are high enough temperatures for many different types of experiments, the intrinsic instrument limitation is not shared by the laser heating method. Using laser heating, the maximum temperature of the experiment is dictated only by the limits of the laser used and the material properties of the specimen.

Lastly, specimen drift is a significant issue with high temperature experiments using heating holders.[97] This is a side effect of heating many components in the specimen holder as well as the entire specimen, all of which are affected by thermal expansion. Laser heating does not have this issue because the localized heating only impacts relatively small volume of material.

Though not a specific experimental advantage of laser heating compared to heating holders, laser annealing is becoming a more popular annealing method in industry and performing experiments more closely resembling the applied practice is highly appealing to materials engineers. The higher temperature gradients and Gaussian temperature profiles shown here would be important factors to industry for laser annealing and could potentially be investigated further using this experimental setup.

5.2 Laser heating model

In order to understand the laser heating process better in our TEM setup, a finite-difference model was developed to predict the spatial and temporal behavior of the temperature profile in the YIG film during pulsed laser irradiation. The model was as simplified as possible for computational considerations. A one dimensional model is applied due to the radial symmetry of the system and the high aspect ratio of the film's area to its thickness.

Before the model evolves in time, the effect of a single laser pulse must be applied to the film. The relevant material properties are input for both the film and the substrate found in literature and are summarized in Table 5.1. The laser pulse energy can be measured experimentally and the pulse duration is assumed to be instantaneous compared to other relevant time scales in the model. The fraction of the laser energy absorbed is calculated using

$$f_{energy} = (1 - R)(1 - e^{-A_{film}t_{film}})(1 - e^{-A_{sub}t_{sub}})$$

where *R* is the fraction of the laser reflected from the surface and *A* and *t* are the absorption coefficient and thickness respectively for the film and the substrate as designated by the subscript. The average change in temperature for the laser spot is then calculated by assuming a thickness weighted average of the density and specific heat of the film-substrate system. This temperature change is an average change over the FWHM of the laser spot which is then converted into the assumed Gaussian spatial profile. The temperature is then allowed to evolve in time based on classical heat transfer equations.

	YIG film	*SiO_2 membrane*
Thermal conductivity, k *(W/m-K)*	0.74 [98]	0.8 [99]
Specific heat, C (J/kg-K)	426 [98]	719 [100]
Density, ρ (kg/m^3)	5170 [101]	2220 [102]
Thickness, t (nm)	25	40
Extinction coefficient, A (1/m)	2x10^6	~ 0

Table 5.1 Relevant physical properties for YIG and SiO_2 used in the laser heating model

The governing equation is the following as described in Chapter 2

$$\frac{\partial T_j}{\partial t} = \alpha \frac{\left(j+\frac{1}{2}\right)\left(T_{j+1}-T_j\right)-\left(j-\frac{1}{2}\right)\left(T_j-T_{j-1}\right)}{j*\Delta r^2}$$

Where T_j is the temperature at spatial step j starting at the center of the Gaussian, Δr is the radial step spacing. The thermal diffusivity, α, is taken found using the following formula.

$$\alpha = \left(\left(t_{film}\right)\left(\frac{k_{film}}{C_{film}\rho_{film}}\right) + \left(t_{sub}\right)\left(\frac{k_{sub}}{C_{sub}\rho_{sub}}\right)\right)/\left(t_{film} + t_{sub}\right)$$

Variables here are described in Table 5.1. A Runge-Kutta method is used to solve the system implicitly, stepping forward in time. A Neumann boundary condition is assumed at j=0 representing the symmetry of the Gaussian profile. This is easily implemented by equating the j=-1 position to the j=1 position, effectively forcing the derivative at this point to be zero. At the outer radius of the model, the edge of the window membrane is a Dirichlet boundary condition. This forces the final spatial point to be a fixed temperature, set to room temperature here. The relatively infinite heat sink and high thermal conductivity of the crystalline silicon support make this a reasonable assumption. As seen in Figure 5.1(a), the heat from the system will travel along the negative gradient towards the edge of the window. The cooling of the film is allowed to evolve until the following laser pulse strikes the system.

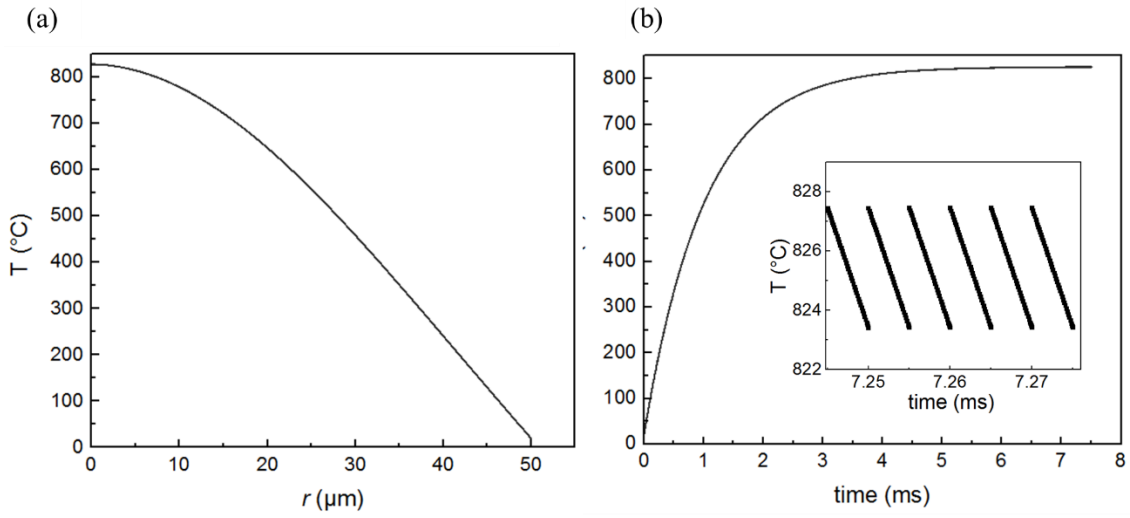

Figure 5.1. (a) Modeled temperature at steady state of the YIG film across a TEM window as a function of radius. (b) Temperature at the center of the laser spot as a function of time. The laser spot reaches a steady state after a few milliseconds. The inset shows that even at quasi-steady state, there is some time variation in the temperature (<5 °C). Laser repetition rate: 200 kHz, average power: 10 mW

Based on an input laser repetition rate, the process of adding the initial Gaussian temperature profile is iterated after a time of 1/frequency. The cycle repeats for a set number of pulses. Typically, for the YIG film system, on the order hundreds of pulses are needed to reach a pseudo-steady state as seen in Figure 5.1(b). Between pulses the temperature of the system relaxes. As seen in Figure 5.1(b), for the parameters described in Table 5.1, the temperature variation between pulses is less than 4 °C at a laser repetition rate of 200 kHz and average power of 10 mW. Even though this is a pulsed laser system, we can treat the temperature to be a quasi-steady state.

5.3 In situ Thermometry

The finite difference (FD) model is a good qualitative approximation for the behavior of the temporal and spatial profile of the heat flow in the film. However, it includes terms which are approximations of film properties or assumed from literature and are not measured. To fine tune the model, we experimentally verified the temperature of the film with an *in situ* thermometry technique utilizing the thermal expansion of the crystalline YIG lattice. Specifically, the location of the YIG diffraction (Bragg) spot is observed with the laser on and off, and the lattice temperature is estimated from the change in the location of this spot.

The YIG film is supported by an amorphous silicon dioxide membrane. The membrane will also expand due to heating but has a different coefficient of thermal expansion (CTE) compared to the YIG film. In order to account for the thermal expansion of the electron transparent window, a weighted average of the YIG film CTE and the SiO_2 support film was used:

$$\alpha_{eff} = \alpha_{YIG}\left(\frac{E_{YIG}t_{YIG}}{E_{YIG}t_{YIG}+E_{SiO2}t_{SiO2}}\right) + \alpha_{SiO2}\left(\frac{E_{SiO_2}t_{SiO_2}}{E_{YIG}t_{YIG}+E_{SiO_2}t_{SiO_2}}\right)$$

The CTE for each layer is weighted by the thickness and Young's modulus for that layer. The values for CTE for YIG and SiO_2 were taken from literature[102-103] as were those for the Young's moduli of both materials.[104-105] The temperature variation in the CTE for YIG was taken into account for this model while all other values were taken at 800 °C.

The Young's modulus used for YIG was that of polycrystalline YIG which more closely resembles the film structure here.

Using the equation which describes the CTE,

$$\Delta T = \frac{\Delta L}{L}\frac{1}{\alpha}$$

where L and ΔL are experimentally measured using diffraction patterns. When the laser is on the specimen, the material is heated and the lattice expands. This moves the diffraction spots closer to the center of the diffraction pattern in reciprocal space. We can measure d' and Δd' in reciprocal space and convert this back into the real space values for L and ΔL to find:

$$\Delta T = (1 - (1 - \frac{\Delta d'}{d'}))\frac{1}{\alpha}$$

Equivalent diffraction spots opposite the (000) spot corresponding to the YIG phase were fit to two dimensional Gaussian profiles and the distance between them for both laser on and off were recorded. In this way, d' and Δd' could be found for different laser powers. The YIG phase only formed in the highest three temperature experiments and the laser temperature was approximated based on a linear fit of the temperature versus laser power shown in Figure 5.2. These temperatures were used in the analysis in the following sections.

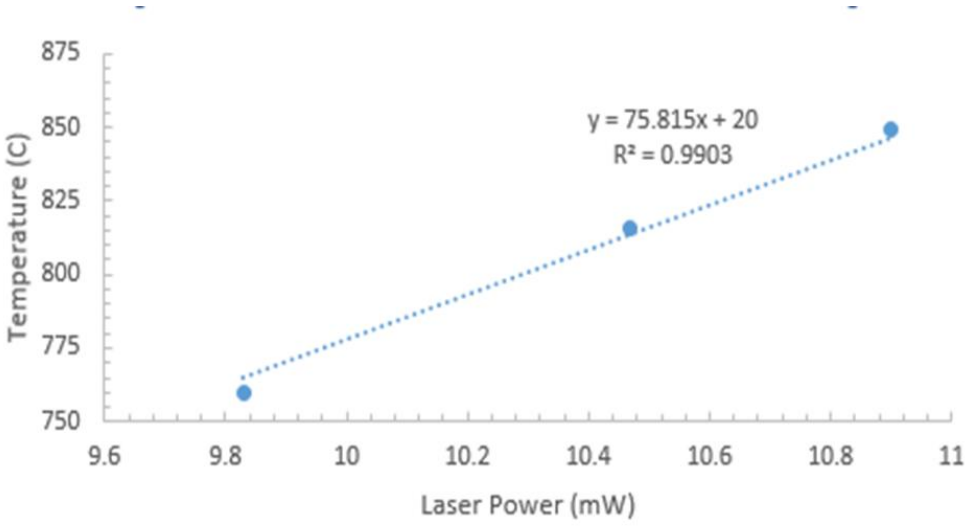

Figure 5.2. Plot of calculated film temperature as a function of incident laser average power. The linear fit equation on the plot was forced to have an intercept at 20 °C and was used to find the temperature of the lowest temperature window.

5.4 Diffraction

When the laser heats the amorphous YIG films above a certain temperature the films will crystallize. This crystallization process can be observed in reciprocal space by monitoring the diffraction pattern. The diffraction pattern begins as a radial distribution function with diffuse rings at radii of the average interatomic spacing of the various atoms. As the film is crystallized, these diffuse rings give way to well-defined rings related to the transient crystal structure. The evolution of this transition aids in our understanding of the solid state crystallization process.

5.4.1 Experimental

All experiments in this chapter were performed on the same windowed TEM grid. This grid was the same as those described in previous chapters. The YIG film was 25 nm thick as measured by AFM. After precise alignment of the probe laser as described in Chapter 2, the first window was used as a calibration for finding an appropriate laser power. The laser was set to 200 kHz with a wavelength of 515 nm. The average power was slowly increased with the laser incident on the window until crystallization was first observed at 9.36 mW. Using this same average power, a new window was positioned such that it was centered with the laser and the field of view. A selected area aperture with an effective diameter of 5.4 μm at the object plane was inserted. The microscope was then put into diffraction mode and aligned. Using "*in situ"* mode on the Gatan Oneview camera, the camera was set to be binned by 2 and a frame rate of 50 frames/sec. The "look back" feature was set to 3 seconds, and the laser was set to the desired power of 9.36 mW at a repetition rate of 200 kHz. The laser shutter and the camera acquire buttons were pushed simultaneously. There were 3 seconds of recording before time zero due to the "look back" feature. The change in diffraction pattern was observed and recorded. The recording was terminated when there was no change in the diffraction pattern for at least one minute. This process was repeated for laser powers of 9.83, 10.47, and 10.9 mW sequentially. For the 10.9 mW recording, the camera was binned by four to allow for a higher frame rate of 200 frames/sec, 5 ms exposure time.

5.4.2 Data Analysis

Each frame of the diffraction videos was radially integrated to obtain intensity information for a given scattering vector. A custom MATLAB program was written for this function. This program was able to report average intensity at a given pixel radius for areas of the image bounded by user assigned angles. Due to the large number of images (>10,000), considerable effort was put into making sure this process was as computationally economical as possible. Figure 5.3(a) is representative of a diffraction image frame and the yellow outline shows the integrated area. Once each frame was analyzed, a typical integrated diffraction pattern was rendered similar to that shown in Figure 5.3(b). This pattern is of the nanocrystalline $YFeO_3$ phase which appeared first. The (110) peak was fit to a Gaussian after a simple background subtraction as shown in Figure 5.3(c). The evolution of this peak was correlated with the growth of the nanocrystalline phase in the following analysis. The fitting parameter for the intensity of the Gaussian fit was multiplied by the variance parameter fit. This product gave a value proportional to the area under the peak. This value was assumed to be proportional to the number of electrons scattered due to the $YFeO_3$ phase and taken as a representation of the phase's presence.

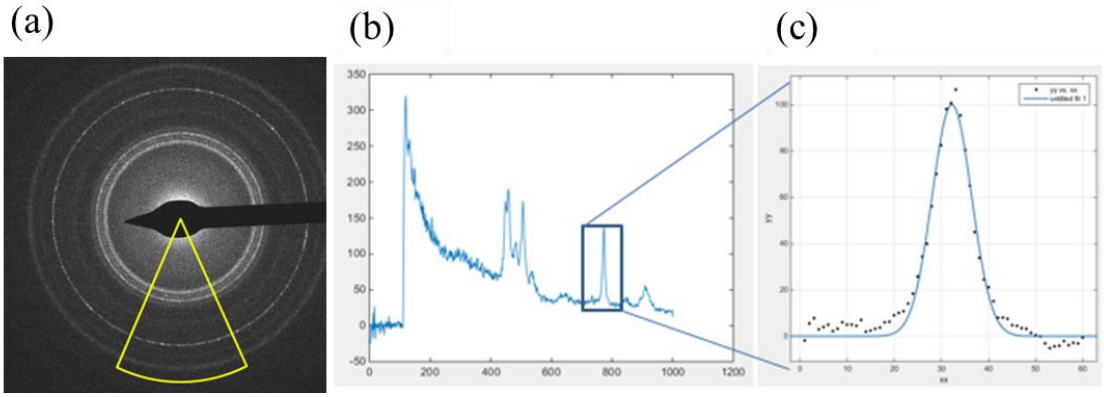

Figure 5.3. (a) Representative diffraction pattern of the nanocrystalline phase used for analysis. The yellow wedge indicates the region being used for integration. Screenshots of MATLAB code (b) Average azimuthally integrated intensity versus pixel data (c) Gaussian fit to the (110) peak of the nanocrystalline phase after background correction.

5.4.3 Results

The previously described microstructure of the YIG films on SiO_2 is seen in these experiments as well. The nanocrystalline phase is represented by rings of uniform azimuthal intensity while the YIG grains give rise to spots in the diffraction pattern. There is a typical pattern which can be seen qualitatively in the evolution of all the diffraction pattern movies shown in Figure 5.4. The diffuse amorphous pattern is present before time zero in all videos and, at some point after time zero, the $YFeO_3$ nanocrystalline phase begins to appear. This is followed by the Fe_2O_3 nanocrystalline peaks and in some videos, the YIG spots are formed last.

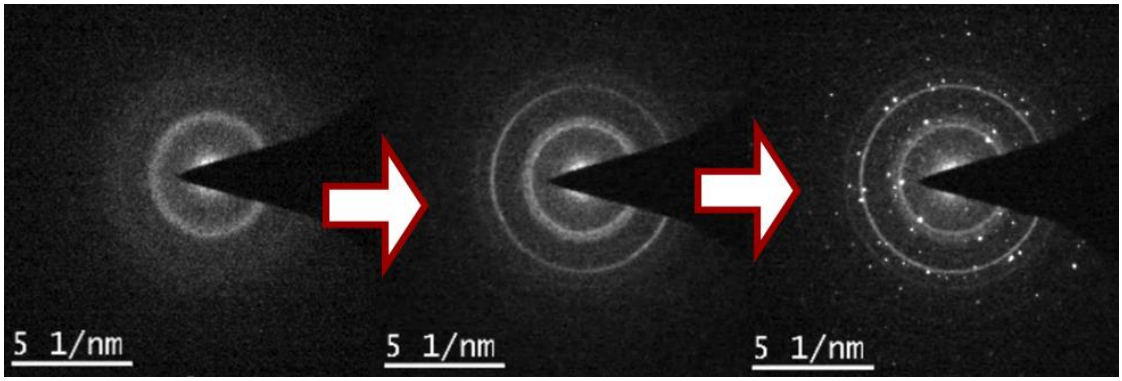

Figure 5.4. PBED patterns showing the typical evolution of the YIG film. It begins as an amorphous pattern, forms a nanocrystalline phase causing rings with smooth azimuthal intensity. The YIG phase appears last as spots due to the large single-crystal crystallites.

The amorphous to nanocrystalline transformation is also shown in Figure 5.5 for all four temperatures used in the experiments. In this figure, the diffraction peaks are labeled for the different phases which appear during the evolution of the crystallization. In the two highest temperature experiments, it is interesting to note that the nanocrystalline peaks all diminish as the YIG peaks form, nearly disappearing at 849 °C. This reinforces the conclusion that the YIG phase is growing into the nanocrystalline phase and not into still uncrystallized amorphous material. The evolution of the Fe_2O_3 peaks were not quantitatively analyzed in this work, however, they do appear to have a longer time scale associated with their arrival compared to the $YFeO_3$ phase. This could be due to diffusion limitations or a higher energy of formation for the Fe_2O_3 phase. The Fe_2O_3 phase does not appear to be consumed by the YIG phase and is present in final diffraction patterns where

no $YFeO_3$ phase is present. This indicates a higher degree of stability for this phase and indicates it is possibly precipitated at interfaces.

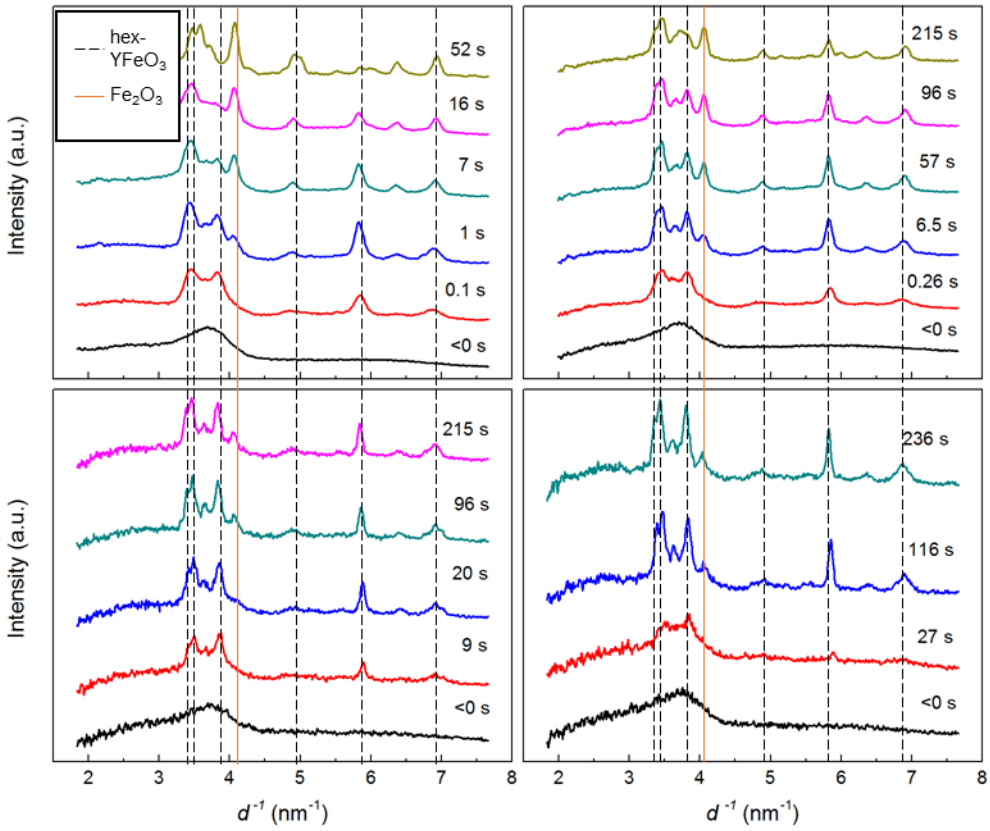

Figure 5.5. Radially integrated diffraction pattern data for all four temperature experiments. All temperatures show similar evolution moving from an amorphous state to a crystalline state. Times of various patterns are noted on the plot.

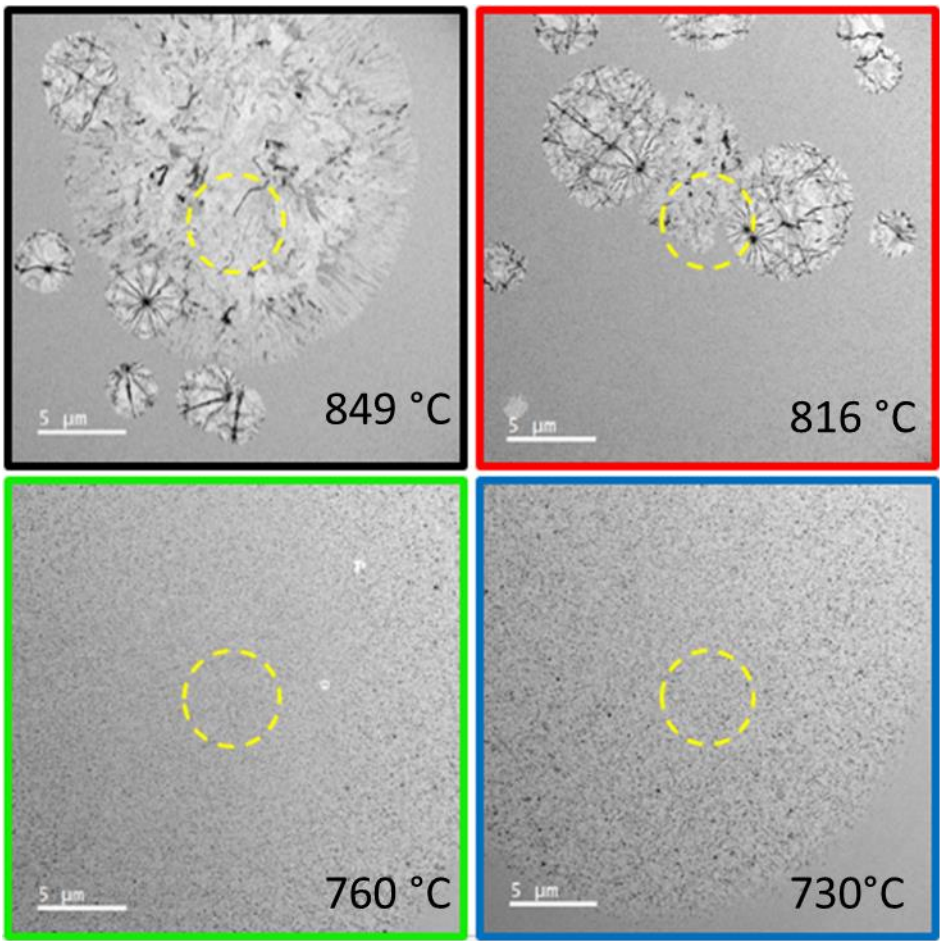

Figure 5.6. Post-mortem bright-field images for all four temperature experiments. The dashed circle indicates the location of the selected-area aperture used during the time-resolved diffraction experiments.

Figure 5.6 shows post-mortem bright-field images of the windows from the four different temperature experiments as well as the placement of the selected area aperture used during the time-resolved diffraction experiments. The highest temperature window shows the YIG phase with strong in-plane texturing at the temperature region where the

diffraction experiment was performed. This could indicate explosive growth of the YIG phase. The next highest temperature is similar to the results of the *ex situ* annealing studies. There are large round YIG crystallites in a nanocrystalline matrix. The crystallites vary in size depending on their radius from the center of the laser spot. In the third highest temperature window, only two small YIG crystallites are observed outside of where the selected area aperture was placed and in the final window, no YIG formed during the entirety of the experiment. These results demonstrate the role that temperature has on the final YIG microstructure. For more applications of the YIG phase, large, single-crystal grains are desirable, similar to those found in the 816 °C window. This temperature is examined further in the bright-field experiment below.

By assuming that we start with no $YFeO_3$ phase formed and at some point in time have 100% of our film in the selected area transformed into this phase, we can use classic crystallization quantification techniques to analyze the phase's evolution. In Figure 5.7, we show the calculated fraction crystallized of the amorphous phase based on the analysis of the area under the (110) peak for the $YFeO_3$ phase. For each temperature, we see the expected logic function curve. Each curve levels out as the entire film is converted to the $YFeO_3$ phase.

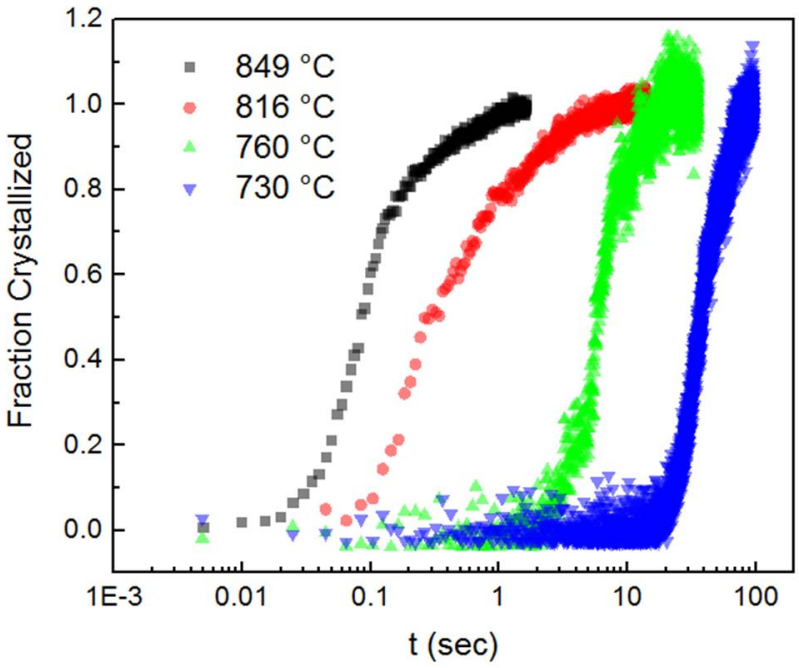

Figure 5.7. Fraction of the film transformed to the nanocrystalline phase versus time. The fraction crystallized was calculated from the product of the intensity and width of the (110) peak Gaussian fit.

The JMAK crystallization equation previously derived in Chapter 1, is used to compare the crystallization dynamics at each temperature. For this analysis, the time has been converted to hours.

$$\ln(-\ln(1-\alpha)) = \mathrm{n}\ln t + \ln K$$

The fraction crystallized is represented by α and the time by *t*. The Avrami coefficient, *n*, is determined by the kinetics of the crystallization process. This equation is plotted for the four temperatures analyzed in Figure 5.8.

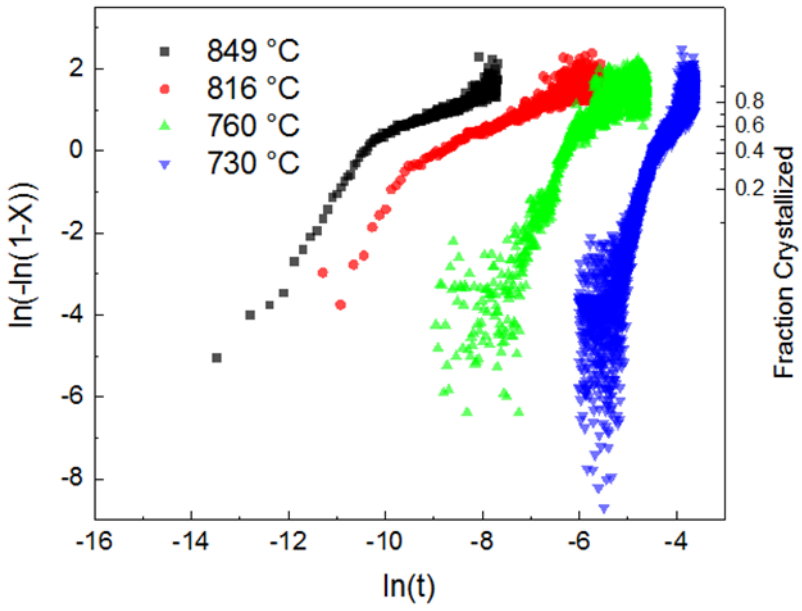

Figure 5.8. Plot of crystallization data using the JMAK linear analysis. Linear regimes are seen in the initial crystallization behavior for all temperatures.

Here, it can be seen that there are linear regimes initially in all crystallization temperatures which give way to a second linear regime after some time and near 50% crystallization. Data before crystallization has been removed for clarity. The initial crystallization behavior follows a pattern where the Avrami coefficient, *n*, has an inverse relationship to the temperature. This is shown in Table 5.2 along with the values of *ln(K)* for the Avrami fit.

Temp. (°C)	*n*	*ln(K)*	R^2
849	2.02	21.18	.9917
816	2.13	19.94	.9811
760	2.75	17.19	.8540
730	3.44	15.20	.9296

Table 5.2. Results of linear fitting to the initial crystallization dynamics for each temperature experiment.

5.4.4 Discussion

Such a large change in n is somewhat unusual for this small of a temperature range. There is also a large change in incubation time before crystallization . If we assume homogenous and continuous nucleation, we would expect to have a value of n close to four if we have three dimensional isotropic growth.[106] Because of our crystallite size and the thickness of our film, this film system falls into a middle ground between three dimensional growth and constrained two dimensional growth. Nuclei near the film interfaces will not be able to grow beyond said interface. In the 25 nm YIG film, we expect to have growth behavior between three and constrained two dimensional growth,[107] which would have an Avrami coefficient of 3 and 4 respectively. At 730 °C we have an Avrami number within this range. As we increase our crystallization rate and decrease the incubation time with increasing temperature, the actual crystallization process behaves in a more limited way.

This could be due to diffusion limitations.[108] The nominal crystallization behavior is still faster for higher temperatures even though the Avrami coefficient is lower. The lower Avrami coefficient could mean that during the incubation period, there is diffusion occurring in the glassy system which subsequently facilitates easier crystallization. Another possibility, is that the nucleation behavior is much more dominant at higher temperatures, limiting the effect of growth and thereby skewing the Avrami model.

The reporting of the structure of the grains in the nanocrystalline phase where the analyzed dynamics were captured was only possible in the two lower temperature experiments. The film area in the two higher temperature experiments transitioned into the garnet phase by the end of the annealing process. A study where the nanocrystalline phase was only allowed to partially form and was investigated in real space would be illuminating to its nucleation and growth nature. Also, performing similar experiments at more temperatures would determine if there is some numerical fit between the Avrami number and the temperature, it is possible that we would see asymptotic behavior at the high and low ends of the temperature range.

5.5 Activation Energy

The apparent activation energy of the $YFeO_3$ phase for our system was determined by two different methods with high agreement. The first method was with analysis of the fraction crystallized at a given time and the second was by looking at the intercept of the Avrami fit. Both of these values should follow an Arrhenius behavior and have been

analyzed as such. Figure 5.9(a) shows the results of finding times it required for the different temperature experiments to reach a certain percentage of crystallization. The fit has an R^2 value of 0.9626. The slope of the fit is 5.064 eV with a standard error of 0.258 eV. Using the intercepts from the Avrami plot, we expect to see a linear relationship when plotted against inverse temperature. Here our slope is -4.786 eV and our standard error is 0.176 eV. If we average these approximations of activation energy, we have a value of 4.925 eV. This value is comparable to other reported crystallization activation energies for similar systems.[109]

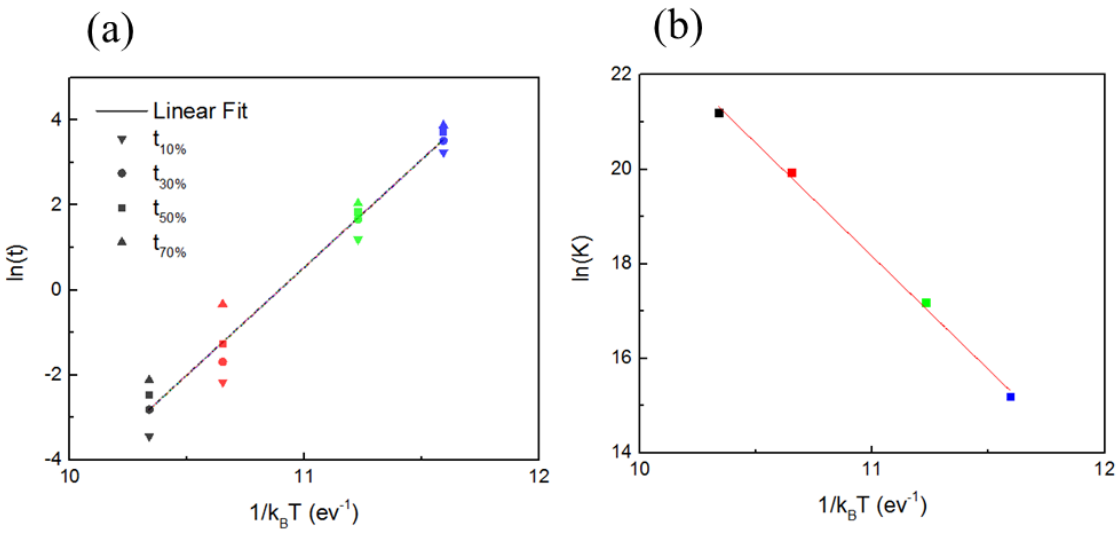

Figure 5.9. (a) Plot of the natural log of the time to reach a particular fraction crystallized versus the inverse of the thermal energy. The linear fit has the slope of the activation energy. (b) The intercept for the Avrami crystallization model fit versus the inverse of the thermal energy. The linear fit has the inverse slope of the activation energy.

5.5 In situ Bright-Field Imaging

Utilizing the same TEM window grid as in the diffraction study above, a different window was used for bright-field analysis of the YIG phase growth. Studying the garnet phase dynamics with an Avrami analysis is not practical in the TEM because of the large grain size relative to the field of view. There would not be enough grains to create rings with mostly uniform intensity, and any intensity analysis would be strongly skewed due to grain orientation. However, in bright-field mode, we can observe the growth of the YIG crystals in real-time and study the crystallization behavior in this way.

The same alignments were performed here as in the diffraction study. The laser power was set to 10.47 mW because the post-mortem observations from the diffraction study suggested this would be the most interesting temperature to observe for potentially high quality YIG grain formation. The TEM camera was set to 5 frames/sec and the images were not binned, utilizing all 4096 x 4096 pixels. The magnification was set to 1700x which is the lowest magnification which allows for proper bright-field imaging. This allowed for higher contrast from bend contours, the primary source of contrast in the film, as well as a high field of view to observe as many nucleation events as possible.

Figure 5.10 shows the stages of growth for the YIG film. There is a slight contrast change as the nanocrystalline phase forms in the first seconds of the video. The YIG crystallites begin to nucleate and subsequently grow into the nanocrystalline phase. The diameter of the crystallites was measured during growth until the crystallites coalesced. This measurement is shown in Figure 5.11.

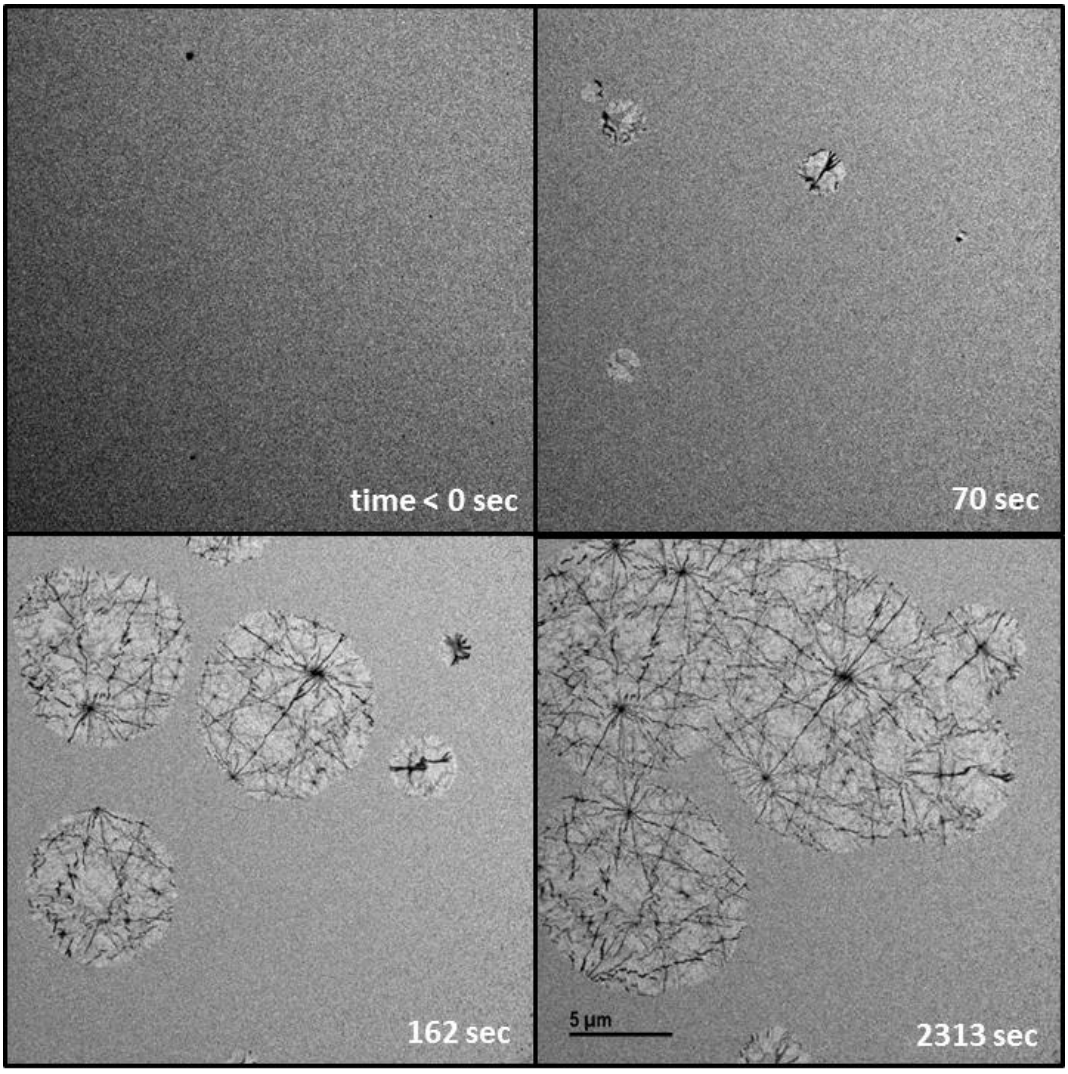

Figure 5.10. Still images from a bright-field movie obtained during the crystallization of the YIG film at 816 °C. The time of each frame is noted in the bottom right corner.

Unlike in the diffraction study, no selected area aperture is used here. This means we are sampling a larger variety of temperatures due to the Gaussian nature of the temperature profile discussed in the laser heating model section. As a result, the crystallites

at different temperatures have their own growth profile. All of the observable crystallites had qualitatively similar growth profiled in that their crystallization velocity slowed down with time. Though not shown here, all of the slopes go to zero by the end of the experiment, meaning that the crystallization process stops before all of the film is transformed.

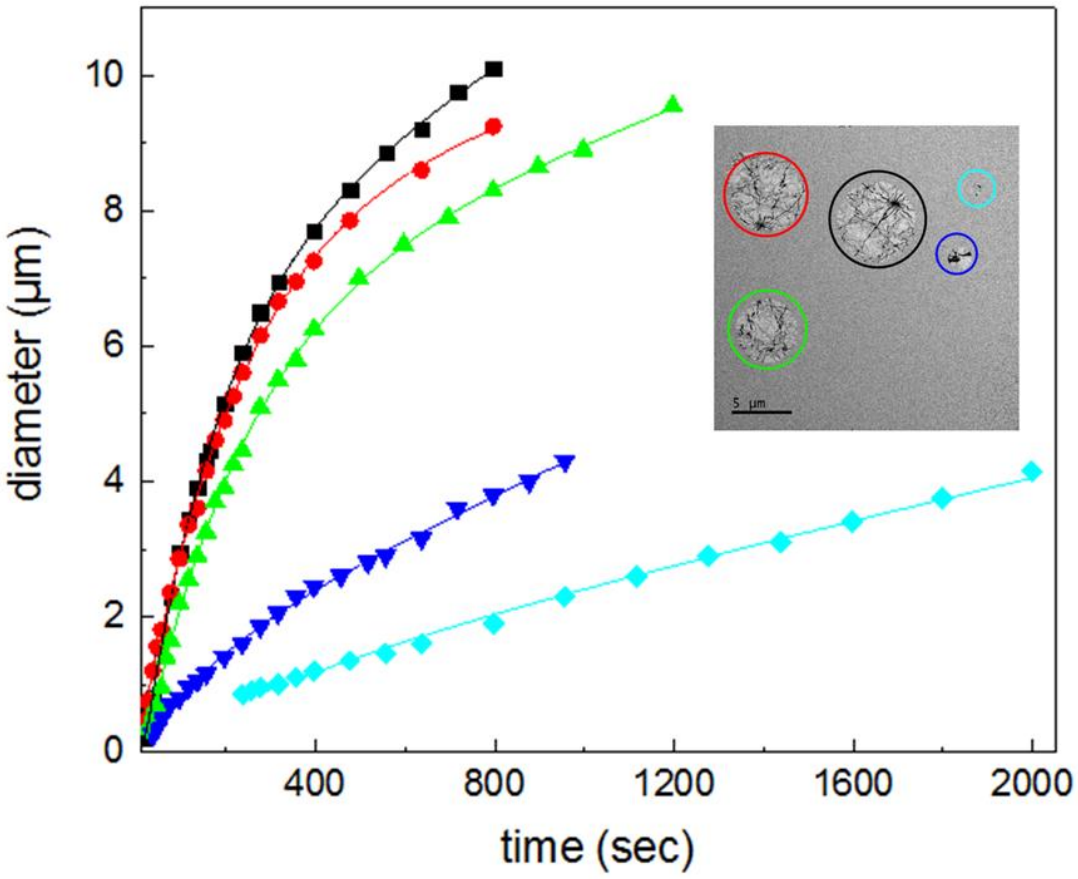

Figure 5.11. The diameter of various YIG crystallites versus time. The inset indicates which crystallite corresponds to which data set. The lines are fits to the stress limited crystal growth equation.

The diameter versus time data was fit to a stress limited crystallization model.[110] The model assumes that the crystallization is limited by both diffusion and stress and is described by the following equation.

$$L(t - t_{nuc}) = L_S(\frac{t-t_{nuc}}{\tau_R} + (1 - e^{-\frac{t-t_{nuc}}{\tau_D}}))$$

L is the diameter of the crystallite, L_s is the characteristic crystallite size when stress begins to dominate its growth behavior, t_{nuc} is the time of nucleation for that crystallite, τ_R is the stress relaxation time constant and τ_D is the diffusion time constant. The time scales for these two parameters dictate the growth behavior of the crystals. If the characteristic time scale for stress relaxation is much longer than that of diffusion, the crystallites will grow to a certain size and stop. Figure 5.12 shows the modeled relationship the two time constants can have on the crystallization velocity.

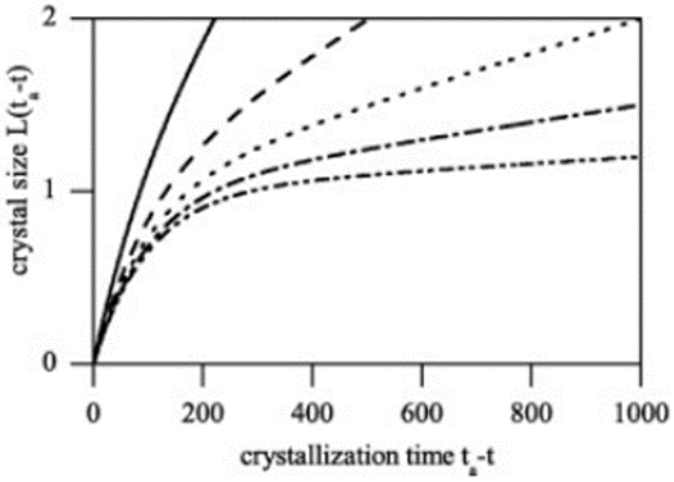

Figure 5.12. Time dependence of the diameter of crystallites based on the model. The different lines have various ratios of relaxation and diffusion times scales. A higher ratio leads to a slower end stage growth behavior. Adapted from Bocker et al.[110]

The computational fit to the model above has four fitting parameters making some of the margins of error large. By estimating the center of the laser spot on the window shown in Figure 5.13(d) and the distances from the center, temperatures can be assigned to each crystallite. Figure 5.13(a-c) shows the trend of each fitting parameter, except for the nucleation time, for each crystallite as a function of temperature. There are general trends in the fit which are logical. For example, L_s increases with temperature as we observe in the real space video. However, it is counter-intuitive that the relaxation time constant increases with temperature except that grains with higher temperatures tend to have a higher initial crystallization velocities due to thermodynamic driving forces. This could skew the thermal relaxation constant higher for higher temperatures. The general decrease in diffusion time with an increase in temperature agrees with faster migration of ions.

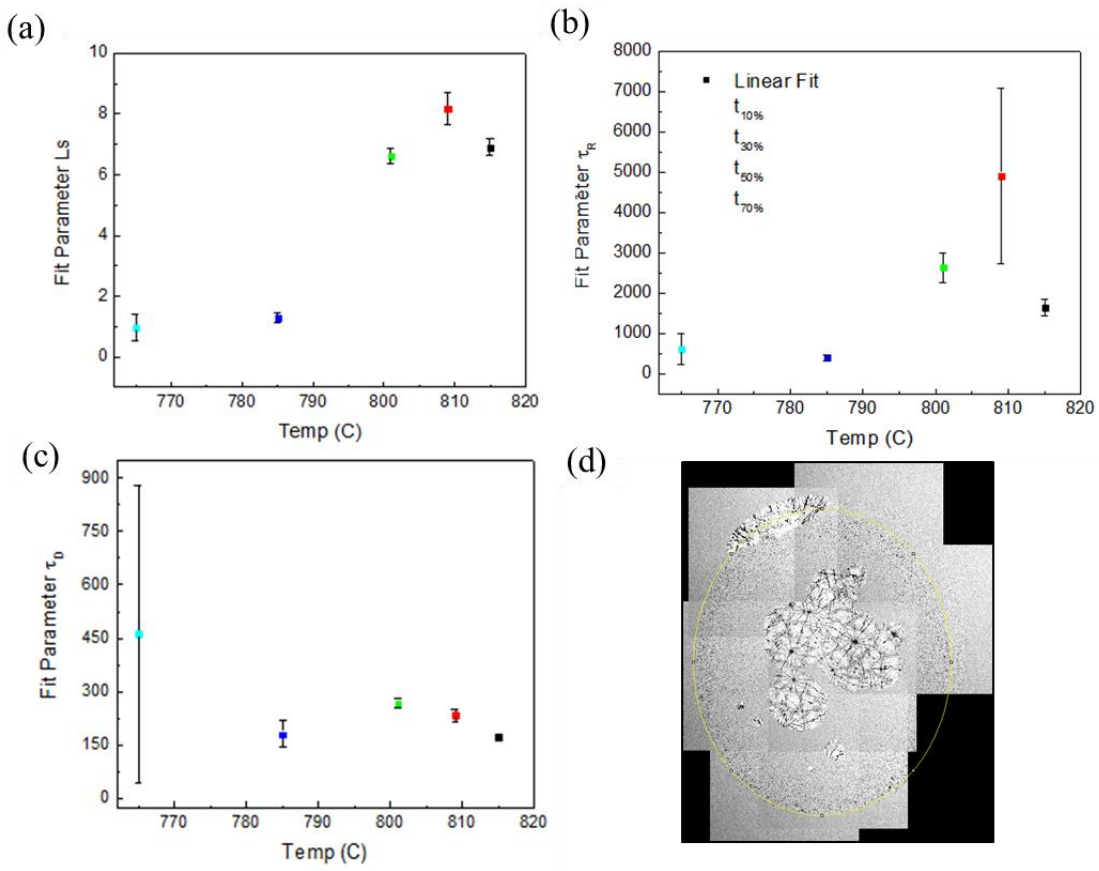

Figure 5.13. (a-c) Fit parameters for the stress limited crystallization model for different calculated film temperatures at the nucleation site for that crystallite. Error bars indicate a 95% confidence interval from the fit. Colors correspond to outlines in the inset of Figure 5.12 (d) Stitched bright-field images of the laser spot. The yellow ring is the approximate radius of the laser spot and was used to find the center from which crystallite nucleation site radius were measured for temperature approximation.

5.6 Summary and Outlook

In this chapter, an *in situ* laser annealing method was developed for TEM analysis of the crystallization of amorphous YIG films on SiO_2. This method is novel in its ability to approximate an isothermal condition during crystallization by allowing for high rates of heating. It also is novel in its ability to study the same film at multiple temperatures for temperature dependent crystallization studies. We have modeled this experimental setup using a finite-difference MATLAB script which can report the approximated temperature at various radii of the laser pulse at any given time. The exact experimental temperatures were measured using contraction of the diffraction pattern compared to room temperature. A model was developed to equate the change in diffraction pattern spacing to film temperature.

The initial transformation of the film to the nanocrystalline $YFeO_3$ phase was recorded at a high frame rate for four temperatures. The evolution of the nanocrystalline phase was correlated to the evolution of the (110) peak. An Avrami analysis was used to better understand the crystallization behavior of the different temperatures. There was negative correlation between the temperature and the Avrami coefficient indicating that the crystallization dynamics may be qualitatively different at higher temperatures, limited by diffusion or dominated by nucleation events. The apparent activation was determined for the crystallization of the nanocrystalline phase in this film. This activation energy encompasses the activation energy of the nucleation as well as the growth for the nanocrystals. Further studies are needed in order to better understand the trends in the

Avrami coefficient with temperature and the separate the effects of nucleation and growth behavior on the final phases present in the film.

The formation of YIG crystallites was observed using the same *in situ* laser annealing technique as the diffraction work, but in real-space bright-field imaging. A range of temperatures was captured in the field of view due to the Gaussian temperature profile across the TEM grid window. The large single-crystal YIG crystallites grew with similar behavior at all temperatures. The growth was fit to a strain limited crystallization model. This model fit the growth behavior well for all crystallites indicating that strain plays a dominating role in the final film structure. Because of difference in substrate in these experiments and the desired crystallization substrate (Si wafer) the crystallization behavior after the crystallites enter the strain limited regime may be different than observed here. More traditional crystallization experiments, such as time-resolved XRD or DSC, on YIG films on Si wafers would be illuminating to the role of strain in these systems.

6. Chapter 6 – Optimization of Single-Shot UEM

This chapter will focus on a specific mode of operation for a UEM known as single-shot. It is aptly named because all experimental data is collected in a single burst of electrons. This allows irreversibly processes to be probed at timescales only limited by the duration of the electron packet. The greatest challenge with this technique is generating enough electrons in a single burst to form an image with enough contrast to make useful observations. The instrumentation needed to confront this challenge at the University of Minnesota's time-resolved TEM lab was addressed in this work.

6.1 Introduction

Single-shot TEM, also referred to as dynamic TEM (DTEM), was one of the earliest forms of ultrafast TEM experiments to be performed. Bostanjoglo et al. pioneered the field and published the first paper on this technique in 1980.[111] It opened up a pathway to probe the nonreversible dynamics of materials that happened too quickly and at too small of length scales to be studied with traditional methods. Laser induced phase changes was one of the first phenomenas to be studied with this technique and remains a popular area of interest today.[112-120] This is just one example of a dynamic process that necessitates this experimental technique. Others include grain growth, ablation, melting, and structural

changes, etc. With better resolution both temporally and spatially, as well as creative experimental design, more experimental areas of interest will continue to arise.

Currently there are only three groups actively publishing results from a single-shot TEM setup. These are at California Insitute of Technology (CIT),[121] Lawrence Livermore National Laboratory (LLNL),[122] and Institut de Physique et Chimie des Matériaux de Strasbourg (IPCMS).[123] Other institutions are currently planning on or currently beginning to start up labs that have single-shot UEM capability.

Due to the nonreversible nature of the dynamics investigated with the single-shot technique, each experiment can only yield data from one time point in a standard setup. A modification can be made to the projection system of the TEM to allow for up to 16 time points to be investigated with a single pump pulse. This is a technique known as movie mode.[124] The camera is partitioned into sections which each house the signal from different time points. Using deflector coils added to the projection system, the electron beam can quickly be directed to these different sections for successive electron probe packets.

Both LLNL and IPCMS have microscopes which are outfitted with a C_0 lens.[125-126] This lens sits between the Wehnelt assembly and the first condenser lens and aids in the collection of electrons. Our microscope, as well as the microscope at CIT, does not have this lens. A systematic study has not been done to look at the effects of the C0 lens and if it is truly necessary to perform DTEM experiments.

All of the other DTEM systems have demonstrated electron counts in a single pulse large enough for imaging. The CIT images are generally lower in counts, though these numbers are rarely reported in publications. The other two institutions use a different tip geometry for producing photoelectrons. Instead of a cone like LaB_6 structure, work has been done to show that a large flat tantalum disc is able to provide the most coherent beam.[127] A systematic study of tip material has not been reported, however, tantalum does have a much higher damage threshold compared to LaB6, possibly allowing for more photoelectron generation even though it has a higher work function. This work uses a comparatively small (150 μm diameter) LaB_6 tip which is the same as those being used in stroboscopic and thermionic experiments. While likely not the ideal source for single-shot experiments, it requires no hardware changes to the microscope to switch between operational modes with this setup.

In the following experiments, the single-shot TEM setup at the University of Minnesota is optimized for the current hardware. A demonstration is given of current single-shot technologies. A discussion about possible ways in which to improve the setup will follow.

6.2 Experimental

The following experiments are demonstrations of the electron counts from a single photoelectron packet in a single-shot setup. The counts are taken at the camera and are representative of the number of electrons available for signal in a single-shot experiment.

The experimental setup is the same as that described in Chapter 2 for single-shot UEM mode, but without the use of the pumping laser.

After the probe beam has been aligned at 1 kHz, low power and focused to a small area on the camera, the pulse energy for the probe laser line needed to be maximized. By optimizing both the second and fourth harmonic doubling crystals, a conversion ratio of roughly 5% was able to be achieved. This limited pulse energies to roughly 10 μJ. For each experiment, the pulse energy was found by measuring the average power of the 1 kHz beam and dividing by 1,000. This optimized laser was now set to 1 Hz and defocused on the LaB_6 cathode. From here the experimental conditions were changed depending on the independent variable being investigated. Unless otherwise noted, each data point is representative of the average of 20 successive electron packets.

All images acquired in this chapter for counting were in low magnification mode of the TEM. No apertures were inserted except for the custom large condenser aperture described in Chapter 2. The specimen holder was left empty. A 150 um diameter custom flat LaB_6 tip (Applied Photonics) was used as the cathode. This tip is comparable to tips commonly used in thermionic and stroboscopic operating modes in the lab. The tip was not carbon coated in this study.

6.2.1 Changing Cathode Height

The distance between the Wehnelt aperture and the flat of the LaB_6 tip is adjustable. The gun region of the microscope was vented to atmosphere and the entire Wehnelt assembly needed to be removed. There is a screw mechanism that controls the position of

the Wehnelt aperture. It should be noted that the tip is in a fixed position with respect to the rest of the microscope and the Wehnelt cap is moving. The flat of the LaB_6 tip is aligned to the Wehnelt aperture by aligning them both to a focal plane in an optical microscope. The Wehnelt cap has numbered markings which represent 0.1 mm of vertical distance when turned to that position. It is by this manner the tip height is set.

6.2.2 Changing Probe Laser Fluence

The focusing lens on the side of the TEM column near the gun periscope was used to control the laser diameter at the LaB_6 flat. For experiments controlling fluence of the probe laser, the micrometer controlled focusing lens was started at a maximum position away from the TEM column, greatly over focusing the laser and ensuring we are far from the damage threshold. The micrometer was slowly moved towards a cross-over position with data being collected at various micrometer positions corresponding to different laser fluences at the cathode.

6.3 Analysis

The data for these experiments consists of images of electrons focused into a spot of various radius. Unless otherwise noted, the Orius camera was used in a 4x binning mode. The radius of the beam was not rigorously controlled during the experiments and needed to be adjusted to avoid saturation while maintaining high signal to noise level. To limit the noise when summing the counts in the image, a region of interest was defined for

each image. The electron packet image in Figure 6.1 is representative of the single-shot electron images. The intensity in each image was fit to a two dimensional Gaussian. Pixels outside of three standard deviations from the center of the Gaussian we not included in the summing of total counts in the image.

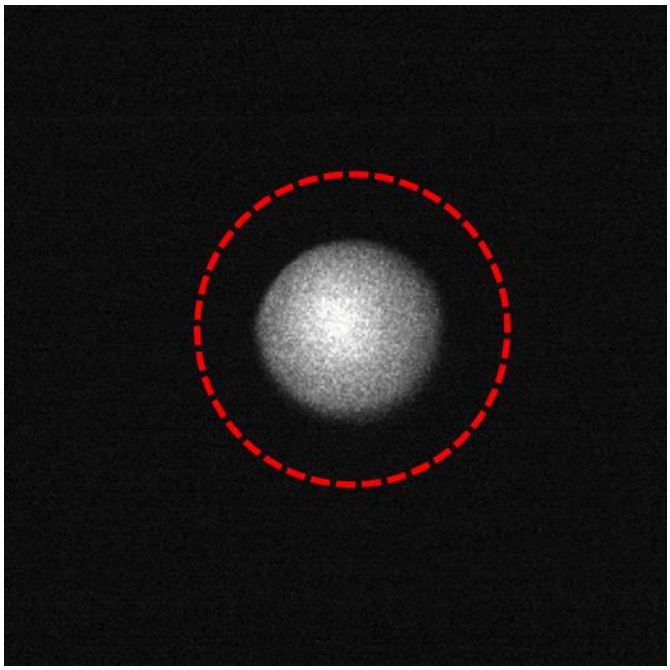

Figure 6.1. Representative electron counting image of a single photoelectron packet. Images were acquired in low magnification mode at 17x magnification. The red ring shows the masking radius corresponding to 3 standard deviations of a Gaussian fit.

Each pixel has varying levels of noise and a baseline value associated with it. When summing pixels to calculate total counts from the electron packet, the background noise and counts need to be subtracted. Immediately after 20 images of photoelectron packets are captured for a specific condition, the mechanical shutter for the probe laser is closed

and 20 more images are acquired. The two dimensional Gaussian profile mask described above is then applied to these images as well. The mean of the 20 dark images is subtracted from the mean of the electron packet images for a background subtracted mean electron count.

6.4 Results and Discussion

6.4.1 Tip Height Optimization

In an attempt to maximize single-shot electron counts, the role of the distance between the cathode and the Wehnelt aperture was investigated. This follows from modeling work reported by Kieft et al. They report an optimized distance that is dependent on other microscope features such as Wehnelt aperture diameter and is a function of the number of electrons in the electron packet.[61] The geometry of their model as well as the trends related to Wehnelt-tip distance is shown in Figure 6.2. This model was similar to our experimental setup with no C_0 aperture though the nature of the self-bias of the Wehnelt aperture is not well understood in our microscope for photoelectron mode. The model did not have an applied bias to the Wehnelt.

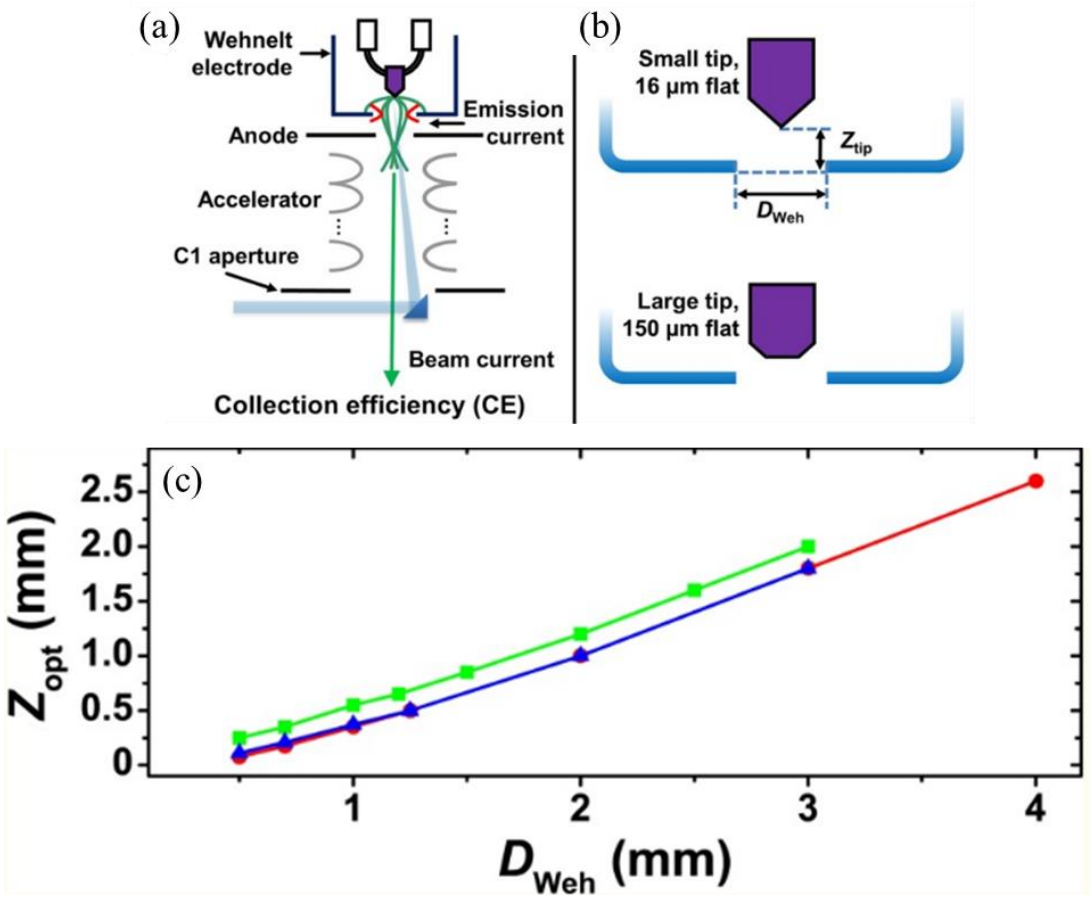

Figure 6.2. (a) Thermionic electron-gun geometry for a LaB6 source used in the model. (b) Configuration of the tip height (Z_{tip}) and Wehnelt aperture. (c) Optimized tip height for a given Wehnelt diameter. The blue triangles represent the optimum for single-shot mode. Adapted from Kieft et al.[61]

Figure 6.3 shows an experimental data from our instrument. Each data point represents the average of three 20 shot experiments per tip height. Between each 20 shot experiment, the tip was manually realigned for optimized counts. Precise alignment is crucial to obtaining high counts per shot and introduced high variability in the

measurements. The error bars represent one standard deviation for the 60 shots measured at each tip height.

Using a t-test to compare the mean of the 350 µm height and the closest other mean at 450 µm, the t-test score was calculated to be 8.55. Using 60 shots to calculate the mean yields 59 as a degree of freedom for the measurement. This t-test results in an alpha value much less than 0.001 meaning that there is less than a 0.1% chance that the mean value for the 350 µm height is actually lower than the 450 µm height. Based on this analysis we report that the optimal tip height for the described experimental setup is between 300 µm and 400 µm. We were unable to fill in this plot with more data points due to equipment considerations involved with venting the gun region.

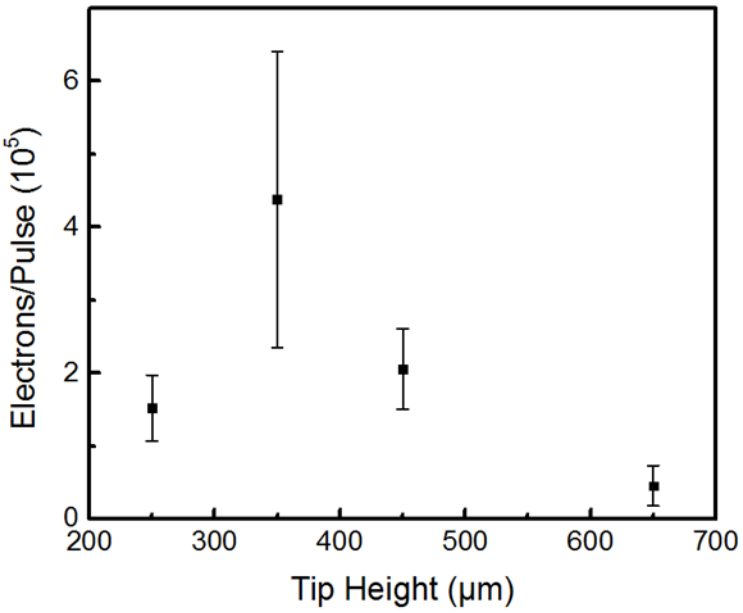

Figure 6.3. Average electrons counted at the camera per single-shot pulse as a function of tip height for a 2 mm diameter Wehnelt aperture. Error bars indicate one standard deviation from 60 averaged shots.

The reported optimal height does not agree with the modeled value for optimization. The Kieft model shown in Figure 6.2(c) has an optimized position close to 1 mm, much farther than our own findings. This discrepancy could be explained by the existence of a self-bias applied to the Wehnelt aperture in our experiments due to the high electron current. This may make the effective Wehnelt aperture smaller helping to explain the experimental optimal position.

6.4.2 Laser Fluence

In order to probe the effect of laser fluence on photoemission in single-shot mode of our microscope, the tip was set to the optimally found height (350 μm) and the pulse energy was maximized. The focusing lens was manipulated to decrease the laser spot size and increase the fluence at the cathode. Figure 6.4 shows the results of this experiment. Each data point is the mean of 20 shots and the error bars represent one standard deviation. The electron beam and focusing lens were realigned between each fluence change. The experiment was continued until the high tension could no longer be maintained in the gun region due to damage of the LaB_6 crystal. Spikes in vacuum pressure at the gun were observed when the damage threshold was reached.

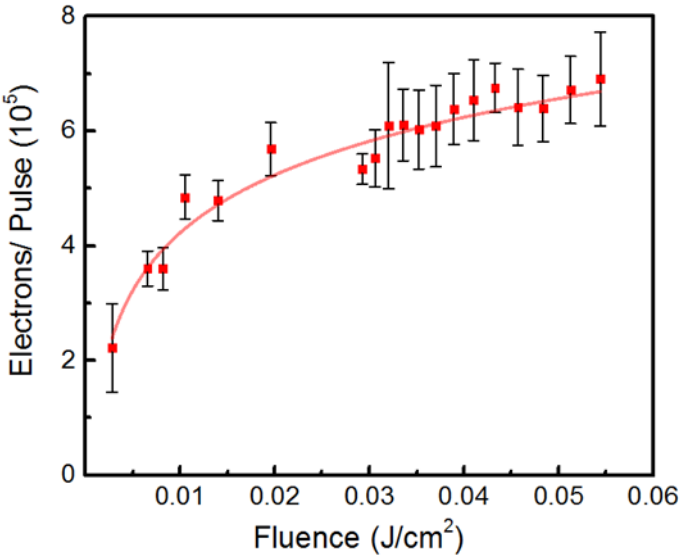

Figure 6.4. Average electrons counted at the camera per single-shot pulse as a function of laser fluence for a 2 mm diameter Wehnelt aperture Error bars indicate one standard deviation from 60 averaged shots. Line is a fit to the space-charge limited photoelectron emission model.

The photoemission of electrons from the cathode in the TEM is a process which depends upon the fluence of the laser pulses. More photons incident on the tip will generate more electrons, though this is not a linear relationship. Previous work done by Plemmons et al. has shown that the number of electrons emitted matches the proposed physical model of an image charge limiting the number of electrons generated.[42] The piecewise physical model is below.[128]

$$n_{e^-} = \begin{cases} b_0 + b_1 F + \frac{b_2}{2} F^2 & F < F_0 \\ b_0 + b_1 F_0 + \frac{b_2}{2} {F_0}^2 + n_{e^-}^{lim} \log\left(\frac{F}{F_0}\right) & F > F_0 \end{cases}$$

This model represents a quadratic relationship between the number of electrons (n_{e-}) and laser fluence (F) before the saturation limit with b_0 and b_1 representing coefficients for the one and two photon emission process respectively. After the saturation limit, F_0, the relationship between the number of electrons and fluence follows a logarithmic relationship due to photoemission suppression as a result of the image-charge effect. In Figure 6.4 this latter relationship is fit to the experimental data with high agreement. This indicates we are operating in the image-charge limiting region with diminishing returns with increasing fluence. It should be noted that the last two data points have a full width half max (FWHM) calculated to be smaller than the diameter of the tip.

The fit suggests that the limit of electrons before entering the space-charge limiting regime is at 1.45×10^5 electrons with a standard error of 1.1×10^4. This value is highly dependent on the diameter of the tip as well as factors such as contamination, cathode surface topology and any possibly non-optimized positioning of the tip with respect to the Wehnelt aperture.

6.4.3 Photoelectron Yield

Important factors to consider when discussing the ability to generate photoelectrons for UEM experiments are the quantum efficiency and loss in the column and gun region (column loss). Here, we see our best achieved photon to electron conversion at the lowest fluence because we are already in the space-charge limiting regime. However, using this value, and using values for quantum efficiency and column loss reported in literature, we are able to demonstrate our system behaving with expected column losses which are

comparable to systems with a C_0 lens. Our total efficiency can be defined as the product of the quantum efficiency and the column efficiency. For LaB_6 single-crystal (001) the quantum efficiency is dependent on the surface condition of the tip as well as the wavelength used for photoemission.[129] At photon wavelengths of 266 nm, single-crystal LaB_6 cathodes have been measured to have a quantum efficiency between $6x10^{-6}$ and $1x10^{-5}$ depending on the temperature of the cathode is a study by Torgasin et al..[130] While this study did not optimize for quantum efficiency, they reported similar pulse energies to those used here. Recently, a single-shot experimental setup with a C_0 lens reported a calculated 2% column efficiency, meaning that only 2% of the electrons generated at the cathode made it to the camera.[123] Using this value for column efficiency with the best reported quantum yield, we would expect a total yield of approximately $2x10^{-7}$. Our own best measured total yield is approximately $5x10^{-8}$. Our calculated column losses are 99.5%.

There are a number of factors which could account for not being able to reach a higher yield value. One obvious factor is the fact that our best measurement in this study is still above the space-charge limit. It would be more appropriate to optimize our quantum yield at a lower fluence. Another factor is that we may not be operating with a clean tip. In the cited quantum efficiency, the vacuum pressure at the cathode was better than 10^{-8} Torr while our gun operates at approximately 10^{-6} Torr. Additionally, the reported LaB_6 quantum efficiencies are for higher cathode temperature than those used here, which have been shown to have a better quantum efficiency. Finally, our system may have more

column losses than those reported by Picher et al. A more rigorous study of our tips quantum efficiency would be needed to calculate total column losses.

6.4.4 Imaging and Diffraction capabilities

Images and diffraction patterns obtained with the optimized experimental single-shot settings and Gatan OneView camera are shown in Figure 6.5. Figure 6.5(a) is representative of current real space imaging capabilities in single-shot mode. The edge of a 15 nm oriented gold foil is imaged to demonstrate the imaging capabilities for diffraction contrast as well as mass-thickness contrast. Approximately $4x10^5$ electrons were used to form this image which was binned by eight in post processing to increase the signal. Figures 6.5(b,c) show what 10 and 100 electron packets used to create the image look like to give a sense of the needed electron counts to achieve imaging capabilities for desired levels of contrast. Figure 6.5(d) is a diffraction pattern of the 15 nm oriented gold along the (001) zone axis. Here we clearly observe the first order and second order Bragg spots. In Figure 6.5(e), 10 shots are summed, again demonstrating what an order of magnitude increase in electron counts would appear like. The spots are brighter but no more information is gained from the low order Bragg spots. This indicates we have an appropriate level of electrons to perform single-shot diffraction experiments with our current setup given an appropriately diffracting specimen. In Figure 6.5(f) the edge of a copper grid bar is imaged with a single packet of photoelectrons. Because the grid bar is not electron transparent, this represents the highest contrast possible for imaging. Experiments performed at the CIT single-shot TEM setup have utilized this “shadow

imaging" technique to probe material dynamics of particles[121] and nanowires[131] which are not electron transparent.

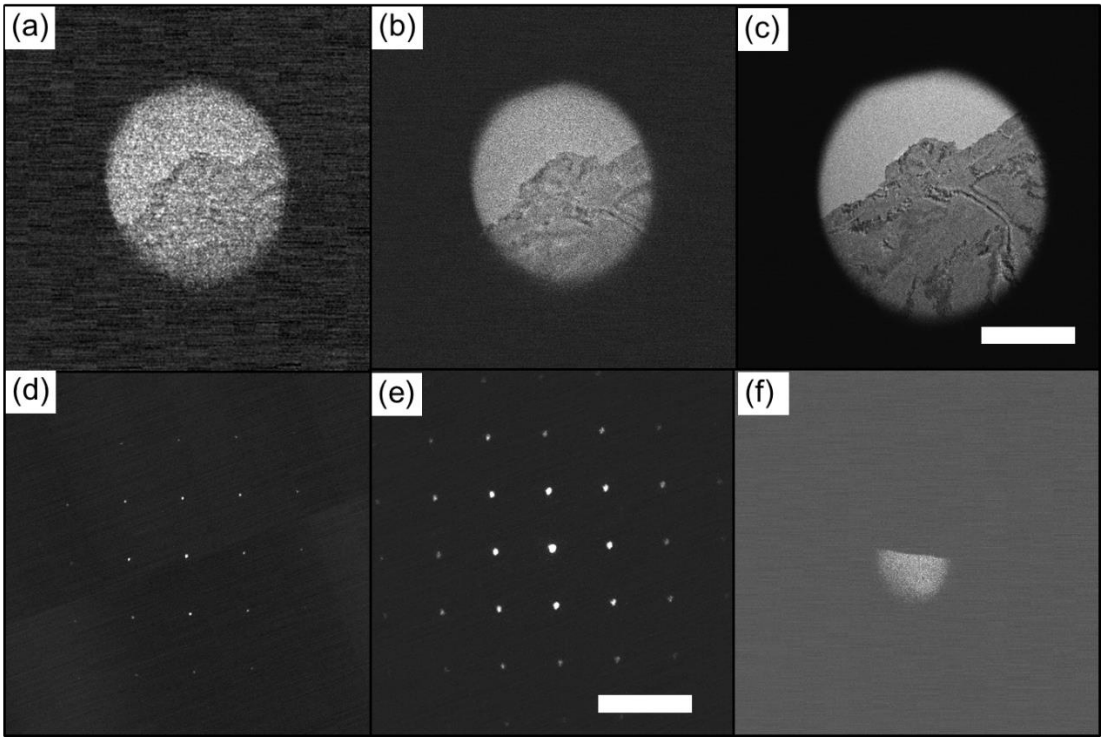

Figure 6.5. (a-c) real space images of a 15nm oriented gold foil with varying number of electron packets; (a) 1 shot; (b) 10 shots; (c) 100 shots. The scale bar is 5 μm. (d,e) SADP of 15nm oriented gold foil; (d) 1 shot; (e) 10 shots. (f) Image of copper grid bar edge.

6.4.5 Tip Geometry and Damage

Because the tip height has been optimized and the fluence study suggests that we are at the limit for LaB_6 for photoelectron emission, the only other means to improve counts in single-shot mode is with equipment changes. By increasing the tip diameter, we could expect to see electron emission which scales with emission area. Tips currently used by

other single-shot groups are more than an order of magnitude larger in area than those used here.[123, 132] By extrapolating the number of electrons per shot based upon the increased tip area, if we were to use a tip of 0.8 mm diameter like those in other studies, we could expect to see approximately a 30 fold increase in electron counts. This would put our imaging quality between Figure 6.5(b) and (c) above. Increasing the tip diameter would also require a higher pulse energy in order to achieve the appropriate fluence values for high photoemission. As mentioned earlier, in this study, we needed to focus the tip down to an area smaller than the tip before we reached the damage threshold. As such, if we were to increase the laser diameter, we will need to increase our laser fluence by a similar amount. A dedicated laser would need to be acquired to meet this higher pulse energy demand.

6.6 Conclusion and Outlook

Though this study has shown the plausibility of performing single-shot experiments using equipment in our lab, it has largely outlined areas where there are still short-comings and ways in which single-shot photoelectron counts can be improved. There does appear to be an optimal location for the cathode with relation to the Wehnelt aperture but the precise location is still in question. Further studies will be needed in order to find this distance to a higher degree of certainty. We have demonstrated the space-charge effect in a LaB_6 cathode and the role that fluence plays in photoemission of electrons. This will be the limiting factor in our TEM with current equipment. By increasing the number of electrons in a pulse, we can hope to perform experiments with specimen dynamic having lower contrast. A larger tip will help to improve these counts.

Another outstanding question with our single-shot setup is the instrument response. Other single-shot setups have lasers for photoelectron extraction with pulse durations of greater than 10 ns.[121, 123, 132] Our laser is sub-nanosecond in pulse duration. This means we could possibly achieve higher temporal resolution. It also means our peak pulse power is higher for a given fluence than those used by other groups. This could be limiting because the damage threshold for a cathode will be reached more quickly for the same number for photons incident for photoexcitation. Systematic studies will be needed for determining instrument response.

A final issue to address is the cathode material used in a single-shot TEM setup. Here, we are using a LaB_6 tip because it is compatible with thermionic mode as well as stroboscopic UEM. Other single-shot groups have used tantalum cathodes. It is unclear if space-charge effects and damage thresholds would be similar in these materials or if a tantalum cathode would be a more suitable material for single-shot UEM experiments.

Bibliography

1. R. P. Feynman, There's plenty of room at the bottom: An invitation to enter a new field of physics. In *Handbook of Nanoscience, Engineering, and Technology, Third Edition*, CRC Press: 2012; 26-35.

2. K. C. Chun; H. Zhao; J. D. Harms; T.-H. Kim; J.-P. Wang; C. H. Kim. A scaling roadmap and performance evaluation of in-plane and perpendicular MTJ based STT-MRAMs for high-density cache memory. *IEEE Journal of Solid-State Circuits* **2013,** *48*, 598-610.

3. A. Esfandiar; B. Radha; F. Wang; Q. Yang; S. Hu; S. Garaj; R. Nair; A. Geim; K. Gopinadhan. Size effect in ion transport through angstrom-scale slits. *Science* **2017,** *358*, 511-513.

4. X. Yin; Y. Shi; Y. Wei; Y. Joo; P. Gopalan; I. Szlufarska; X. Wang. Unit cell level thickness control of single-crystalline zinc oxide nanosheets enabled by electrical double-layer confinement. *Langmuir* **2017,** *33*, 7708-7714.

5. J. W. Nielsen; E. F. Dearborn. The growth of single crystals of magnetic garnets. *Journal of Physics and Chemistry of Solids* **1958,** *5*, 202-207.

6. W. Wettling; B. Andlauer; P. Koidl; J. Schneider; W. Tolksdorf. Optical absorption and Faraday rotation in yttrium iron garnet. *Physica Status Solidi B: Basic Research* **1973,** *59*, 63-70.

7. A. A. Serga; A. V. Chumak; B. Hillebrands. YIG magnonics. *Journal of Physics D: Applied Physics* **2010,** *43*, 264002.

8. I. C. Hunter; J. D. Rhodes. Electronically tunable microwave bandpass filters. *IEEE Transactions on Microwave Theory and Techniques* **1982,** *30*, 1354-1360.

9. T. Boudiar; B. Payet-Gervy; M. F. Blanc-Mignon; J. J. Rousseau; M. Le Berre; H. Joisten. Magneto-optical properties of yttrium iron garnet (YIG) thin films elaborated by radio frequency sputtering. *Journal of Magnetism and Magnetic Materials* **2004,** *284*, 77-85.

10. S. Geller; M. A. Gilleo. The crystal structure and ferrimagnetism of yttrium-iron garnet, $Y_3Fe_2(FeO_4)_3$. *Journal of Physics and Chemistry of Solids* **1957,** *3*, 30-36.

11. P. Larsen; R. Metselaar. Defects and the electronic properties of $Y_3Fe_5O_{12}$. *Journal of Solid State Chemistry* **1975,** *12*, 253-258.

12. R. Lecraw; D. Wood; J. Dillon Jr; J. Remeika. The optical transparency of yttrium iron garnet in the near infrared. *Applied Physics Letters* **1965,** *7*, 27-28.

13. Ü. Özgür; Y. Alivov; H. Morkoç. Microwave ferrites, part 1: fundamental properties. *Journal of Materials Science: Materials in Electronics* **2009,** *20*, 789-834.

14. P. Hansen; K. Witter; W. Tolksdorf. Magnetic and magneto-optic properties of lead-and bismuth-substituted yttrium iron garnet films. *Physical Review B* **1983,** *27*, 6608.

15. M. Gomi; K. Satoh; M. Abe. Giant Faraday rotation of Ce-substituted YIG films epitaxially grown by RF sputtering. *Japanese Journal of Applied Physics* **1988,** *27*, L1536.

16. M.-C. Tien; T. Mizumoto; P. Pintus; H. Kromer; J. E. Bowers. Silicon ring isolators with bonded nonreciprocal magneto-optic garnets. *Optics express* **2011,** *19*, 11740-11745.

17. P. Dulal; A. D. Block; T. E. Gage; H. A. Haldren; S.-Y. Sung; D. C. Hutchings; B. J. Stadler. Optimized magneto-optical isolator designs inspired by seedlayer-free terbium iron garnets with opposite chirality. *ACS Photonics* **2016,** *3*, 1818-1825.

18. D. C. Hutchings; C. Zhang; B. M. Holmes; P. Dulal; A. D. Block; B. J. Stadler In *Faraday polarisation mode conversion in semiconductor waveguides incorporating periodic garnet claddings*, Integrated Optics: Devices, Materials, and Technologies XX, International Society for Optics and Photonics: 2016; 97500V.

19. C. Zhang; P. Dulal; B. J. Stadler; D. C. Hutchings. Monolithically-integrated TE-mode 1D silicon-on-insulator isolators using seedlayer-free garnet. *Scientific reports* **2017,** *7*, 5820.

20. L. Bi; J. Hu; P. Jiang; D. H. Kim; G. F. Dionne; L. C. Kimerling; C. Ross. On-chip optical isolation in monolithically integrated non-reciprocal optical resonators. *Nature Photonics* **2011,** *5*, 758.

21. M. Onbasli; A. Kehlberger; D. Kim; G. Jakob; M. Kläui; A. Chumak; B. Hillebrands; C. Ross. Pulsed laser deposition of epitaxial yttrium iron garnet films with low Gilbert damping and bulk-like magnetization. *APL Materials* **2014,** *2*, 106102.

22. H. Chang; P. Li; W. Zhang; T. Liu; A. Hoffmann; L. Deng; M. Wu. Nanometer-thick yttrium iron garnet films with extremely low damping. *IEEE Magnetics Letters* **2014,** *5*, 1-4.

23. Y. Sun; Y.-Y. Song; H. Chang; M. Kabatek; M. Jantz; W. Schneider; M. Wu; H. Schultheiss; A. Hoffmann. Growth and ferromagnetic resonance properties of nanometer-thick yttrium iron garnet films. *Applied Physics Letters* **2012,** *101*, 152405.

24. C. Hahn; G. De Loubens; O. Klein; M. Viret; V. V. Naletov; J. B. Youssef. Comparative measurements of inverse spin Hall effects and magnetoresistance in YIG/Pt and YIG/Ta. *Physical Review B* **2013,** *87*, 174417.

25. M. Jungfleisch; A. Chumak; A. Kehlberger; V. Lauer; D. Kim; M. Onbasli; C. Ross; M. Kläui; B. Hillebrands. Thickness and power dependence of the spin-pumping effect in $Y_3Fe_5O_{12}$/Pt heterostructures measured by the inverse spin Hall effect. *Physical Review B* **2015,** *91*, 134407.

26. D. Qu; S. Huang; J. Hu; R. Wu; C. Chien. Intrinsic spin Seebeck effect in Au/YIG. *Physical Review Letters* **2013,** *110*, 067206.

27. A. B. Cahaya; O. A. Tretiakov; G. E. Bauer. Spin Seebeck power generators. *Applied Physics Letters* **2014,** *104*, 042402.

28. F.-J. Chang; J. G. Lin; S.-Y. Huang. Robust spin current generated by the Spin Seebeck Effect. *Physical Review Materials* **2017,** *1*, 031401.

29. P. Pintus; D. Huang; C. Zhang; Y. Shoji; T. Mizumoto; J. E. Bowers. Microring-based optical isolator and circulator with integrated electromagnet for silicon photonics. *Journal of Lightwave Technology* **2017,** *35*, 1429-1437.

30. T. Mizumoto; R. Baets; J. E. Bowers. Optical nonreciprocal devices for silicon photonics using wafer-bonded magneto-optical garnet materials. *MRS Bulletin* **2018,** *43*, 419-424.

31. Y. Zhang; C. Wang; X. Liang; B. Peng; H. Lu; P. Zhou; L. Zhang; J. Xie; L. Deng; M. Zahradnik. Enhanced magneto-optical effect in $Y_{1.5}Ce_{1.5}Fe_5O_{12}$ thin films deposited on silicon by pulsed laser deposition. *Journal of Alloys and Compounds* **2017,** *703*, 591-599.

32. M. Balinskiy; S. Ojha; H. Chiang; M. Ranjbar; C. A. Ross; A. Khitun. Spin wave excitation in sub-micrometer thick $Y_3Fe_5O_{12}$ films fabricated by pulsed laser deposition on garnet and silicon substrates: A comparative study. *Journal of Applied Physics* **2017,** *122*, 123904.

33. T. E. Gage; P. Dulal; P. A. Solheid; D. J. Flannigan; B. J. Stadler. Si-integrated ultrathin films of phase-pure $Y_3F_e5O_{12}$ (YIG) via novel two-step rapid thermal anneal. *Materials Research Letters* **2017,** *5*, 379-385.

34. A. D. Block; P. Dulal; B. J. H. Stadler; N. C. A. Seaton. Growth Parameters of Fully Crystallized YIG, Bi:YIG, and Ce:YIG Films With High Faraday Rotations. *IEEE Photonics Journal* **2014,** *6*, 1-8.

35. D. Uhlmann. Glass formation. *Journal of Non-Crystalline Solids* **1977,** *25*, 42-85.

36. M. Avrami. Kinetics of phase change. I General theory. *The Journal of Chemical Physics* **1939,** *7*, 1103-1112.

37. M. Avrami. Kinetics of phase change. II transformation-time relations for random distribution of nuclei. *The Journal of Chemical Physics* **1940,** *8*, 212-224.

38. N. Pienack; W. Bensch. *In-situ* monitoring of the formation of crystalline solids. *Angewandte Chemie International Edition* **2011,** *50*, 2014-2034.

39. S. W. Chee; A. Datta; U. Anand; D. Loh; U. Mirsaidov. Capturing dynamics in liquids with high-speed CMOS cameras-opportunities and challenges. *Microscopy and Microanalysis* **2017,** *23*, 860-861.

40. G. Martinez; T. Pennycook; T. Naginey; L. Jones; H. Yang; J. Yates; R. Nicholls; M. Huth; M. Simson; H. Soltau. Towards a direct visualization of charge transfer in monolayer hexagonal boron nitride using a fast pixelated detector in the scanning transmission electron microscope. *Microscopy and Microanalysis* **2017,** *23*, 436-437.

41. V. A. Lobastov; R. Srinivasan; A. H. Zewail. Four-dimensional ultrafast electron microscopy. *Proceedings of the National Academy of Sciences* **2005,** *102*, 7069-7073.

42. D. A. Plemmons; D. J. Flannigan. Ultrafast electron microscopy: Instrument response from the single-electron to high bunch-charge regimes. *Chemical Physics Letters* **2017,** *683*, 186-192.

43. A. Arbouet; G. M. Caruso; F. Houdellier, Ultrafast Transmission Electron Microscopy: Historical Development, Instrumentation, and Applications. In *Advances in Imaging and Electron Physics*, Elsevier: 2018; Vol. 207, 1-72.

44. M. R. Armstrong; K. Boyden; N. D. Browning; G. H. Campbell; J. D. Colvin; W. J. Dehope; A. M. Frank; D. J. Gibson; F. Hartemann; J. S. Kim. Practical considerations for high spatial and temporal resolution dynamic transmission electron microscopy. *Ultramicroscopy* **2007,** *107*, 356-367.

45. P. J. Kelly; R. D. Arnell. Magnetron sputtering: a review of recent developments and applications. *Vacuum* **2000,** *56*, 159-172.

46. J. A. Thornton. Magnetron sputtering: basic physics and application to cylindrical magnetrons. *Journal of Vacuum Science and Technology* **1978,** *15*, 171-177.

47. M. Ohring, *Materials science of thin films*. Elsevier: 2001.

48. S. Berg; T. Nyberg. Fundamental understanding and modeling of reactive sputtering processes. *Thin Solid Films* **2005,** *476*, 215-230.

49. P. Lippens; U. Muehlfeld. Indium tin oxide (ITO): Sputter deposition processes. *Handbook of Visual Display Technology* **2014**, 1-16.

50. Y. Shao; M. Yan; D. J. Sellmyer. Effects of rapid thermal annealing on nanostructure, texture and magnetic properties of granular FePt: Ag films for perpendicular recording. *Journal of Applied Physics* **2003,** *93*, 8152-8154.

51. K. K. Kim; S. Niki; J. Y. Oh; J. O. Song; T. Y. Seong; S. J. Park; S. Fujita; S. W. Kim. High electron concentration and mobility in Al-doped n-ZnO epilayer achieved via dopant activation using rapid-thermal annealing. *Journal of Applied Physics* **2005,** *97*,

52. J. Fitch; C. Bjorkman; G. Lucovsky; F. Pollak; X. Yin. Intrinsic stress and stress gradients at the SiO_2/Si interface in structures prepared by thermal oxidation of Si and subjected to rapid thermal annealing. *Journal of Vacuum Science & Technology B: Microelectronics Processing and Phenomena* **1989,** *7*, 775-781.

53. C.-R. Cho; S. Cho; S. Vadim; R. Jung; I. Yoo. Current-induced metal–insulator transition in VOx thin film prepared by rapid-thermal-annealing. *Thin Solid Films* **2006,** *495*, 375-379.

54. B. D. Cullity; S. R. Stock, *Elements of X-ray Diffraction*. Pearson Education: 2014.

55. D. Shindo; T. Oikawa, Energy dispersive x-ray spectroscopy. In *Analytical Electron Microscopy for Materials Science*, Springer: 2002; 81-102.

56. S. Foner. Vibrating sample magnetometer. *Review of Scientific Instruments* **1956,** *27*, 548-548.

57. P. Flanders. An alternating-gradient magnetometer. *Journal of Applied Physics* **1988,** *63*, 3940-3945.

58. D. B. Williams; C. B. Carter. The Transmission Electron Microscope. *Transmission Electron Microscopy* **2009**, 3-22.

59. T. Kawasaki; T. Yoshida; T. Matsuda; N. Osakabe; A. Tonomura; I. Matsui; K. Kitazawa. Fine crystal lattice fringes observed using a transmission electron microscope with 1 MeV coherent electron waves. *Applied Physics Letters* **2000,** *76*, 1342-1344.

60. G. Mcmullan; A. Faruqi; D. Clare; R. Henderson. Comparison of optimal performance at 300 keV of three direct electron detectors for use in low dose electron microscopy. *Ultramicroscopy* **2014,** *147*, 156-163.

61. E. Kieft; K. B. Schliep; P. K. Suri; D. J. Flannigan. Effects of Electron-Gun and Laser Parameters on Collection Efficiency and Packet Duration in Ultrafast Electron Microscopy. *Microscopy and Microanalysis* **2015,** *21*, 807-808.

62. Y. G. Chukalkin; V. Shtirz; B. Goshchitskii. The structure and magnetism of amorphous $Y_3Fe_5O_{12}$. *Physica Status Solidi (A)* **1989,** *112*, 161-174.

63. A. D. Block; P. Dulal; B. J. Stadler; N. C. Seaton. Growth parameters of fully crystallized YIG, Bi: YIG, and Ce: YIG films with high faraday rotations. *IEEE Photonics Journal* **2014,** *6*, 1-8.

64. Y. Zhang; J. Xie; L. Deng; L. Bi. Growth of phase pure yttrium iron garnet thin films on silicon: the effect of substrate and postdeposition annealing temperatures. *IEEE Transactions on Magnetics* **2015,** *51*, 1-4.

65. S. Shahrokhvand; A. Rozatian; M. Mozaffari; S. Hamidi; M. Tehranchi. Preparation and investigation of Ce: YIG thin films with a high magneto-optical figure of merit. *Journal of Physics D: Applied Physics* **2012,** *45*, 235001.

66. B. Bhoi; N. Venkataramani; R. Aiyar; S. Prasad. FMR and magnetic studies on polycrystalline YIG thin films deposited using pulsed laser. *IEEE Transactions on Magnetics* **2013,** *49*, 990-994.

67. Y.-M. Kang; S.-H. Wee; S.-I. Baik; S.-G. Min; Y. Seong-Cho; M. Seung-Hyun; Y.-W. Kim; Y. Sang-Im. Magnetic properties of YIG thin films prepared by the post annealing of amorphous films deposited by RF-magnetron sputtering. *Journal of Applied Physics* **2005,** *97*, 10A319-10A319-3.

68. S. Y. Sung; Q. Xiaoyuan; B. J. Stadler. Integrating yttrium iron garnet onto nongarnet substrates with faster deposition rates and high reliability. *Applied Physics Letters* **2005,** *87*,

69. S. Blank; J. Nielsen. The growth of magnetic garnets by liquid phase epitaxy. *Journal of Crystal Growth* **1972,** *17*, 302-311.

70. S. H. Vajargah; H. M. Hosseini; Z. Nemati. Preparation and characterization of yttrium iron garnet (YIG) nanocrystalline powders by auto-combustion of nitrate-citrate gel. *Journal of Alloys and Compounds* **2007,** *430*, 339-343.

71. K. Kitayama; M. Sakaguchi; Y. Takahara; H. Endo; H. Ueki. Phase equilibrium in the system Y–Fe–O at 1100° C. *Journal of Solid State Chemistry* **2004,** *177*, 1933-1938.

72. M. Ismael; E. Elhaddad; D. H. Taffa; M. Wark. Synthesis of phase pure hexagonal $YFeO_3$ perovskite as efficient visible light active photocatalyst. *Catalysts* **2017,** *7*, 326.

73. M. Wang; T. Wang; S. Song; M. Tan. Structure-controllable synthesis of multiferroic $YFeO_3$ nanopowders and their optical and magnetic properties. *Materials* **2017,** *10*, 626.

74. N. Rodziah; M. Hashim; I. Idza; I. Ismayadi; A. Hapishah; M. Khamirul. Dependence of developing magnetic hysteresis characteristics on stages of evolving microstructure in polycrystalline yttrium iron garnet. *Applied Surface science* **2012,** *258*, 2679-2685.

75. D. M. Gil; M. C. Navarro; M. C. Lagarrigue; J. Guimpel; R. E. Carbonio; M. I. Gómez. Synthesis and structural characterization of perovskite $YFeO_3$ by thermal decomposition of a cyano complex precursor, Y [Fe (CN) $_6$]· $4H_2O$. *Journal of Thermal Analysis and Calorimetry* **2010,** *103*, 889-896.

76. O. Yamaguchi; Y. Mukaida; A. Hayashida. Formation and transformation of tetragonal $Y_3Fe_5O_{12}$. *Journal of Materials Science Letters* **1990,** *9*, 1314-1315.

77. J. Liu; Q. Jin; S. Wang; P. Yu; C. Zhang; C. Luckhardt; Z. Su; R. Barua; V. G. Harris. An insight into formation mechanism of rapid chemical Co-precipitation for synthesizing yttrium iron garnet nano powders. *Materials Chemistry and Physics* **2018,** *208*, 169-176.

78. V. Popkov; O. Almjasheva; V. Gusarov. The investigation of the structure control possibility of nanocrystalline yttrium orthoferrite in its synthesis from amorphous powders. *Russian Journal of Applied Chemistry* **2014,** *87*, 1417-1421.

79. H. Shen; J. Xu; M. Jin; G. Jiang. Influence of manganese on the structure and magnetic properties of $YFeO_3$ nanocrystal. *Ceramics International* **2012,** *38*, 1473-1477.

80. L. J. Downie; R. J. Goff; W. Kockelmann; S. D. Forder; J. E. Parker; F. D. Morrison; P. Lightfoot. Structural, magnetic and electrical properties of the hexagonal ferrites $MFeO_3$ (M= Y, Yb, In). *Journal of Solid State Chemistry* **2012,** *190*, 52-60.

81. M. Derras; N. Hamdad. New approach for the spin effect on the ground state properties of the cubic and hexagonal $YFeO_3$ perovskite oxide: GGA+ U based on the DFT+ U description. *Results in Physics* **2013,** *3*, 61-69.

82. K. B. Schliep; J.-Y. Chen; M. Li; J.-P. Wang; D. J. Flannigan. Laser-initiated magnetization reversal and correlated morphological effects visualized with *in situ* Fresnel transmission electron microscopy. *Physical Review B* **2016,** *94*, 104407.

83. P. Gruszecki; A. Serebryannikov; W. Śmigaj; M. Krawczyk. Microwave excitation of spin wave beams in thin ferromagnetic films. *Scientific reports* **2015**,

84. A. Ishikawa; T. Amemiya; Y. Shoji; P. N. Hai; M. Tanaka; T. Mizumoto; S. Arai; T. Tanaka. Optical and magnetic microstructures in YIG ferrite fabricated by femtosecond laser. *Journal of Laser Micro Nanoengineering* **2015,** *10*, 48.

85. H. Kurebayashi; O. Dzyapko; V. E. Demidov; D. Fang; A. Ferguson; S. O. Demokritov. Controlled enhancement of spin-current emission by three-magnon splitting. *Nature Materials* **2011,** *10*, 660-664.

86. M. Levy; R. Osgood; H. Hegde; F. Cadieu; R. Wolfe; V. Fratello. Integrated optical isolators with sputter-deposited thin-film magnets. *Photonics Technology Letters, IEEE* **1996,** *8*, 903-905.

87. W. Lin; K. Chen; S. Zhang; C. L. Chien. Enhancement of Thermally Injected Spin Current through an Antiferromagnetic Insulator. *Physical Review Letters* **2016,** *116*, 186601.

88. M. Ristić; I. Nowik; S. Popović; I. Felner; S. Musić. Influence of synthesis procedure on the YIG formation. *Materials Letters* **2003,** *57*, 2584-2590.

89. D. Sun; K. J. Van Schooten; H. Malissa; M. Kavand; C. Zhang; C. Boehme; Z. V. Vardeny. Inverse spin hall effect from pulsed spin current in organic semiconductors with tunable spin-orbit coupling. *Nature Materials* **2015**,

90. T. Suzuki. Magnetic and magneto-optic properties of rapid thermally crystallized garnet films. *Journal of Applied Physics* **1991,** *69*, 4756-4760.

91. Y. Zhang; J. Xie; L. Deng; L. Bi. Growth of Phase Pure Yttrium Iron Garnet Thin Films on Silicon: The Effect of Substrate and Postdeposition Annealing Temperatures. *Magnetics, IEEE Transactions on* **2015,** *51*, 1-4.

92. B.-S. Lee; G. W. Burr; R. M. Shelby; S. Raoux; C. T. Rettner; S. N. Bogle; K. Darmawikarta; S. G. Bishop; J. R. Abelson. Observation of the role of subcritical nuclei in crystallization of a glassy solid. *Science* **2009,** *326*, 980-984.

93. F. Tichelaar; F. Schapink; X. Li. *In situ* TEM observations of the order-disorder transition at interfaces in Cu_3Au. *Philosophical Magazine A* **1992,** *65*, 913-929.

94. Q. Jeangros; T. W. Hansen; J. B. Wagner; C. D. Damsgaard; R. E. Dunin-Borkowski; C. Hebert; A. Hessler-Wyser. Reduction of nickel oxide particles by hydrogen studied in an environmental TEM. *Journal of Materials Science* **2013,** *48*, 2893-2907.

95. K. Kaneko; K. Inoke; K. Sato; K. Kitawaki; H. Higashida; I. Arslan; P. Midgley. TEM characterization of Ge precipitates in an $Al_{1.6}$ at% Ge alloy. *Ultramicroscopy* **2008,** *108*, 210-220.

96. M. Asoro; D. Kovar; P. Ferreira. Effect of surface carbon coating on sintering of silver nanoparticles: *in situ* TEM observations. *Chemical Communications* **2014,** *50*, 4835-4838.

97. M. A. Van Huis; N. P. Young; G. Pandraud; J. F. Creemer; D. Vanmaekelbergh; A. I. Kirkland; H. W. Zandbergen. Atomic imaging of phase transitions and morphology transformations in nanocrystals. *Advanced Materials* **2009,** *21*, 4992-4995.

98. A. M. Hofmeister. Thermal diffusivity of garnets at high temperature. *Physics and Chemistry of Minerals* **2006,** *33*, 45-62.

99. R. Kato; I. Hatta. Thermal conductivity measurement of thermally-oxidized SiO_2 films on a silicon wafer using a thermo-reflectance technique. *International Journal of Thermophysics* **2005,** *26*, 179-190.

100. S. Andersson; L. Dzhavadov. Thermal conductivity and heat capacity of amorphous SiO_2: pressure and volume dependence. *Journal of Physics: Condensed Matter* **1992,** *4*, 6209.

101. K. Modi; P. Jha; P. Raval; N. Vasoya; K. Vyas; U. Meshiya; R. Gohil; K. Jadav; N. Gohil; P. Sharma. Study on thermodynamic properties of Fe^{3+}-substituted yttrium iron garnets. *Acta Physica Polonica (A)* **2016,** *130*, 778-784.

102. J.-I. Kushibiki; M. Arakawa; R. Okabe. High-accuracy standard specimens for the line-focus-beam ultrasonic material characterization system. *IEEE Transactions on Ultrasonics, Ferroelectrics, and Frequency Control* **2002,** *49*, 827-835.

103. G. White. Thermal expansion of reference materials: copper, silica and silicon. *Journal of Physics D: Applied Physics* **1973,** *6*, 2070.

104. S. Spinner; G. Cleek. Temperature dependence of Young's modulus of vitreous germania and silica. *Journal of Applied Physics* **1960,** *31*, 1407-1410.

105. H. Chou; E. D. Case. Characterization of some mechanical properties of polycrystalline yttrium iron garnet (YIG) by non-destructive methods. *Journal of Materials Science Letters* **1988,** *7*, 1217-1220.

106. A. Prnová; A. Plško; J. Valúchová; K. Haladejová; R. Klement; D. Galusek. Crystallization kinetics of glass microspheres with yttrium aluminium garnet (YAG) composition. *Journal of Thermal Analysis and Calorimetry* **2018,** *131*, 1115-1123.

107. J. Očenášek; P. Novák; S. Agbo. Finite-thickness effect on crystallization kinetics in thin films and its adaptation in the Johnson–Mehl–Avrami–Kolmogorov model. *Journal of Applied Physics* **2014,** *115*, 043505.

108. T. Pradell; D. Crespo; N. Clavaguera; M. Clavaguera-Mora. Diffusion controlled grain growth in primary crystallization: Avrami exponents revisited. *Journal of Physics: Condensed Matter* **1998,** *10*, 3833.

109. Y. P. Fu; F. Y. Tsai. Nonisothermal Crystallization Kinetics of $Bi_xY_{3-x}Fe_5O_{12}$ ($0.25 \leq x \leq 1.00$) Prepared from Coprecipitation Process. *Journal of the American Ceramic Society* **2008,** *91*, 1214-1217.

110. C. Bocker; I. Avramov; C. Rüssel. The effect of stresses during crystallization on the crystallite size distributions. *Journal of the European Ceramic Society* **2011,** *31*, 2861-2866.

111. O. Bostanjoglo; R. Liedtke. Tracing fast phase transitions by electron micrscopy. *Physica Status Solidi (A)* **1980,** *60*, 451-455.

112. O. Bostanjoglo; G. Hoffmann. Time-Resolved TEM of Transient Effects in Pulse Annealing of Ge and Ge–Te Films. *Physica Status Solidi (A)* **1982,** *73*, 95-105.

113. O. Bostanjoglo; W. Horinek. Pulsed TEM: A new method to detect transient structures in fast phase transitions. *Optik* **1983,** *65*, 361-367.

114. O. Bostanjoglo; D. Otte. High speed transmission electron microscopy of laser quenching. *Materials Science and Engineering A* **1993,** *A173*, 407-411.

115. O. Bostanjoglo; D. Otte. High-speed electron microscopy of nanocrystallization in Al-Ni films by nanosecond laser pulses. *Physica Status Solidi (A)* **1995,** *150*, 163-169.

116. O. Bostanjoglo; P. Thomsen-Schmidt. Laser-induced multiple phase transitions in Ge-Te films traced by time-resolved TEM. *Applied Surface Science* **1989,** *43*, 136-141.

117. O. Bostanjoglo; P. Thomsen-Schmidt. Time-resolved TEM of laser-induced structural changes in GeTe films. *Applied Surface Science* **1990,** *46*, 392-397.

118. O. Bostanjoglo; M. Weingartner. Pulsed photoelectron microscope for imaging laser-induced nanosecond processes. *Review of Scientific Instruments* **1997,** *68*, 2456-2460.

119. T. Lagrange; D. S. Grummon; B. W. Reed; N. D. Browning; W. E. King; G. H. Campbell. Strongly driven crystallization processes in a metallic glass. *Applied Physics Letters* **2009,** *94*,

120. M. K. Santala; S. Raoux; G. H. Campbell. Kinetics of liquid-mediated crystallization of amorphous Ge from multi-frame dynamic transmission electron microscopy. *Applied Physics Letters* **2015,** *107*,

121. X. Fu; B. Chen; J. Tang; M. T. Hassan; A. H. Zewail. Imaging rotational dynamics of nanoparticles in liquid by 4D electron microscopy. *Science* **2017,** *355*, 494-498.

122. G. C. Egan; T. Lagrange; M. R. Zachariah. Time-resolved nanosecond imaging of nanoscale condensed phase reaction. *Journal of Physical Chemistry C* **2015,** *119*, 2792-2797.

123. M. Picher; K. Bücker; T. Lagrange; F. Banhart. Imaging and electron energy-loss spectroscopy using single nanosecond electron pulses. *Ultramicroscopy* **2018,** *188*, 41-47.

124. T. Lagrange; B. W. Reed; D. J. Masiel. Movie-mode dynamic electron microscopy. *MRS Bulletin* **2015,** *40*, 23-28.

125. K. Bücker; M. Picher; O. Crégut; T. Lagrange; B. Reed; S. Park; D. Masiel; F. Banhart. Electron beam dynamics in an ultrafast transmission electron microscope with Wehnelt electrode. *Ultramicroscopy* **2016,** *171*, 8-18.

126. T. Lagrange; G. H. Campbell; B. W. Reed; M. Taheri; J. B. Pesavento; J. S. Kim; N. D. Browning. Nanosecond time-resolved investigations using the *in situ* of dynamic transmission electron microscope (DTEM). *Ultramicroscopy* **2008,** *108*, 1441-1449.

127. S. Ji; L. Piazza; G. Cao; S. T. Park; B. W. Reed; D. J. Masiel; J. Weissenrieder. Influence of cathode geometry on electron dynamics in an ultrafast electron microscope. *Structural Dynamics* **2017,** *4*, 054303.

128. P. Pasmans; D. Van Vugt; J. Van Lieshout; G. Brussaard; O. Luiten. Extreme regimes of femtosecond photoemission from a copper cathode in a DC electron gun. *Physical Review Accelerators and Beams* **2016,** *19*, 103403.

129. M. Asakawa; N. Sakamoto; Y. Shimizu; S. Nakai; K. Imasaki; C. Yamanaka. Experimental studies of photocathode materials for FELs. *Nuclear Instruments and*

Methods in Physics Research Section A: Accelerators, Spectrometers, Detectors and Associated Equipment **1993,** *331*, 302-306.

130. K. Torgasin; K. Morita; H. Zen; K. Masuda; T. Katsurayama; T. Murata; S. Suphakul; H. Yamashita; T. Nogi; T. Kii. Thermally assisted photoemission effect on CeB_6 and LaB_6 for application as photocathodes. *Physical Review Accelerators and Beams* **2017,** *20*, 073401.

131. B. Chen; X. Fu; J. Tang; M. Lysevych; H. H. Tan; C. Jagadish; A. H. Zewail. Dynamics and control of gold-encapped gallium arsenide nanowires imaged by 4D electron microscopy. *Proceedings of the National Academy of Sciences* **2017**, 201708761.

132. T. Lagrange; M. R. Armstrong; K. Boyden; C. G. Brown; G. H. Campbell; J. D. Colvin; W. J. Dehope; A. M. Frank; D. J. Gibson; F. V. Hartemann; J. S. Kim; W. E. King; B. J. Pyke; B. W. Reed; M. D. Shirk; R. M. Shuttlesworth; B. C. Stuart; B. R. Torralva; N. D. Browning. Single-shot dynamic transmission electron microscopy. *Applied Physics Letters* **2006,** *89*,